Analysis and Control of Vortex Shedding from a Blunt Trailing Edge

by

Bradley Joseph Gibeau

A thesis submitted in partial fulfillment of the requirements for the degree of

Master of Science

Department of Mechanical Engineering
University of Alberta

Abstract

The work within this thesis is concerned with an unsteady flow phenomenon known as vortex shedding. It is ubiquitous throughout engineering applications and leads to unwanted noise, vibration, and pressure drop in the afflicted systems. Vortex shedding is highly complex, and even with over a century of research on the subject, there are many aspects of the phenomenon that we do not yet understand. This thesis advances the current understanding of how vortex shedding affects the wake of a two-dimensional blunt trailing edge. The investigation begins with an in-depth analysis of the three-dimensional vortex structures that are present in the unsteady wake. It is shown that the blunt trailing edge geometry investigated here results in a wake that contains the same structures as that of cylindrical geometries. Specifically, the mode B secondary instability that was originally observed in the wake of a circular cylinder is found to have a dominant presence. The use of oscillating piezoelectric flaps for controlling the unsteady wake is then investigated. It is found that the actuation configuration designed here is capable of both suppressing and enhancing the vortex shedding pattern in the wake. Moreover, a symmetric shedding mode can be forced for a small range of actuation frequencies, leading to interesting wake behaviour that is not naturally present. Finally, a real-time optimization technique known as adaptive slope-seeking is used to seek an optimal control input for suppressing the wake. The closed-loop controller is capable of reaching and maintaining the optimal input and is robust to slow variations in freestream velocity within the designed operating range.

Preface

The results from Chapter 4 of this thesis have been published in the *Journal of Fluid Mechanics* as presented below.

1. Gibeau, B., Koch, C. R., and Ghaemi, S. (2018) Secondary instabilities in the wake of an elongated two-dimensional body with a blunt trailing edge. *Journal of Fluid Mechanics*, 846, pp. 578-604.

The Cambridge University Press is the copyright holder; however, permission to reproduce the work is retained under the transfer of copyright:

> *You [the author] may reproduce the article or an adapted version of it in any volume of which you are editor or author subject to normal acknowledgement.*

I personally conducted the experiments and analysis for this paper and wrote the manuscript under the supervision of the co-authors. The paper details an experimental investigation of the three-dimensional vortex structures that are present in the wake of a two-dimensional body with a blunt trailing edge. The work appears here as close to the publication form as possible while adhering to the thesis structure. For example, the introduction and experimental setup from the publication have been moved to the appropriate chapters.

The results from Chapter 5 have not yet been submitted to a journal for peer review; however, the process of assembling the results into a journal article for future publication is underway.

Dedicated to Sara Kay

Acknowledgements

First and foremost I would like to thank Prof. Sina Ghaemi and Prof. Bob Koch for allowing me to work under their guidance for the last two years. The quality of your mentoring has far exceeded expectation.

Second, I would like to express my appreciation for Bernie Faulkner and Rick Conrad for helping me handle all things mechanical and electrical, respectively, during my research. Your assistance has been invaluable.

And finally, to my friends and family, thank you for accommodating my schedule, enduring my frustration, supporting me in reaching my goals, and providing a much needed distraction when the time was right.

Contents

List of Tables

List of Figures

Chapter 1

Introduction

1.1 Motivation

Vortex shedding is an unsteady flow phenomenon that occurs in the wakes of nominally two-dimensional bodies whose trailing edges are not streamlined (i.e. bluff bodies). The result is a distinct flow pattern consisting of the alternate shedding of two rows of spanwise vortices from the trailing edge of the body. The phenomenon has been the subject of studies for over a century, beginning with the work of Strouhal (1878). As discussed by Zdravkovich (1996), Strouhal began an investigation into the tones emitted from wires exposed to fluid flow. As it turned out, he was hearing frequencies caused by the shedding of vortices from the cylindrical wires. The signature pattern left in the wake of a body experiencing the phenomenon would go on to be named the von Kármán vortex street, although von Kármán (1954) has acknowledged the contributions of Mallock (1907) and Bénard (1908) prior to his in the early 1900s (von Kármán, 1911).

Many different geometries have been used to study vortex shedding in the past, but the two-dimensional circular cylinder has been the most popular (Williamson, 1996a). This is likely due to its single characteristic length, experimental simplicity, and ubiquity within engineering. This thesis focuses on vortex shedding from a blunt trailing edge (BTE), which is another commonly encountered bluff body geometry found within engineering applications. For example, transport trucks, large ships, wind turbine blades, and tall structures all experience fluid flow past blunted features. Despite this, there is a lack of understanding of

how the wakes of BTEs compare to those of other bluff body geometries. This can be a significant issue given that the phenomenon is usually accompanied by vibration (Williamson and Govardhan, 2004), noise (Brooks et al., 1989), and pressure drop (Roshko, 1993), all of which have the potential to cause problems in the afflicted systems. A better understanding of BTE wakes could lead to improved vortex shedding suppression techniques that allow for mitigation of the negative effects. This thesis aims to expand the current knowledge relating to both understanding and controlling an unsteady, two-dimensional BTE wake flow.

1.2 Thesis Overview

Chapter 2 provides the background information necessary for understanding the work contained in the primary results chapters. This includes discussions about bluff body wake dynamics, control strategies, flow measurements, and mathematical analyses.

Chapter 3 provides the details of the experiments. The configurations of the wind tunnel, blunt body model, and measurement equipment are given, and the closed-loop control system is outlined.

Chapter 4 investigates the secondary vortices in the wake of a BTE using five separate experiments. The dimensions and spatio-temporal symmetry of the vortices are determined, and the link between the wake structures and the upstream boundary layer is scrutinized. The results are compared to the current literature and an inconsistency is addressed.

Chapter 5 examines the use of piezoelectric bending actuators for actively manipulating the wake region. The entire operating range of the actuators is characterized, and the energy of the wake flow is investigated to categorize the impact of actuation. Cases of vortex shedding amplification, suppression, and forced symmetry are studied. Adaptive slope-seeking control is then applied to optimize actuation in real time.

Chapter 6 summarizes the present thesis and states its contributions. The thesis is concluded with a discussion about future work.

Chapter 2

Background

2.1 Bluff Body Wake Dynamics

Bluff bodies with two- and three-dimensional geometries exist within engineering systems. Both experience periodic shedding of coherent vortex structures within their wakes, but the shedding occurs in different forms. The von Kármán vortex shedding pattern afflicts two-dimensional bluff bodies, while three-dimensional bluff body wakes feature different vortex structures (Johnson and Patel, 1999). Vortex shedding from nominally two-dimensional bodies is the topic of this thesis and so this section will focus on vortex shedding of the von Kármán type.

2.1.1 Primary Vortex Formation

Von Kármán vortex shedding is characterized by the alternate roll-up and subsequent shedding of spanwise vortices from the trailing edge of a two-dimensional bluff body experiencing fluid flow (von Kármán, 1954). The process is self-sustaining once it begins, as it is each alternately forming vortex that causes the formation of the next (Gerrard, 1966). The formation of a spanwise vortex from one of the separating shear layers causes a pressure gradient that forces the roll-up of the opposite shear layer. The affected shear layer is pulled across the wake centre line as it forms into a vortex itself, acting to detach the original vortex from the body. The newly forming vortex then acts on the opposing shear layer in the same manner, causing the cycle to repeat. The wake flow is steady prior to the onset of vortex shedding, and it is a Hopf bifurcation that marks the initiation of the unsteady wake

process (Jackson, 1987).

The lower threshold at which vortex shedding begins can be characterized using the Reynolds number:

$$Re(L) = \frac{\rho U_\infty L}{\mu}, \tag{2.1}$$

where ρ is fluid density, U_∞ is the freestream velocity, L is a characteristic length, and μ is the dynamic viscosity of the fluid. The thickness of the trailing edge is typically used as the characteristic length in the present context, although modified length scales are sometimes used (Naghib-Lahouti et al., 2014). It is difficult to define the exact point at which the vortex shedding begins because surface roughness, freestream flow quality, etc., all affect transition (Williamson, 1996a). Despite this, the unsteady wake process has been observed as low as $Re(d) = 40$ in the wake of a circular cylinder with diameter d (Roshko, 1954) and $Re(h) = 154$ in the wake of a two-dimensional body with a blunt trailing edge (BTE) of height h (Petrusma and Gai, 1996). Vortex shedding in the wake of a BTE is shown in Figure 2.1, where the well-known von Kármán vortex street pattern is clearly visible in all cases (Naghib-Lahouti et al., 2012).

2.1.2 Shedding Frequency

The unsteady vortex formation process occurs at a relatively constant frequency as long as freestream flow velocity is also constant. This frequency is often nondimensionalized using the Strouhal number:

$$St(L) = \frac{f_s L}{U_\infty} \tag{2.2}$$

where f_s is the frequency of vortex shedding. The St curve as a function of Re is well-defined in the case of circular cylinders, and $St(d)$ has been shown to increase rapidly for $Re(d) < 300$ before asymptotically approaching a constant of $St(d) \approx 0.2$ (Roshko, 1954). Similar asymptotic behaviour occurs in the wake of a BTE. However, trailing edge geometry (Petrusma and Gai, 1996), experimental conditions (Williamson, 1988b), and three-dimensionality in the wake (Williamson, 1996a) have been shown to impact the exact nature of the curve.

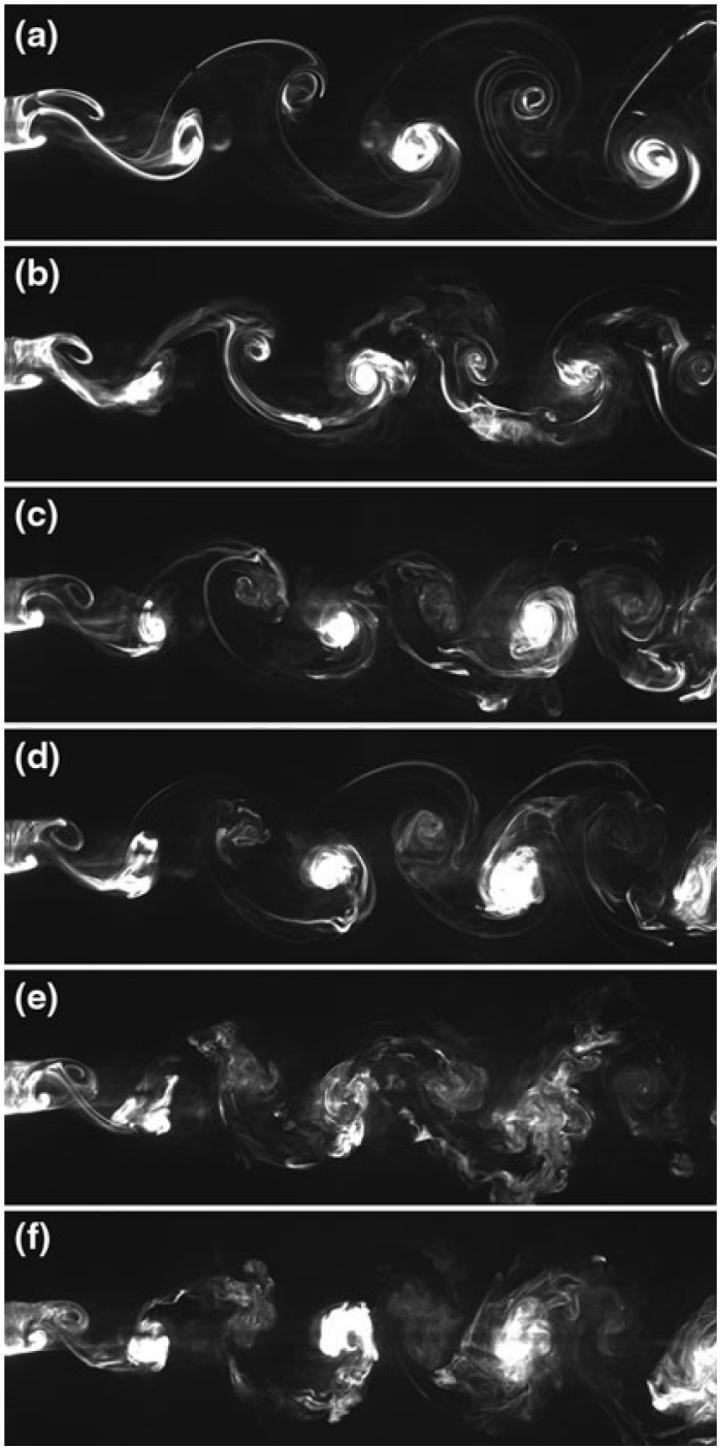

Figure 2.1: Laser-induced fluorescence images of vortex shedding in the wake of a BTE for $Re(h)$ of (a) 550, (b) 850, (c) 1150, (d) 1320, (e) 1705, and (f) 2150. Taken with permission from Naghib-Lahouti et al. (2012).

2.1.3 Formation Length and Base Pressure

Although the wake process is unsteady, time-averaged velocity information can be used to determine the 'formation length' of the primary vortex shedding process. The formation length is characterized by the boundaries of the mean recirculation region in the wake. It also corresponds to the distance downstream from the trailing edge at which point the velocity fluctuations in the wake reach a maximum, i.e. the wake unsteadiness decays downstream from this point. In general, a longer formation length is associated with a lower vortex shedding frequency and an increase in pressure at the base of the trailing edge (Williamson, 1996a).

The pressure at the trailing edge base has obvious implications for drag and is often nondimensionalized using the base pressure coefficient:

$$C_{P,B} = \frac{2\Delta P}{\rho U_\infty^2} \tag{2.3}$$

where ΔP is the difference in static pressure between the point of evaluation and the freestream flow. The base pressure coefficient measured in the wake of a circular cylinder over a large range of Re is given in Figure 2.2. The plot indicates that $C_{P,B}$ decreases rather linearly while vortex shedding is laminar. Once the wake becomes three-dimensional, there is no clear trend and base pressure varies significantly as Re increases. The unpredictable nature of the curve highlights the complexity of the vortex shedding process.

2.1.4 Secondary Instabilities

Cylinder Wakes

Even at low Re, the wake of a cylinder becomes populated with counter-rotating streamwise vortex pairs. As opposed to the primary shedding of large spanwise vortices, the much smaller streamwise vortex pairs represent the secondary wake instability and vary depending on body geometry and Re. In an early observation, Gerrard (1978) described them as "fingers of dye" during flow visualization experiments, although he did not associate them with a secondary instability at the time. Nearly a decade later, Wei and Smith (1986) detected streamwise vortices in the wake of a circular cylinder and concluded that they

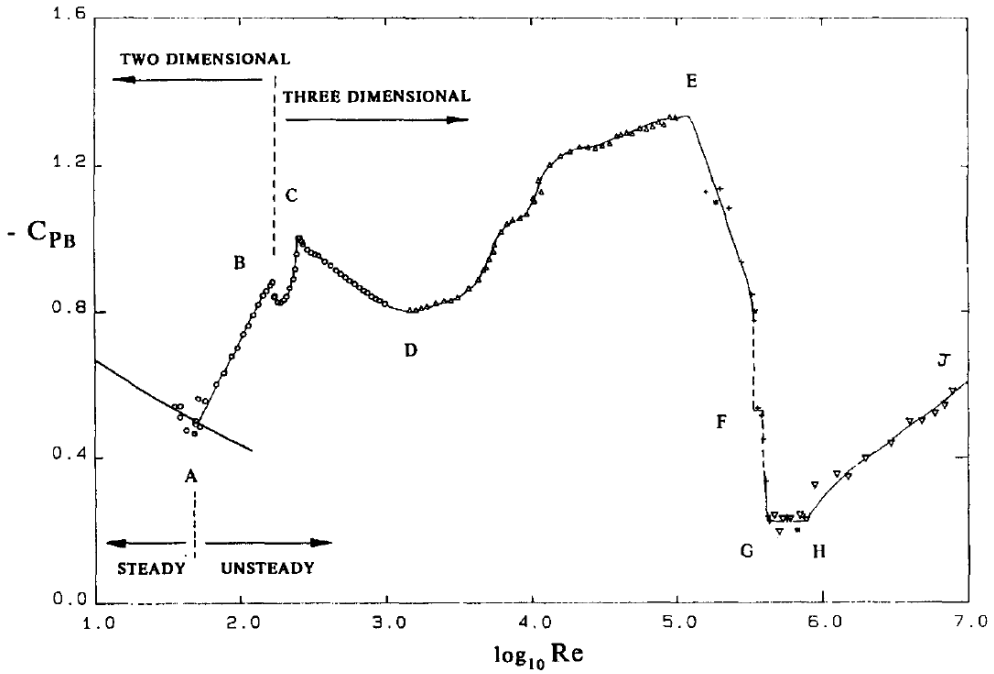

Figure 2.2: Variation of base pressure coefficient ($C_{P,B}$) in the wake of a circular cylinder as a function of Re. Taken with permission from Williamson (1996a).

were a direct result of the Tollmien-Schlichting transition waves in the separated shear layer observed by Bloor (1964). Shortly after, Williamson (1988a) showed the existence of two stages of three-dimensional transition in the unforced wake of a circular cylinder consisting of two unique instability modes: mode A and mode B. Contrary to the work of Wei and Smith (1986), Williamson (1988a) concluded that the secondary vortices cannot be a result of the Tollmien-Schlichting transition waves because the vortices appear prior to their amplification.

The secondary instabilities in the unforced wake of a circular cylinder continued to be actively investigated during the 1990s (Bays-Muchmore and Ahmed, 1993; Mansy et al., 1994; Wu et al., 1994; Lin et al., 1995a; Zhang et al., 1995; Brede et al., 1996; Wu et al., 1996; Williamson, 1996b). The generally agreed upon results are described next. Mode A is the first to appear and features vortex loops which form streamwise vortex pairs in an out-of-phase arrangement. The spacing between adjacent vortex pairs, which will be

referred to as the secondary instability wavelength, is approximately 3-5d, and a distinct characteristic of mode A is the fact that the vortex pairs change their sense of rotation every half shedding cycle of the primary instability. Mode B replaces mode A as Re is increased and consists of a much finer in-phase spatial arrangement of streamwise vortex pairs which have a secondary instability wavelength of approximately $1d$. The mode B vortex pairs weave between the primary spanwise vortices, effectively maintaining their rotational orientation for many shedding cycles. Mode B dominates the unforced cylinder wake for all appreciable Re. The instantaneous structures of modes A and B can be viewed in Figure 2.3.

A third instability mode, mode S, has been predicted by stability analysis and has the potential to occur in the unforced wake of square cylinders in addition to modes A and B (Robichaux et al., 1999). Mode S contains in-phase vortex pairs with a secondary instability wavelength of $2.8h$. These vortex pairs differ from those of modes A and B because their direction of rotation changes every shedding cycle of the primary instability. Robichaux et al. (1999) concluded that mode S is not the most unstable of the square cylinder modes and so modes A and B may need to be suppressed in order to show its existence. They also concluded that mode S is a subharmonic mode (hence its name), but this was shown to be incorrect, as it is actually quasi-periodic in nature (Blackburn and Lopez, 2003). For this reason it is more appropriately referred to as mode QP (Blackburn et al., 2005). Finally, a fourth secondary instability mode has the potential to exist when the trailing edge geometry breaks the wake symmetry. This mode is referred to as mode C and may exist in cases such as flow past square cylinders with an angle of incidence (Sheard et al., 2009) or circular cylinders with trailing edge disturbances (Yildirim et al., 2013).

There is strong evidence that mode A is the result of an elliptical instability within the primary spanwise vortices (Thompson et al., 2001); however, the origin of the mode B instability is not clear from past literature. As previously mentioned, Wei and Smith (1986) attribute the vortices to Tollmien-Schlichting transition waves. Wu et al. (1994) emphasize that the stretching of initial vorticity tubes within the separated shear layers plays a major

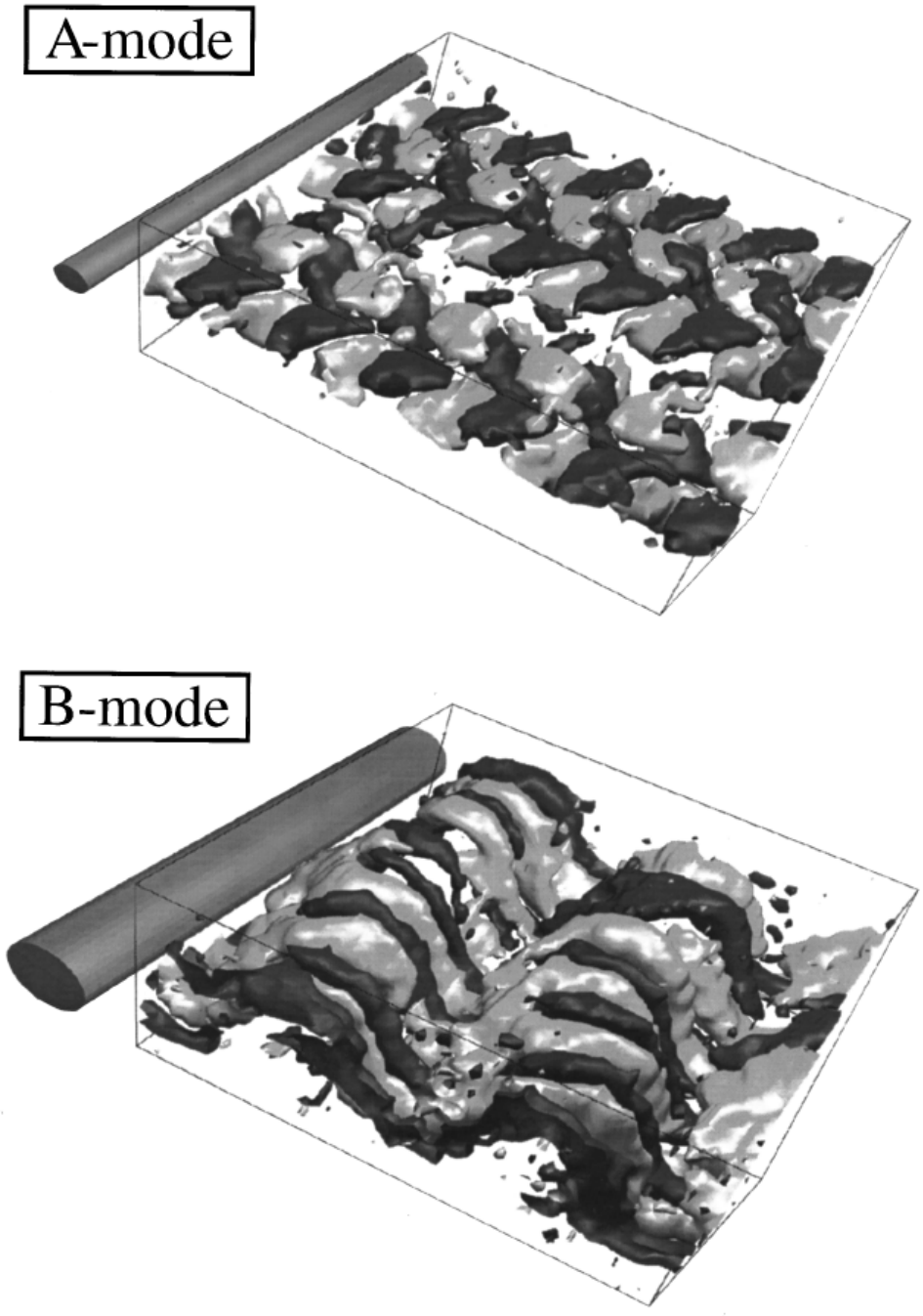

Figure 2.3: The measured spatio-temporal structures of modes A and B in the wake of a circular cylinder. The grey and black isosurfaces represent positive and negative streamwise vorticity, respectively. Taken with permission from Brede et al. (1996).

role in the development of the streamwise vortices. These initial vortex tubes may take the form of Kelvin-Helmholtz vortices that are embedded within the separated shear layers which form the primary spanwise vortices (Lin et al., 1995a). Brede et al. (1996) have shown the existence of mode B as close as $0.2d$ downstream from the trailing edge and suggest that it is the result of a shear layer instability that arises due to fluid interacting with the cylinder. Williamson (1996b) suggests that mode B is due to an instability within the braid region between interacting shear layers, and the in-phase arrangement of mode B is due to the close proximity of braid shear layers. The recently formed streamwise vortices force the same spanwise location upon the newly forming vortex pairs. This "imprinting" process has more recently been demonstrated in the near-wake of a square cylinder (Luo et al., 2007), although it does not account for the inception of the first streamwise vortices. Overall, the instability that forms mode B is different than the one that forms mode A.

Blunt Trailing Edge Wakes

The geometry considered in this thesis, the BTE, has been studied in the past using a flat plate with an elliptical leading edge and a BTE. This geometry will be referred to as an elongated blunt body from here forward. The secondary instabilities in the wake of the elongated blunt body have not been given much attention in the past. An early investigation by Ryan et al. (2005) utilized direct numerical simulations and Floquet stability analysis to probe the wakes of elongated blunt bodies with varying aspect ratios, where aspect ratio AR is defined as the ratio between chord length c and trailing edge height h. For $AR =$ 2.5, 7.5, 12.5, and 17.5 and $Re(h)$ up to 700, a key result is that AR affects which modes will appear in the wake. The circular cylinder mode A has the potential to be the most unstable for $AR < 7.5$; however, $AR > 7.5$ are susceptible to a new dominant mode. This new mode is similar to mode B of a circular cylinder in that it features streamwise vortex pairs which maintain their directions of rotation during primary shedding cycles, but it has a predicted secondary instability wavelength of $2.2h$ and also has differences in the near-wake vorticity field. For these reasons, the authors referred to it as mode B$'$. For

large AR, a third instability mode was predicted to become more unstable than Mode A. This mode was referred to as mode S$'$ due to its similarities with the square cylinder mode S (QP). It has a secondary instability wavelength of 0.7-1.0h and the streamwise vortex pairs change their direction of rotation after each full shedding cycle. Mode S$'$ seems to have more in common with the cylinder mode B than the BTE mode B$'$ because of their similar secondary instability wavelengths and near-wake vorticity fields. Mode S$'$ is the least unstable mode for $12.5 < AR < 17.5$ but more unstable than mode A for $AR > 17.5$. The prediction that the instability modes vary with AR suggests that the upstream boundary layer, which would be more developed for large AR, plays a role in the formation of the secondary instabilities. Additionally, the differences in the near-wake vorticity fields may be a result of the more developed upstream boundary layer that accompanies large AR.

It has been shown by Mansy et al. (1994) and Wu et al. (1996) that the secondary instability wavelength matches the spanwise distance between adjacent low-speed zones of streamwise velocity in the wake region. These undulating velocity patterns have been used to provide evidence for the existence of the mode B$'$ instability in the wake of an elongated blunt body with $AR = 12.5$ and $250 \leq Re(h) \leq 5 \times 10^4$ by Naghib-Lahouti et al. (2012, 2014). Both investigations found secondary instability wavelengths varying from 2.0 to 2.5h. Naghib-Lahouti et al. (2012) also observed that the vortex pairs maintained their sense of rotation based on visual inspection of laser induced fluorescence (LIF) images. They concluded that mode B$'$ was present for the geometry in question, and that the secondary instability has limited dependence on the state of the upstream boundary layer. To the author's knowledge, this is the only experimental evidence of mode B$'$ within past literature, and there does not appear to be any investigation into the wake organization of elongated blunt bodies with large AR. Moreover, the role that the upstream boundary layer plays in regulating the secondary instability has not been thoroughly scrutinized in the past.

2.2 Wake Control

Control of vortex shedding is a popular topic because it has the potential to lead to improved bluff body aerodynamics. Choi et al. (2008) characterized bluff body flow strategies into three primary groups as shown in Figure 2.4. In order of increasing complexity these are passive, active open-loop, and active closed-loop control strategies. Passive control refers to actuation without power input, for example the use of geometric modifications. Active open-loop strategies utilize powered actuation, and active closed-loop control strategies utilize real-time measurements along with powered actuators so that actuation can be tailored towards a desired control outcome. Control theory based on linear systems provides a plethora of tools for analyzing and implementing closed-loop control methods (Chen, 1999); however, modelling a fluid-dynamical system and designing a controller for flow control purposes is not straightforward. The equations commonly used to model fluid motion – the Navier-Stokes equations – are highly nonlinear, coupled partial differential equations, making linear systems theory difficult to apply to flow control problems. This has led to experimental researchers preferring the use of control methods that do not require phenomenological modelling. For example, the use of system identification, machine learning, and adaptive methods is ubiquitous in flow control literature (Brunton and Noack, 2015).

2.2.1 Actuators

The successful implementation of active flow control strategies, even in a laboratory environment, is far from trivial, and one reason for this is the difficulty in selecting appropriate actuators (Cattafesta III and Sheplak, 2011). The complex nature of fluid flows makes predicting the effects of actuation difficult. Moreover, actuators must often be implemented in a manner that is minimally invasive with respect to to the overall geometry of the system so that desirable flow characteristics can be preserved. The importance of realistic actuators for flow control is emphasized in the present work, and experimental investigations are the focus of the following discussion.

During early investigations into vortex shedding control, the wakes of cylinders were

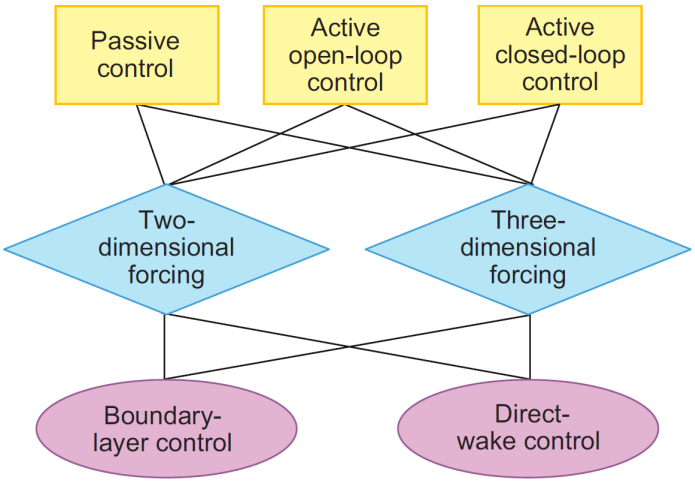

Figure 2.4: Bluff body flow control classifications. Taken with permission from Choi et al. (2008).

actuated by means of transverse oscillations (Berger, 1967; Tao et al., 1996; Warui and Fujisawa, 1996), loudspeakers (Ffowcs Williams and Zhao, 1989; Roussopoulos, 1993; Huang, 1996), and cylinder rotation (Fujisawa and Nakabayashi, 2002). While these studies provide great insight into the mechanisms behind controlling unsteady wakes, it is impractical to rely on moving the entire body itself or generating acoustic noise to control flow. The use of steady injection/suction (Lin et al., 1995b; Shi and Feng, 2015), synthetic jets (Williams et al., 1992; Lin et al., 1995b; Fujisawa et al., 2004; Pastoor et al., 2008; Feng and Wang, 2010; Qu et al., 2017), plasma actuators (Artana et al., 2003; Jukes and Choi, 2009; Kozlov and Thomas, 2011; Benard and Moreau, 2013; Nati et al., 2013; Bhattacharya and Gregory, 2015; Naghib-Lahouti et al., 2015), and control cylinders (Korkischko and Meneghini, 2012; Schulmeister et al., 2017) has become popular more recently for use with various bluff body geometries. Aside from the latter, these types of actuators can be implemented into the surface of a body to manipulate the flow while retaining the overall geometry, making them more suitable for practical applications. The length of the above list is indicative of the large variety of actuators that have been utilized during experiments; however, ideal actuators for flow control still elude researchers (Cattafesta III and Sheplak, 2011).

The use of piezoelectric materials to create actuators for flow control purposes is a

promising area of active research (Cattafesta III et al., 2001; Mathew et al., 2006; bin Mansoor et al., 2017). Piezoelectric materials expand or contract when a voltage is applied and can be used to manipulate flow boundaries using various signals. This type of actuator shows potential for many different flow control scenarios. For example, they have been used to actuate the exit of a square jet (Wiltse and Glezer, 1993, 1998), generate vortices in a boundary layer (Jacobson and Reynolds, 1998; Jeon and Blackwelder, 2000; Kim et al., 2013; Bai et al., 2014), attenuate cavity oscillations (Cattafesta III et al., 2008), and manipulate separation on an airfoil (Amir and Kontis, 2008; Bilgen et al., 2010). More closely related to the present investigation, they have also been used to suppress and enhance vortex shedding from both elastically and rigidly mounted square cylinders (Zhang et al., 2004, 2005). The actuator was mounted under a plastic plate on the top surface of the cylinder and acted to perturb the surface upwards during actuation. The authors were able to enhance and reduce the forces acting on the square cylinder by tuning a proportional-integral-derivative (PID) controller. While Zhang et al. (2004, 2005) were able to reduce the negative side effects associated with vortex shedding, their investigation lacked a detailed analysis of the mechanism responsible for vortex shedding suppression. Overall, it seems that the use of piezoelectric actuators for wake control has not been given much attention in the past.

2.2.2 Impact of Actuation

There are generally three potential outcomes when actuation is successfully applied to an unsteady, two-dimensional wake. These are amplification, suppression, and re-organization of the classic von Kármán pattern. Amplification and suppression simply refer to when the typical vortex shedding process is strengthened or weakened, respectively. Wake re-organization occurs when the structure of the von Kármán wake pattern is altered in some way. All three of these cases will be detailed next.

Amplification of the unsteadiness in the wake often occurs through resonant forcing leading to the occurrence of a 'lock-on' scenario. The classical case of lock-on is the resonant vibration of a flexibly-mounted cylinder when vortices shed from the trailing edge during

cross-flow (Williamson and Govardhan, 2004). The classical case is due to self-excitation, but forcing transverse oscillations can also lead to amplification of the vortex shedding pattern (Tao et al., 1996; Warui and Fujisawa, 1996). Vortex shedding amplification has been achieved recently using two of the more promising types of flow control actuators: plasma actuators (Jukes and Choi, 2009; Benard and Moreau, 2013) and synthetic jets (Pastoor et al., 2008). The results of these studies indicate that amplified vortex shedding is generally accompanied by increases in turbulence intensities in the wake, pressure drag, and force fluctuations on the body. As well, Benard and Moreau (2013) reported vortices that shed closer to the body, resulting in a more organized shedding pattern and a shorter recirculation region.

Suppression of the unsteady wake is arguably the most sought control outcome for the many potential benefits. A large majority of the previously discussed investigations were able to achieve vortex shedding suppression to some degree, resulting in attenuation of the unwanted pressure variations in the wake. Interestingly, vortex shedding suppression does not always occur through the same mechanisms. The slot synthetic jets used by Pastoor et al. (2008) attenuated vortex shedding in the wake by forcing the symmetric (simultaneous) roll-up of shear layers at the trailing edge of the body, leading to the postponement of shedding to further downstream and an increase in base pressure by 40%. Similar actuators used by Fujisawa et al. (2004) generated small spanwise vortices in one shear layer which weakened the interaction between the separating shear layers, leading to disruption of the wake pattern and complete attenuation of lift fluctuations on the body. Although the actuators used were similar, different mechanisms (forced symmetry versus shear layer disruption) were responsible for vortex shedding suppression, thus highlighting the importance of studying these mechanisms. Other reported active suppression mechanisms include blocking the interaction of the shear layers (Nati et al., 2013) and disrupting their spanwise coherence (Naghib-Lahouti et al., 2015).

An interesting potential result of actuation is the re-organization of the vortex structures in the wake. This occurs in the wakes of cylinders when the cylinder is vibrated in a

specific manner, and the results include various symmetric and asymmetric vortex patterns (Ongoren and Rockwell, 1988; Williamson and Govardhan, 2004; Xu et al., 2006). The reorganization of the wake to a symmetric mode is interesting from an engineering perspective because it results in the removal of the mean and fluctuating lift forces on the body that result from vortex shedding, which normally occur due to the cyclic wake asymmetry. Moreover, it has been shown that forcing the symmetric mode can lead to an increase in base pressure as previously discussed (Pastoor et al., 2008). The symmetric shedding mode has mostly been observed in the wake of an oscillating cylinder, but has also been forced using sound (Detemple-Laake and Eckelmann, 1989), freestream flow oscillations (Barbi et al., 1986; Konstantinidis and Balabani, 2007), and the aforementioned synthetic jets (Pastoor et al., 2008; Feng and Wang, 2010).

2.2.3 Adaptive Slope-Seeking

The utilization of adaptive slope-seeking allows for a system to automatically seek optimal control inputs in real time if a measurement of the plant to be controlled is available (Ariyur and Krstić, 2003). The method has been applied in numerous flow control experiments, often in the context of extremum-seeking (i.e. seeking a slope of zero). Successful experimental implementations include controlling backwards-facing step flows (Beaudoin et al., 2006a,b), airfoil separation (Becker et al., 2007; Benard et al., 2010; Chabert et al., 2014, 2016), cavity oscillations (Kim et al., 2009), jet mixing (Wu et al., 2016), and unsteady wakes (Pastoor et al., 2008; Brackston et al., 2016). A properly designed slope-seeking controller is able to guide the output of a system to a specified location on a steady-state input-output map by seeking a reference slope. A slope of zero is sought when the control goal is to drive the output to an extremum on the steady-state map. A small non-zero slope is used as the reference when the map features a plateau.

A vital component to the slope-seeking method is the use of a dither signal. The dither signal takes the form of a zero-mean waveform (usually a sinusoid) and is added to the system input to perturb the system in a regular manner. As long as the system is operating

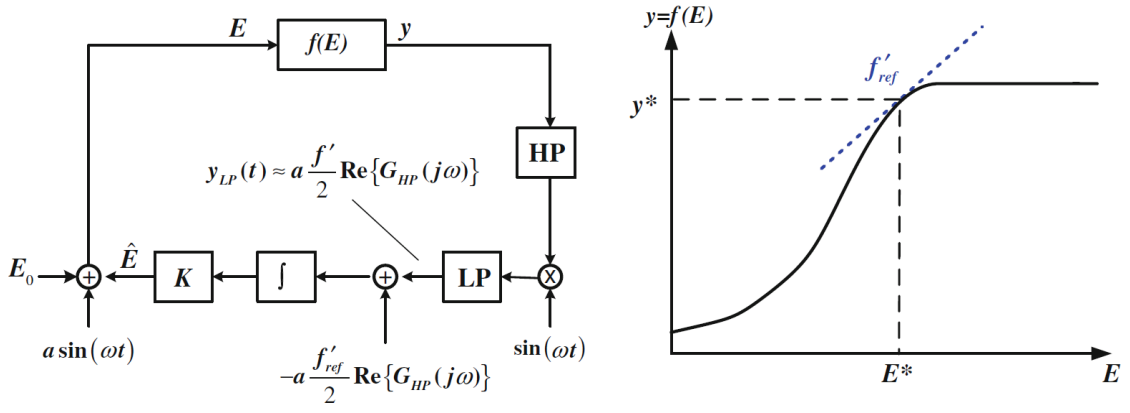

Figure 2.5: The basic slope-seeking feedback loop structure and the corresponding steady-state map. Taken with permission from Benard et al. (2010).

at a position on the steady-state map with a non-zero slope, this oscillating component to the input will cause the output to oscillate in a similar manner. When the system reaches an extremum, the oscillations in the output are minimized due to the shape of the steady-state map. The slope of the steady-state map is therefore monitored by measuring the degree to which the output oscillates with respect to the dither signal. The frequency and amplitude of the dither signal must be selected appropriately to ensure that the output of the plant oscillates along with the dither signal, i.e. the dither must be slow enough to allow for the plant dynamics to reach steady state during each dither cycle and the amplitude must be large enough to elicit a response from the system. Note that adaptive slope-seeking does not stabilize unstable plant dynamics. Instead, it acts to guide the output of the system to an optimal point and therefore is used when the plant is already stable.

The typical slope-seeking feedback loop is presented in Figure 2.5. The input to the system E consists of the initial input, the control modification, and the sinusoidal dither signal $a\sin(\omega t)$. The output of the system y is high-pass filtered, leaving only the fluctuations caused by the dither. This signal is then multiplied by the unit dither and then low-pass filtered to obtain a measure of the current slope on the steady-state map. This measure is compared to a modified target slope (modified to account for the phase shift from the high-pass filter) and the difference is fed into an integrator which acts to drive the difference

to zero by modifying the system input. Slope seeking requires selection or tuning of the dither frequency and amplitude, the filter parameters, the integrator gain, and the target slope. A detailed treatment of the mathematics behind the adaptive slope-seeking method is given by Ariyur and Krstić (2003).

2.3 Particle Image Velocimetry

Particle image velocimetry (PIV) is a popular non-invasive flow measurement technique used in experimental fluid dynamics. The fluid flow is seeded with tracer particles small enough to faithfully follow to the flow field (typically with tracing errors of less than 1%), and a laser is used to illuminate the particles within a plane (two-component and stereoscopic PIV) or volume (tomographic PIV). The motion of groups of particles is determined using calibrated camera images separated by a known time, allowing for the calculation of a velocity vector for each particle group in time. This process is applied in a grid-like fashion across images, resulting in a orthogonal grid of velocity vectors. A sample vector field obtained using the PIV technique is shown in Figure 2.6. An overview of the PIV technique is given in this section, and an in-depth treatment of PIV is given by Raffel et al. (2007).

2.3.1 Working Principle

The simplest form of PIV (two-component) occurs within a plane illuminated by a laser sheet with a typical thickness on the order of 1 mm. A camera set normal to the laser sheet is used to image the tracer particles within the fluid. The resulting images are broken into small interrogation windows, which are compared between images to measure the fluid displacement ($\Delta \boldsymbol{x}$) over a known time interval (Δt). This allows for the calculation of velocity:

$$\boldsymbol{U} = \frac{\Delta \boldsymbol{x}}{\Delta t} \tag{2.4}$$

where $\boldsymbol{U} = (U, V)$ represents the velocity of the fluid projected onto the plane and $\Delta \boldsymbol{x} = (x, y)$ is the fluid displacement within the plane. This operation is applied across the images, resulting in a vector field. A schematic of the technique is given in Figure 2.7.

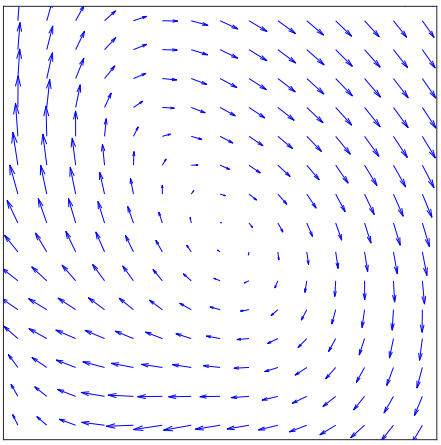

Figure 2.6: Sample vector field of a vortex obtained using the PIV technique.

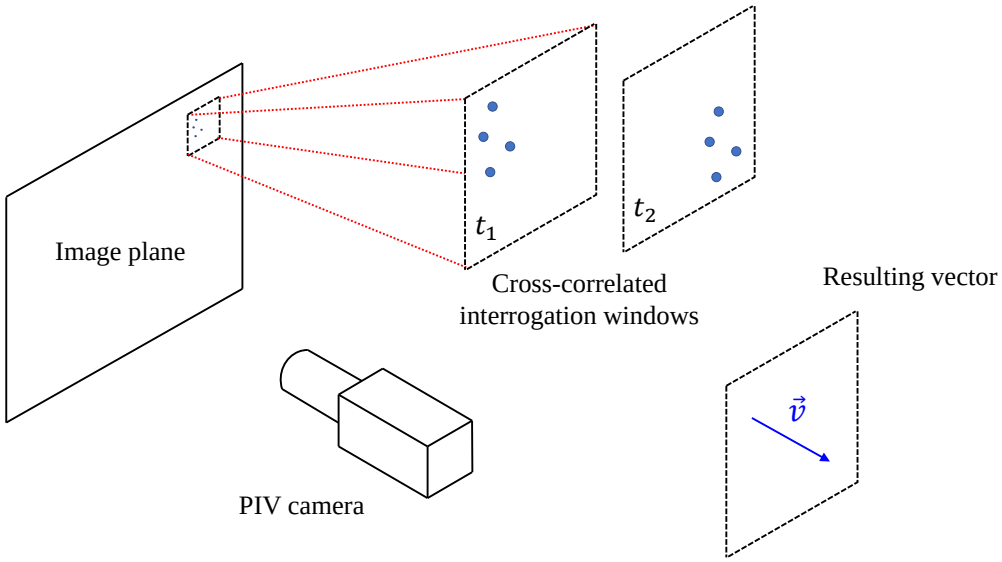

Figure 2.7: Schematic representation of the two-component PIV process where t_1 and t_2 denote the time of each image.

The displacement of the particles within each interrogation window is determined using a cross-correlation between windows in two subsequent images. The light intensity distribution of the interrogation windows within the first and second images are given by I_1 and I_2, and subtracting the mean intensity $\langle I_i \rangle$ of each window gives:

$$I_1' = I_1 - \langle I_1 \rangle, \quad I_2' = I_2 - \langle I_2 \rangle. \tag{2.5}$$

The normalized cross-correlation is then applied:

$$C(\Delta x, \Delta y) = \frac{\langle I_1'(x_0, y_0) \cdot I_2'(x_0 + \Delta x, y_0 + \Delta y) \rangle}{I_{1,rms}'(x_0, y_0) I_{2,rms}'(x_0, y_0)} \tag{2.6}$$

where the subscript rms denotes the root-mean-square operation and $(\Delta x, \Delta y)$ is the shift of the interrogation window. This process results in a correlation map with a distinct peak. The location of the peak represents the most probable displacement of the group of particles. A sample of two 32×32-pixel interrogation windows containing particles and the resulting correlation map between the two windows is given in Figure 2.8. A clear shift to the right is visible between the interrogation windows, and this is evident in the correlation map as well. It is recommended that more than 10 particles be present in each interrogation window for two-component PIV (Keane and Adrian, 1992).

The accuracy of two-component PIV can be improved through the use of a multi-pass cross-correlation method. The displacements obtained from one pass of the cross-correlation method are used to determine where the second interrogation window should be located for the following pass. This acts to increase the number of common particles between interrogation windows, resulting in an improved correlation. It is typical to use two or more passes with interrogation windows of decreasing size when evaluating two-component PIV images. Further accuracy increases can be obtained by deforming interrogation windows relative to the local shear rate (Scarano and Riethmuller, 2000).

2.3.2 Tracer Particles

Since PIV methods rely on the evaluation of particle images, the fidelity of the tracer particles is critical. An ideal tracer faithfully follows the flow field while being large enough

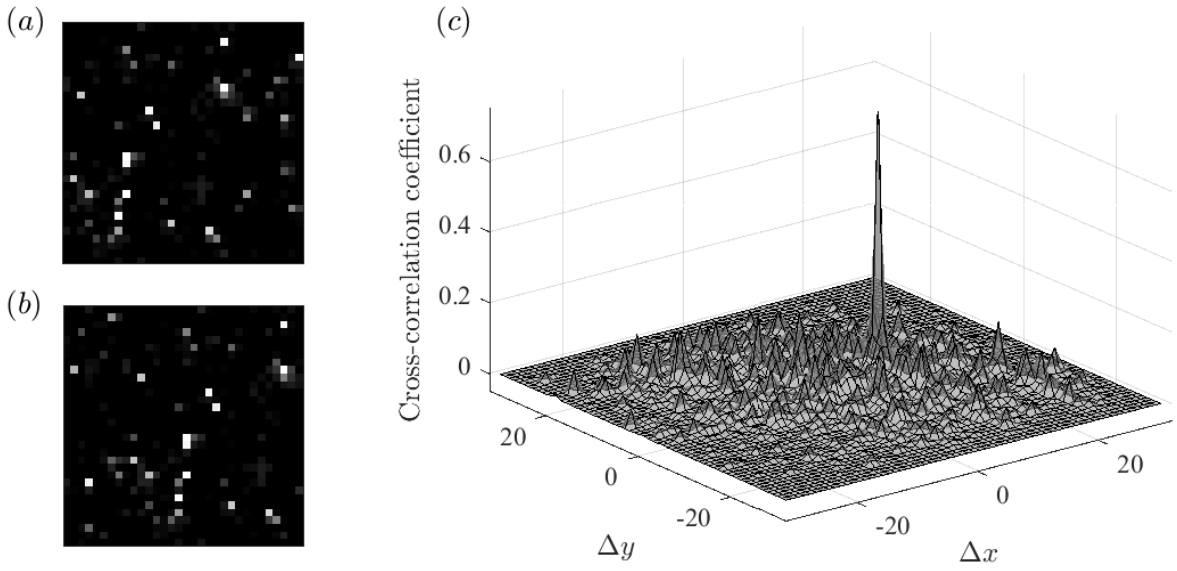

Figure 2.8: Sample 32×32-pixel interrogation windows for cross-correlation at (a) $t = t_0$ and (b) $t = t_0 + \Delta t$. The correlation map between the two windows is shown in (c). Note that this cross-correlation returned a shift of 8 pixels to the right (Δx) between the two windows; this shift is visible between the frames.

to scatter sufficient light for imaging; however, these requirements are often competing because larger particles are more likely to deviate from the true flow field. Assuming a spherical particle, the Reynolds number of a tracer is defined as:

$$Re_p = \frac{\rho(U_p - U)d}{\mu} \tag{2.7}$$

where ρ and μ are the density and dynamic viscosity of the surrounding fluid, U_p and U are the particle and fluid velocities, and d is the diameter of the particle. Typical flow tracers have $Re_p < 1$ and are therefore dictated by Stokes' law. The corresponding Stokes' drag is:

$$F_d = 3\pi\mu d(U_p - U). \tag{2.8}$$

Newton's second law is then applied to obtain the equation of motion for the tracer particle:

$$\frac{\pi}{6}d^3(\rho_p - \rho)\frac{dU_p}{dt} = -3\pi\mu d(U_p - U) \tag{2.9}$$

where ρ_p is the density of the particle. Equation 2.9 reveals that a particle with the same density of the surrounding fluid (i.e. neutrally buoyant) will result in ideal flow tracing.

Obtaining neutrally buoyant particles for use in liquid flows is straightforward due to their high densities. In gasses such as air, neutral buoyancy is not as easy to achieve (Kerho and Bragg, 1994; Scarano et al., 2015).

Tracer particles commonly used in air typically have diameters on the order of 1 μm and are three orders of magnitude more dense (Melling, 1997). Assuming that the density of air is negligible compared to the tracer particle, Equation 2.9 can be re-written as:

$$\frac{dU_p}{dt} = -\frac{18\mu}{\rho_p d_p^2}(U_p - U) = -\frac{1}{\tau_p}(U_p - U) \tag{2.10}$$

where τ_p is the time response of the tracer particle. Tracers with a time response that is more than an order of magnitude smaller than that of the characteristic time scale of the flow will have tracing errors of less than 1% (Tropea et al., 2007). Standard 1 μm particles used in air (e.g. the glycol-water droplets used in the present experiments) have time responses on the order of 1 μs (Ragni et al., 2011).

Another important characteristic of flow tracers is their light scattering ability, as they must scatter enough light to be visible to the cameras. A particle with a diameter larger than the wavelength of incident light (λ) is said to scatter light according to Mie's theory (Raffel et al., 2007). Mie scattering is characterized by a normalized diameter q:

$$q = \frac{\pi d_p}{\lambda}. \tag{2.11}$$

The average scattering intensity increases with q^2 (and therefore d_p^2), highlighting the benefit of using larger tracer particles. For q greater than 1, there are roughly q local maximums between 0° and 180° on the polar light scattering distribution for that particle. An example of a polar distribution is given in Figure 2.9, where a typical Mie scattering pattern is observed. It is important to note that several orders of magnitude more light is scattered in the forward direction with respect to the incoming light. This fact can be exploited to improve light intensity during experiments.

2.3.3 Imaging

Image quality is an important factor in PIV processing, as it is the images that contain the velocity field information that we wish to extract. PIV images are recorded using one or

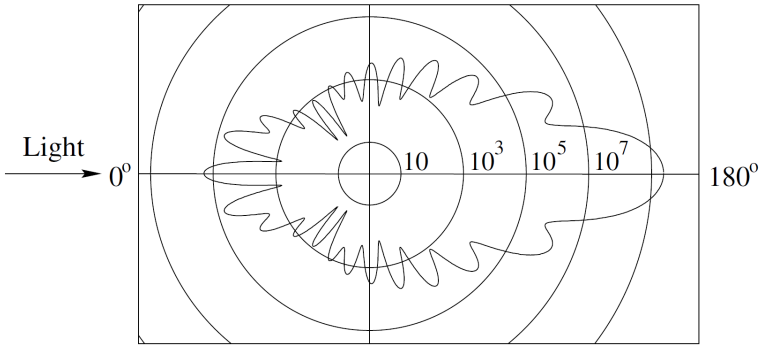

Figure 2.9: Polar distribution of light scattering from a 1 μm oil droplet in air. Taken with permission from Raffel et al. (2007).

more cameras and a light source. Lasers are most commonly used for their high intensity light output, easily manipulated beam, and short pulse width. The cameras are set at a distance from the illuminated particles and with lenses that determine the magnification of the resulting images (M, defined as the ratio between the image and object sizes).

The observed size of a particle in an image is a function of both optical and diffraction-limited imaging:

$$d_{img} = \sqrt{d_{opt}^2 + d_{dif}^2} \tag{2.12}$$

where d_{img}, d_{opt}, and d_{dif} are the particle diameters in the image and due to optical and diffraction-limited imaging, respectively. The particle size due to optical imaging can be approximated by:

$$d_{opt} = M d_p \tag{2.13}$$

and can therefore be neglected for typical particles with $d_p \approx 1\mu$m. The particle size due to diffraction-limited imaging can be approximated by:

$$d_{dif} = 2.44 f_{\#}(M+1)\lambda \tag{2.14}$$

where $f_{\#}$ is the ratio between the lens focal length and aperture diameter (the aperture setting). Observed particle diameters larger than 1 pixel are desired to avoid errors caused by uncertain particle locations.

2.3.4 Stereoscopic Measurements

In many flow measurement applications it is desirable to obtain all three velocity components of a moving fluid. Stereoscopic PIV (stereo-PIV) measurements allow for obtaining the out-of-plane component that is not possible to obtain using standard planar techniques. Stereo-PIV typically employs two cameras set at angles with respect to the imaging plane, thus allowing each of them to capture some portion of the out-of-plane motion. The cameras can be set in any desirable configuration as long as both can view the imaging plane and the two imaging axes are not collinear. To maximize image quality, the Scheimpflug lens condition is often necessary for improving focusing across the imaging plane (Prasad and Jensen, 1995).

The complicated camera arrangement associated with stereo-PIV requires special considerations. A three-dimensional target calibration is required to accurately map the images to the plane of interest. This is achieved using multi-level targets or translating a planar target, and any misalignment between the laser and target planes is corrected using a disparity correction (Wieneke, 2005). The mapping derived from calibration allows for projecting the images from both cameras onto a common grid in space. Two-component PIV processing techniques can be used on the images from both cameras, and then a least-squares technique is applied to solve for the three velocity components using the two-dimensional vectors from each camera view. The residuals from this least-squares fit are generally used as a measure for the quality of the results.

2.4 Measurement of Pressure Fluctuation

2.4.1 Microphones

The ability to measure pressure within a fluid is important for both the industry and research sectors. This is typically achieved using pressure sensors or microphones, depending on the application. Pressure sensors allow for the measurement of instantaneous pressure while microphones only record the fluctuating component. In the context of this thesis, pressure fluctuations in the wake are indicative of the strength and frequency of the vortex shedding

pattern.

Electret condenser microphones are employed in the present investigation to measure pressure fluctuations. This type of microphone contains a parallel-plate capacitor made up of a back plate and a diaphragm, one of which contains a permanent electric charge. Incoming pressure waves cause the diaphragm to deflect, resulting in a change in capacitance and a corresponding change in the measured voltage signal. This voltage signal is representative of the the pressure fluctuations in the fluid. Microphones are typically evaluated based on their sensitivity [V/Pa], frequency range [Hz], and dynamic range [dB].

2.4.2 Ambient Laboratory Noise

A portion of the microphone signals may contain contamination from ambient laboratory noise during experiments. An order of magnitude analysis can be used to determine the impact of this noise on the resulting measurements. The measured noise level in dB is calculated using:

$$20 \log \left(\frac{P}{P_{ref}} \right) \tag{2.15}$$

where P is the measured sound pressure level and P_{ref} is the reference sound pressure level corresponding to the threshold of human hearing (20 μPa). Hearing loss in humans can occur during prolonged exposure at 85 dB, so this will be the assumed maximum ambient noise level in the laboratory. This value corresponds to $P = 0.4$ Pa. Bernoulli's principle can then be employed to estimate the corresponding pressure difference caused by a fluid flow:

$$\Delta P = \frac{1}{2} \rho V^2. \tag{2.16}$$

Assuming a change in fluid velocity of 5 m/s, this corresponds to $\Delta P = 15$ Pa in air. The contamination of the microphone signal caused by the maximum ambient laboratory noise is therefore nearly two orders of magnitude less than the expected signal caused by the flow field.

2.5 Proper Orthogonal Decomposition

2.5.1 Overview

Proper orthogonal decomposition (POD) is a useful mathematical tool for obtaining reduced-order representations of data. It has been applied in areas of science such as image processing and data compression, and is particularly useful for the study of coherent structures in the context of fluid dynamics (Berkooz et al., 1993). The result is a set of optimal modes and time-varying coefficients which can be used to reconstruct a data ensemble using linear combinations. The modes are arranged in terms of energy content, making it straightforward to determine which flow characteristics are the most important. POD is a linear procedure, is statistical in nature, and makes no assumptions about the linearity of the problem at hand, making it an excellent choice for the study of turbulent flows. The 'method of snapshots' first proposed by Sirovich (1987) and outlined by Graftieaux et al. (2001) will be presented here and applied throughout this thesis.

2.5.2 Mathematics

An unsteady flow can be represented in terms of an ensemble of N velocity field snapshots $\boldsymbol{U}^{(i)}$, $i = 1, 2, \ldots, N$. Each snapshot can be decomposed into a mean and a fluctuating component:

$$\boldsymbol{U}^{(i)} = \langle \boldsymbol{U} \rangle + \boldsymbol{u}^{(i)} \tag{2.17}$$

where $\langle \cdot \rangle$ denotes an ensemble average. The fluctuating component $\boldsymbol{u}$ is further decomposed into a linear combination of optimal modes $\boldsymbol{\psi}$:

$$\boldsymbol{U}^{(i)} = \langle \boldsymbol{U} \rangle + \sum_{j=1}^{N} a_{i,j} \boldsymbol{\psi}^{(j)}. \tag{2.18}$$

Obtaining the modes and the corresponding coefficients is the focus of POD. Once obtained, the ensemble of snapshots can be reconstructed using a truncated number of modes, thus preserving a selected fraction of the energy content from within the original ensemble.

First, it is necessary to define the symmetric correlation matrix $\boldsymbol{C}$:

$$\boldsymbol{C}_{i,j} = \frac{1}{N} (\boldsymbol{u}^{(i)}, \boldsymbol{u}^{(j)}) \tag{2.19}$$

where the inner product is denoted by $(\cdot, \cdot)$. Diagonalization of $\boldsymbol{C}$ leads to N positive eigenvalues λ_m and the corresponding eigenvectors $\boldsymbol{V}_m$. The eigenvalues and eigenvectors are then arranged in descending order with respect to λ_m: $\lambda_1 \geq \lambda_2 \geq \ldots \geq \lambda_N \geq 0$. Each eigenvalue represents the contribution of energy captured by the corresponding mode, and therefore the portion of energy captured by mode m of N is given by:

$$E_m = \frac{\lambda_m}{\sum_{i=1}^{N} \lambda_i}. \tag{2.20}$$

The spatial modes $\boldsymbol{\phi}$ are the linear combination of $\boldsymbol{V}$ and $\boldsymbol{u}$:

$$\boldsymbol{\phi}^{(m)} = \boldsymbol{u}\boldsymbol{V}^{(m)} \tag{2.21}$$

which are then normalized to obtain an orthonormal basis (i.e. the POD modes):

$$\boldsymbol{\psi}^{(m)} = \frac{\boldsymbol{\phi}^{(m)}}{[(\boldsymbol{\phi}^{(m)}, \boldsymbol{\phi}^{(m)})]^{1/2}}. \tag{2.22}$$

Finally, the mode coefficients are obtained through the projection of $\boldsymbol{u}$ onto the POD modes:

$$a_{i,j} = (\boldsymbol{u}^{(i)}, \boldsymbol{\psi}^{(j)}). \tag{2.23}$$

Chapter 3

Experimental Setup

This chapter outlines all aspects of the present experiments. This includes the wind tunnel facility, blunt body model, particle image velocimetry (PIV) setups, and modifications for active control. The measurements from Experiment 1 are presented in Chapter 4, and the measurements from Experiment 2 are presented in Chapter 5.

3.1 Wind Tunnel Facility

All experiments within this thesis were conducted in a closed-loop, two-story wind tunnel located in the Mechanical Engineering Building at the University of Alberta. The test section of the wind tunnel is rectangular with cross-sectional dimensions of 2.4×1.2 m^2 ($W \times H$) following honeycombs, several screens, and a contraction ratio of 6.3:1. The side walls are made of transparent acrylic and the floor and ceiling have been fit with either glass or acrylic windows in select locations for PIV. The facility is capable of flow speeds up to 35 m/s and hotwire measurements have shown that the freestream turbulence intensity at the midpoint of the test section is consistently less than 0.4% when the speed is above 2 m/s (Johnson and Kostiuk, 2000). A photograph of the wind tunnel test section is presented in Figure 3.1.

Figure 3.1: Photograph of the wind tunnel test section.

3.2 Blunt Body Model

The elongated blunt body model used for all experiments was machined from an aluminum plate and sanded to a fine surface finish. It has a blunt trailing edge (BTE) height $h = 12.9$ mm and a chord length $c = 600$ mm, resulting in an aspect ratio of $AR = 46.5$. The leading edge was made semi-elliptical with a major to minor axis ratio of 5:1 to prevent leading edge flow separation, and 1 mm tripping wires were attached to the surface 105 mm downstream from the leading edge on both sides of the model to uniformly trigger transition along the span. The model was oriented at zero angle of attack, spanning the entire 1.2 m from floor to ceiling to produce a blockage ratio of 0.5%. The rear section of the model is removable to accommodate experiments with both plain and modified trailing edges. The blunt body model mounted in the test section can be viewed in Figure 3.2.

3.3 Experiment 1

Experiment 1 was used for the analyses presented in Chapter 4. The boundary layer and wake flows near the BTE of the blunt body model were measured using separate PIV configurations which included two planar (2C-PIV) and two stereoscopic (stereo-PIV) measurements in three orthogonal viewing planes. They were conducted at freestream velocities

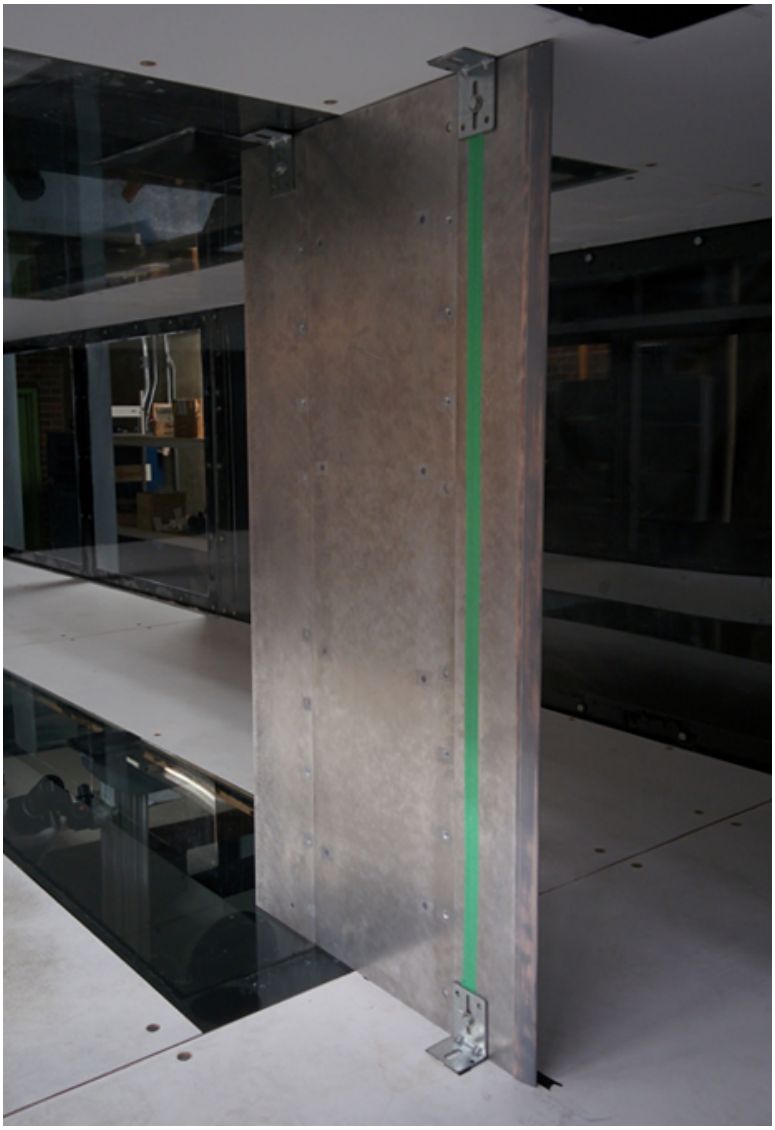

Figure 3.2: Photograph of the blunt body model mounted within the test section. The green strip near the leading edge of the model represents the location of the trip wire.

of 2.3, 4.3, 6.3, 8.4, and 10.4 m/s, corresponding to Reynolds numbers of $Re(h) = 1900$, 3500, 5200, 7000, and 8700 where h is the BTE height of the model. A schematic of the PIV experiments is given in Figure 3.3.

3.3.1 Two-Component Particle Image Velocimetry

A 2C-PIV system was utilized in two configurations to measure instantaneous velocity fields of the upstream boundary layer in the x-y plane (denoted as FOV1) and the low-speed zones near the BTE in the x-z plane (denoted as FOV2). The illumination was provided by an Nd:YAG laser (Spectra-Physics, PIV-400-10) that is capable of outputting 532 nm light at 400 mJ per pulse with a pulse width of 5-8 ns. The laser beam was shaped using one negative cylindrical and two spherical lenses to produce a laser sheet with a thickness of 1 mm. The resulting laser sheet was then directed as necessary using several adjustable mirrors. Imager ProX-4M cameras were used to collect images, each featuring a 2048×2048-pixel CCD sensor with a 7.4×7.4 μm^2 pixel size and 14-bit resolution. A schematic representation of the 2C-PIV setup is included in Figure 3.3.

The boundary layer within FOV1 was imaged at a distance of $7h$ upstream from the BTE at centre span. A Nikon lens with a focal length of $f = 200$ mm and an aperture setting of $f/5.6$ was utilized with the camera which was set 0.7 m from the viewing plane, resulting in a digital resolution of 20.5 μm/pix and a streamwise-wall-normal FOV of (Δx, Δy) = 42×42 mm^2 ($3.3h \times 3.3h$). The flow was seeded with 1 μm particles using a fog generator, and then 500 double-frame images were collected at a frequency of 4 Hz for each flow speed considered.

The low-speed zones in the boundary layer and wake regions of the flow were measured using FOV2 in the x-z plane at $y = 1.5$ mm above the surface. Two cameras were fit with identical Nikon lenses, each with $f = 200$ mm and aperture settings of $f/8.4$. They were placed side by side at a distance of 1.3 m from the viewing plane. The digital resolutions of the upstream and downstream cameras were 34.4 and 34.2 μm/pix, respectively, and the viewing regions overlapped by 5 mm so that the resulting vector fields could be stitched

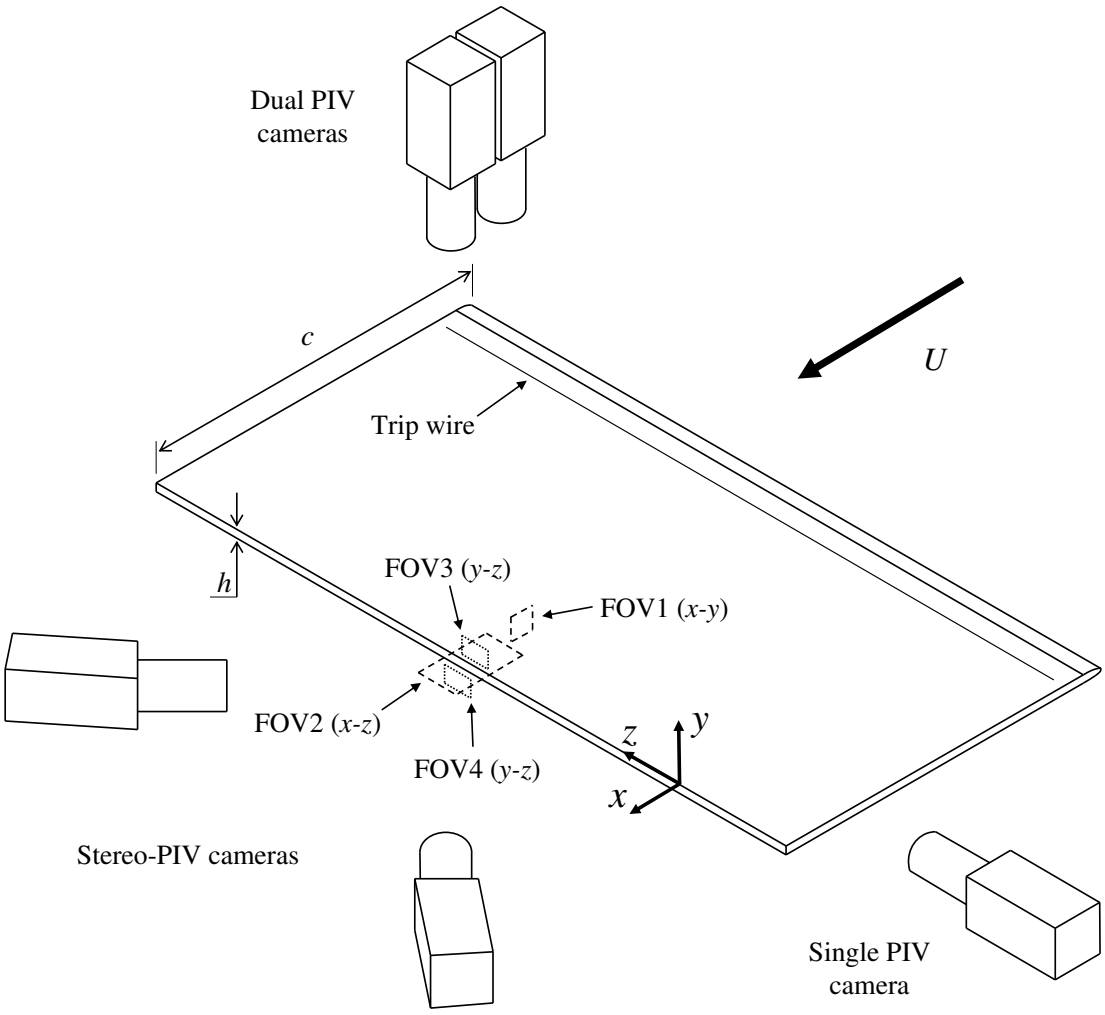

Figure 3.3: Schematic of Experiment 1. Note that $z = 0$ is located at centre span. The axis is offset here for clear viewing of the imaging planes.

together. The combined streamwise-spanwise FOV had dimensions of $(\Delta x, \Delta z) = 135 \times 70$ mm^2 ($10.5h \times 5.4h$) centred at $x = 0$ and at centre span. After seeding with 1 μm fog particles, sets of 5000 double-frame images were collected by both cameras simultaneously at a frequency of 4 Hz for each flow speed considered.

The images were processed using DaVis 8.2 software (LaVision GmbH). First, a pre-processing step was necessary to improve image quality. The minimum of each ensemble was subtracted to remove background noise, followed by normalization using ensemble averages. FOV1 was imaged to obtain mean velocity profiles, and so an ensemble-of-correlation was applied to these sets (Meinhart et al., 2000). A multi-pass algorithm was used with 24×24-pixel (0.49×0.49-mm) interrogation windows with 75% overlap for the final pass. A 4:1 elliptical Gaussian distribution was applied to the window with the major axis of the ellipse in the streamwise direction to improve the correlation. FOV2 was processed using a standard multi-pass cross-correlation with the final passes utilizing Gaussian 48×48-pixel (1.65×1.65-mm) interrogation windows with 75% overlap. A postprocessing step was applied to the wake ensembles using universal outlier detection (Westerweel and Scarano, 2005) and linear interpolation to account for incorrect and missing vectors, which made up less than 1% of each vector field.

3.3.2 Stereoscopic Particle Image Velocimetry

The wake and boundary layer regions were characterized using two different stereo-PIV systems. The first system utilizes the same laser and cameras as the 2C-PIV experiments and the second is high-speed for collecting time-resolved images. The high-speed system makes use of a dual-cavity Nd:YLF laser (Photonics Industries, DM20-527-DH) at 527 nm with a maximum frequency of 10 kHz. The combined beam of the two laser cavities is capable of outputting a maximum of 40 mJ per pulse (at 1 kHz) with a pulse width of 170 ns. Two Phantom v611 high-speed cameras were utilized, each with a 1280×800-pixel CMOS sensor with a 20×20 μm^2 pixel size and 12-bit resolution. The first stereoscopic y-z viewing plane (denoted as FOV3) was located $0.3h$ upstream from the BTE location at

centre span and began at the surface of the model ($y = 0$). The second stereoscopic y-z viewing plane (denoted as FOV4) was centred at $y = -0.5h$ and located $2h$ downstream from the BTE location as shown in Figure 3.3.

Snapshots of the flow in FOV3 and FOV4 were captured for statistical analysis with higher spatial resolution. The mean flow direction is perpendicular to these viewing planes and so the second laser sheet pulse was moved 0.5 mm downstream from the first in both FOV3 and FOV4 to improve the number of common particles captured between frames. Each laser sheet pulse had a thickness of 1.5 mm using the same combination of optics as used previously, resulting in a total laser sheet thickness of 2 mm centred at $x = -0.3h$ for FOV3 and at $x = 2h$ for FOV4. The stereo-PIV cameras were each set approximately 1 m from the FOVs and were fit with Scheimpflug mounts and Nikon lenses with $f = 200$ mm. An aperture setting of $f/11$ was used on the forward scattering camera, while a setting of $f/8.4$ was used on the camera with a backward scattering orientation. A two-step stereoscopic calibration process was used for both FOVs which included a three-dimensional target calibration followed by self-calibration with a small set of particle images (Wieneke, 2005). The spanwise-wall-normal FOV was $(\Delta z, \Delta y) = 76 \times 61$ mm^2 ($5.9h \times 4.7h$) with a digital resolution of 28.8 μm/pix and a residual error of 0.06 pix for FOV3. A spanwise-wall-normal FOV of $(\Delta z, \Delta y) = 75 \times 59$ mm^2 ($5.8h \times 4.6h$) with a digital resolution of 28.1 μm/pix and a residual error of 0.06 pix was obtained for FOV4. The flow was seeded with 1 μm particles using a fog generator and 5000 double-frame images were collected from each camera simultaneously at a frequency of 4 Hz for each flow speed considered and in both FOV3 and FOV4.

High-speed stereoscopic measurements were also conducted within FOV4 for the purpose of studying the temporal evolution of the vortices in the wake. The laser sheet was made to be 2 mm thick using the same combination of optics as before. The high-speed cameras were placed in the same location as the Imager ProX cameras in the previous stereoscopic experiment and with the same lenses and aperture settings. The previously mentioned stereoscopic calibration procedure was followed, resulting in a spanwise-wall-normal FOV

of $(\Delta z, \Delta y) = 115 \times 58$ mm^2 $(8.9h \times 4.5h)$ with a digital resolution of 71.6 μm pix^{-1} and a residual error of 0.02 pix. Ensembles of 5400 time-resolved images were collected at an acquisition frequency of 6.2 kHz for each flow speed considered.

All images were once again processed using DaVis 8.2 software (LaVision GmbH). The double-frame stereo-PIV images were cross-correlated using multiple passes, the last of which utilized Gaussian 96×96-pixel (2.70×2.70-mm) interrogation windows with 75% overlap. A postprocessing step was then applied which removed and replaced outliers and interpolated missing vectors. The incorrect and missing vectors accounted for less than 4% of each vector field. The high-speed stereo-PIV images were processed using a sliding ensemble-of-correlation algorithm with a filter length of 5 images using 4 successive pairs each with a time separation of $\Delta t = 161$ μs to reduce random, high-frequency noise (Ghaemi et al., 2012). The operation utilized a multi-pass cross-correlation with final Gaussian 48×48-pixel (3.44×3.44-mm) interrogation windows with 75% overlap. No postprocessing was performed on the resulting time-resolved vector fields.

3.4 Experiment 2

The trailing edge of the blunt body model has been modified for control purposes and studied in the wind tunnel. Pressure fluctuation measurements and high-speed PIV have been utilized to study the wake with and without active control being applied. The experiments were conducted at $Re(h) = 2600$ where h is the height of the BTE. The results are presented in Chapter 5.

3.4.1 Modified Blunt Trailing Edge

The BTE has been modified for control as depicted in Figure 3.4. Note that the spanwise direction is denoted by z and $z = 0$ is centre span. Both sides of the BTE feature cantilevered flaps that are used to interact with the flow. They are made of 0.005-inch stainless-steel sheets that span 10 cm and are flush-mounted with the surface of the blunt body model when not actuated. The inner surface of each flap is adhered to five piezoelectric bending actuators

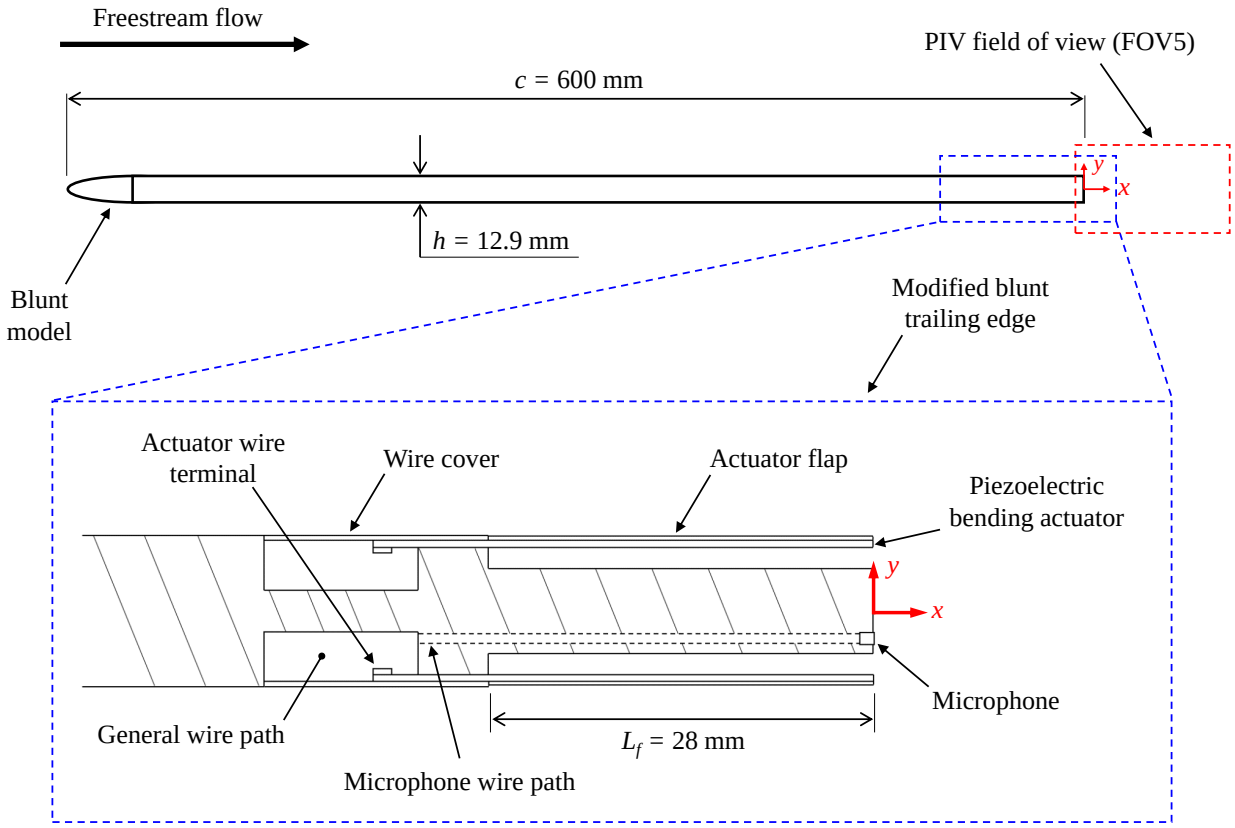

Figure 3.4: Schematic of Experiment 2 and sectional view of the modified BTE. Note that the z-coordinate runs in the spanwise direction with $z = 0$ located at centre span.

(PI Ceramic, PICMA PL128.10), and each actuator has dimensions of $36 \times 6.3 \times 0.75$ mm^3 ($L \times W \times T$). The manufacturer reports a resonant frequency of 360 Hz and a maximum tip displacement of 0.9 mm. Each set of five actuators acts in unison to displace the free end of one flap, and the free length of each actuator/flap construction is $L_f = 28$ mm. A relatively short span of the BTE is actuated, but it has been shown that control of vortex shedding within a small spanwise cell is possible because the flow in adjacent cells is uncorrelated (Roussopoulos, 1993). Two 1/8-inch microphones (Knowles, FG-23629-P16) have been installed to measure the fluctuation in pressure at the surface of the BTE. The microphones are placed at $z = \pm 1$ cm in the spanwise direction and are biased towards one side of the trailing edge so that the phase of the nearest shear layer can be monitored if desired (e.g. Pastoor et al., 2008). All microphone signals have been sampled at a rate of 500 Hz, corresponding to roughly $10\times$ the natural wake frequency for the investigated Re. An I/O board (dSPACE, 1103) has been utilized along with Simulink (MATLAB) and Control Desk (dSPACE) to realize real-time implementation of the actuators and microphones. A photograph of the modified BTE is presented in Figure 3.5.

3.4.2 High-Speed Particle Image Velocimetry

Two-component, high-speed PIV has been conducted to evaluate the impact of the actuators on the flow. A dual-cavity Nd:YLF laser (Photonics Industries, DM20-527-DH) was used with a combination of spherical and cylindrical lenses to produce a laser sheet located at centre span ($z = 0$) with a thickness of 2 mm. Each cavity of the laser emits light at 527 nm with a pulse width of 170 ns. The pulses from both cavities can be combined to produce 40 mJ per pulse at 1 kHz, or can be used in an alternating fashion to obtain frequencies up to 20 kHz with lower power. A high-speed camera (Phantom, v611) featuring a 1280×800-pixel CMOS sensor (20×20 μm^2 pixel size, 12-bit resolution) was used to collect time-resolved images. A Nikon lens with a focal length of $f = 200$ mm and an aperture setting of $f/4$ was used to obtain a FOV of $(\Delta x, \Delta y) = 91 \times 57$ mm^2 ($7.0h \times 4.4h$) with a digital resolution of 70.8 μm/pix. Sets of 5400 single-frame images were collected at a frequency of 5 kHz

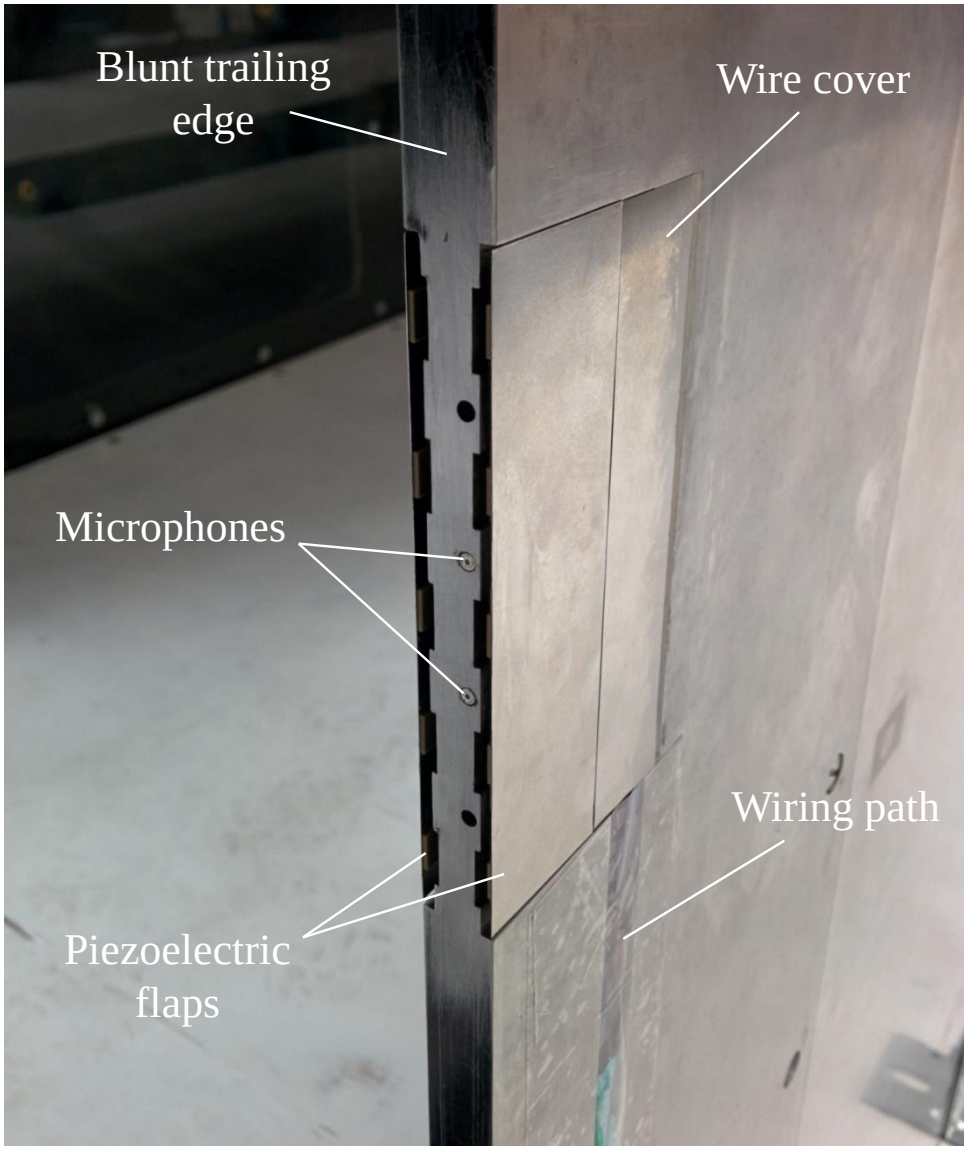

Figure 3.5: Annotated photograph of the modified BTE for control.

for the unforced wake and for numerous actuation cases. The FOV used for PIV has been denoted as FOV5 and is visible in Figure 3.4.

The collected images were processed using DaVis 8.2 software (LaVision GmbH). The minimum of the collected ensembles was subtracted to reduce background noise and the resulting images were divided by ensemble averages for normalization. The preprocessed images were cross-correlated using a multi-pass algorithm that utilized 48×48-pixel (3.40×3.40-mm) interrogation windows with 75% overlap for the final pass. Two images were correlated to obtain each vector field, resulting in 5399 vector fields per collected ensemble. No postprocessing was applied to these vector fields.

3.4.3 Actuator Dynamics and Actuation Methods

The piezoelectric flaps are resonant devices, i.e. they are limited by their own resonant frequency. It is necessary to determine this frequency to avoid actuating in a self-destructive manner. This has been done using the same high-speed camera that was used for PIV and with the same lens. A lens extension system was employed to obtain an improved resolution of 22.4 μm/pix. The camera was then used to collect time-resolved images of the piezoelectric flap tip displacement (d_{tip}) as a function of actuation frequency (f_a). The actuators were driven by a zero-mean sinusoid with the maximum actuation voltage of $V_a = \pm 30$ V for this analysis. The resulting frequency response is given in Figure 3.6, where it is evident that the resonant frequency of the piezoelectric flap is approximately 215 Hz. Note that this is below the manufacturer-reported resonant frequency of each actuator (360 Hz), and this is expected because the stainless-steel flaps add mass to each system of five actuators. The maximum frequency used to drive the piezoelectric flaps for all analyses from here forward is $f_{a,max} = 180$ Hz. This corresponds to a maximum tip displacement of 0.9 mm and therefore all actuation is sub-millimetre. This is important for minimally invasive actuation, as large flap protrusions into the flow may cause unwanted drag.

Three different open-loop actuation methods are explored in this work. These are sym-

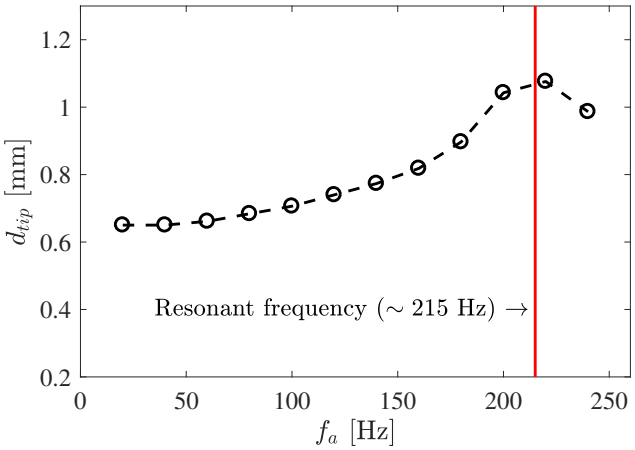

Figure 3.6: Frequency response of the piezoelectric flap construction. The tip displacement (d_{tip}) was measured using a calibrated high-speed camera with a resolution of 22.4 µm/pix, and the piezoelectric flap was driven using a sinusoid of maximum amplitude ($\pm$30 V).

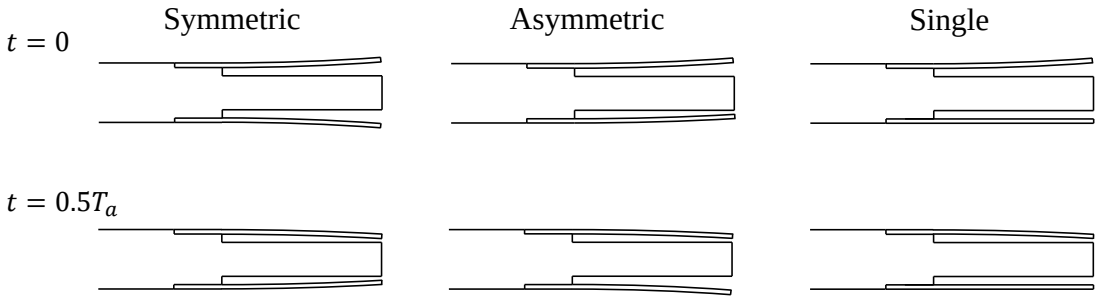

Figure 3.7: Schematic representation of the symmetric, asymmetric, and single actuation methods. Note that T_a is the period of actuation.

metric, asymmetric, and single actuation, and have been named for their movement with respect to the wake centre line (the x-axis in Figure 3.4). Schematic representations of all three actuation methods are given in Figure 3.7. Actuation has been generated using a zero-mean sinusoid for all cases moving forward, and only the amplitude and frequency were modified. The first row of five piezoelectric actuators driving one flap received the same input voltage signal. Sending the same signal to the second row of actuators results in symmetric actuation. The second signal was either phase shifted by π radians or removed altogether to obtain asymmetric or single actuation, respectively.

3.4.4 Surface-Pressure Measurements

The two microphone signals were averaged to obtain a measure of base pressure fluctuation at centre span, denoted as P'. The power spectral density (PSD) of P' has been determined for the natural wake at $Re(h) = 2600$ to obtain the unforced vortex shedding frequency. This value is $f_u = 49.5$ Hz and corresponds to a Strouhal number of $St(h) = 0.20$. This St is similar to the values reported in the wakes of circular cylinders (Roshko, 1954), and slightly smaller than other reported values in the wake of a BTE (Petrusma and Gai, 1996).

The actuators produce acoustic noise at their driving frequency and this noise is measured by the microphones at the BTE. Despite this, it is possible to monitor the frequency component of the wake corresponding to vortex shedding using PSD if the actuation frequency is known. This is evident when looking at the sample PSD of P' in Figure 3.8, where clear peaks exist for both the unforced wake frequency ($f_u = 49.5$ Hz) and the actuation frequency used for the sample ($f_a = 30$ Hz). The plot reveals that the pressure fluctuations in the wake caused by vortex shedding and the acoustic noise produced by the actuators are the only sources with a significant contribution to the microphone signal. The unsteady wake can be said to be suppressed if the peak for f_u is no longer present in the spectrum.

The strength of vortex shedding in the near-wake as measured by the microphones can be monitored using a suppression variable (σ) defined as:

$$\sigma = 10 \log \left(\frac{||P'_a||}{||P'_u||} \right) \tag{3.1}$$

where $||P'_a||$ is the magnitude of the peak in the PSD corresponding to vortex shedding while actuation is being applied, and $||P'_u||$ is the magnitude of the peak in the PSD corresponding to vortex shedding in the unforced wake. Note that a value of $\sigma = 0$ dB represents zero suppression of the unsteady wake, and that the suppression variable cannot be evaluated near $f_a = f_u$ due to overlap of the peaks.

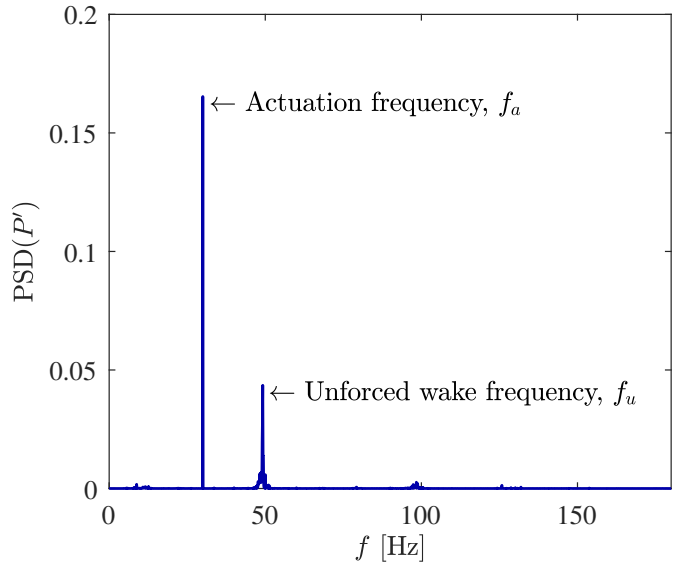

Figure 3.8: Power spectral density (PSD) of P' at $Re(h) = 2600$ for symmetric actuation at 30 Hz. The plot indicates that the pressure fluctuations caused by vortex shedding and the acoustic actuation noise are the only significant contributors to the microphone signal.

Chapter 4

Analysis of Secondary Instabilities in the Wake

Following Experiment 1 (Section 3.3), this chapter begins by characterizing the state of boundary layer upstream from the blunt trailing edge (BTE) to ensure the selected Reynolds numbers (Re) cover the laminar, transitional, and turbulent upstream cases of interest. The wavelength of the secondary instability is then statistically investigated by applying an auto-correlation technique to the vorticity field. The spatio-temporal symmetry of the wake is investigated both qualitatively and statistically using time-resolved measurements. Together, these analyses fully characterize the spatio-temporal behaviour of the secondary vortices. The relationship between the secondary instability and the upstream boundary layer is explored by tracking the spacing and evolution of the low-speed structures in the boundary layer as they move past the BTE and by determining the strength of the streamwise vortices in both the boundary layer and wake. Finally, the proper-orthogonal-decomposition-based analysis used by Naghib-Lahouti et al. (2012, 2014) is applied here to compare the present results with previous estimations of the secondary instability wavelength.

4.1 Upstream Boundary Layer Development

The mean boundary layer profiles $7h$ upstream from the BTE for all Re are presented on both linear and semi-logarithmic axes in Figures 4.1a and 4.1b, respectively. The high spatial resolution of the two-component particle image velocimetry (2C-PIV) measurements from

$Re(h)$	$Re(L)$	U [m/s]	λ_0 [μm]	δ_{99} [mm]	δ^* [mm]	θ [mm]	H
1900	75000	2.3	187	9.8	3.3	1.3	2.49
3500	140000	4.3	115	7.0	2.3	0.9	2.54
5200	205000	6.3	76	8.3	1.8	0.8	2.14
7000	276000	8.4	44	12.0	2.0	1.3	1.50
8700	342000	10.4	38	11.4	1.9	1.3	1.50

Table 4.1: Parameters relating to the mean velocity profiles located $7h$ upstream from the BTE (from FOV1 in Figure 3.3). Note that L is the length of the model up to where these parameters were evaluated.

the ensemble-of-correlation technique in FOV1 allowed for calculation of the inner layer scales, including the wall unit λ_0, by fitting a line to the linear viscous sublayer of the mean profiles. The state of the upstream boundary layer is summarized in Table 4.1. By inspection of Figure 4.1*a* and the calculated shape factors (H, the ratio of displacement thickness to momentum thickness) in Table 4.1, it is evident that the upstream boundary layer is laminar for $Re(h) = 1900$ and 3500, transitional for $Re(h) = 5200$, and turbulent for $Re(h) = 7000$ and 8700.

It can be seen in Figure 4.1*b* that the turbulent boundary layer profiles at $Re(h) = 7000$ and 8700 do not follow the standard logarithmic 'law of the wall' for a zero pressure gradient (ZPG) turbulent boundary layer. In fact, both turbulent profiles clearly exceed the logarithmic line. This deviation can be attributed to the favourable pressure gradient (FPG) caused by the low-pressure near-wake region of the body. This mean profile behaviour is typical of FPG turbulent boundary layers due to their tendency to accelerate and relaminarize, causing the semi-logarithmic profiles to shift towards the laminar curves (Patel and Head, 1968; Badri Narayanan and Ramjee, 1969; Blackwelder and Kovasznay, 1972). This flow acceleration has been confirmed near the BTE using PIV measurements and the results can be found within Appendix A. The remainder of this investigation will only consider $Re(h) = 3500$, 5200, and 7000 as the laminar, transitional, and turbulent cases, respectively, to study the effect that a transitioning upstream boundary layer may have on the wake.

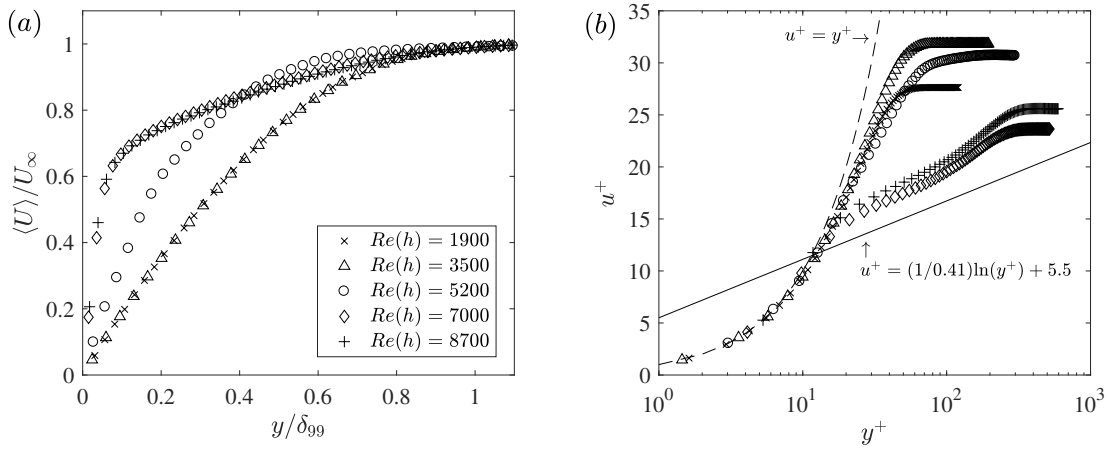

Figure 4.1: Mean velocity profiles $7h$ upstream of the BTE (FOV1) plotted using (a) linear and (b) semi-logarithmic axes. Both sets of profiles have been decimated by a factor of 2 to improve visibility of the data points. The direct overlap between laminar and turbulent profiles in (a) reveals that the flow is fully laminar at $Re(h) = 3500$ and fully turbulent at $Re(h) = 7000$. This is also corroborated from the shape factors (H) provided in Table 4.1.

4.2 Secondary Instability Wavelength

The spanwise distance between adjacent counter-rotating streamwise vortex pairs within the wake region must be determined to characterize the secondary instability modes. This distance is also known as the secondary instability wavelength as described previously and will be denoted as λ_z. The streamwise wake vortices have been identified from the stereoscopic snapshots of FOV4 using two-dimensional Q-criterion (Jeong and Hussain, 1995), where the partial derivative terms have been evaluated using a second-order central differencing scheme. All vortices, which are specified as regions of flow with $Q > 0$, were assigned a direction of rotation using the sign of streamwise vorticity (ω_x), and all $Q < 0$ were discarded. This was done to facilitate identification of the counter-rotating vortex pairs from within the stereoscopic snapshots. Sample snapshots of the fluctuating component of streamwise velocity (u) and the corresponding modified Q-criterion ($Q' = \omega_x Q/|\omega_x|$) are provided in Figure 4.2 for $Re(h) = 3500$, 5200, and 7000. These samples have been selected at instances when the stereoscopic particle image velocimetry (stereo-PIV) plane was cutting through one of the primary spanwise vortices to emphasise the location of the streamwise vortex

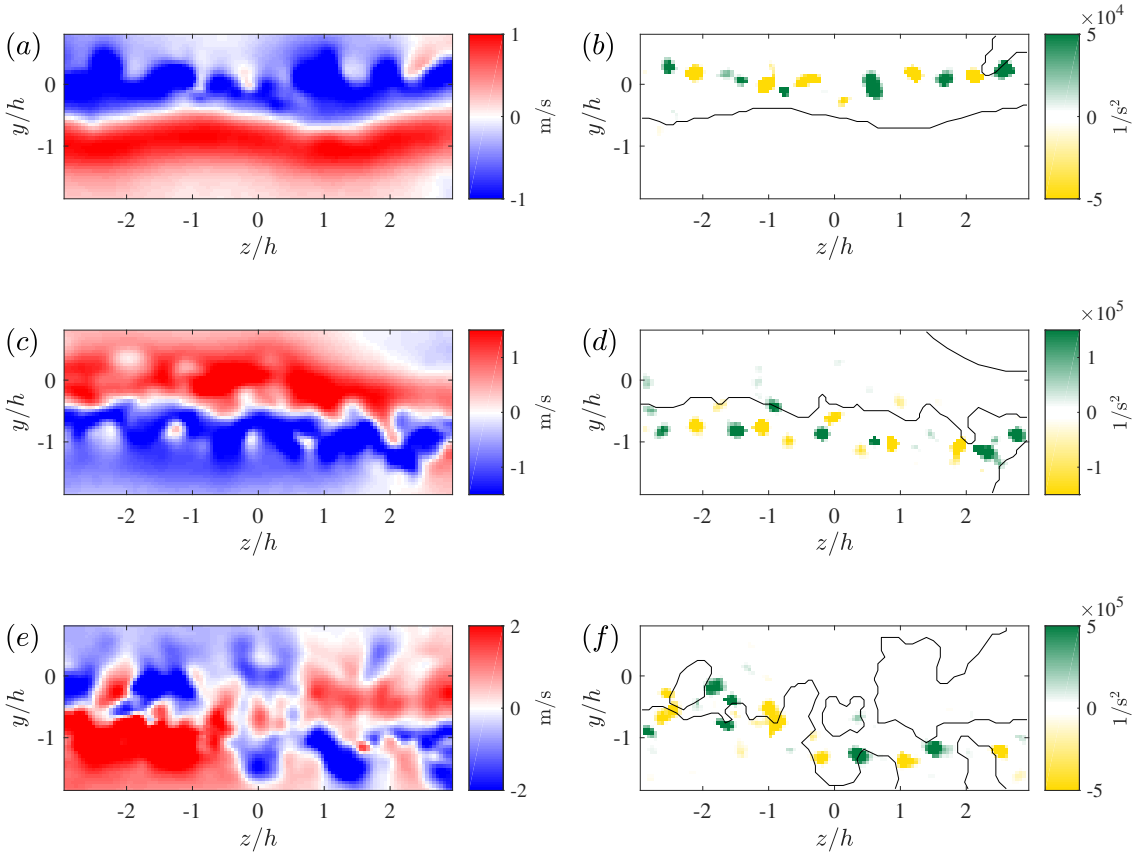

Figure 4.2: Instantaneous snapshots of the fluctuating component of streamwise velocity (u) and the corresponding modified Q-criterion ($Q' = \omega_x Q/|\omega_x|$) in the wake at $x = 2h$ for (a-b) $Re(h) = 3500$, (c-d) $Re(h) = 5200$, and (e-f) $Re(h) = 7000$. The $u = 0$ lines have been added to the contour plots of Q' to facilitate comparison between plots. The streamwise vortex pairs tend to exist either on the $u = 0$ line or in the region of the flow with $u < 0$.

pairs with respect to the primary vortex cores.

Figures 4.2a and 4.2c reveal a clear divide between positive and negative u at $Re(h) =$ 3500 and 5200. This divide occurs where the fluid has no out-of-plane motion with respect to the advecting frame of reference and is represented as a white line separating the red and blue regions of flow corresponding to positive and negative regions of u, respectively. The divide exists due to the rotation of the primary spanwise vortices, as they contain fluid moving both with ($u > 0$) and against ($u < 0$) the advecting frame of reference as the vortex moves downstream. In contrast, the isocontour of $u = 0$ for $Re(h) = 7000$ in Figure 4.2e

is highly jagged with engulfed regions of opposite velocity fluctuation on either side of the wake centre line ($y = -0.5h$). This is caused by intense distortion of the primary spanwise vortices as Re increases. Distortion of the primary vortices can be found throughout the collected data and becomes more prevalent as Re is increased.

The counter-rotating streamwise vorticity pattern of the secondary instability is easily identified in the stereoscopic snapshots of Q' presented in Figures 4.2b, 4.2d, and 4.2f. By comparison between the snapshots of u and Q', it is evident that the streamwise vortices of the secondary instability tend to exist either on the $u = 0$ line or in the region of the wake with $u < 0$. As previously mentioned, the latter corresponds to the portion of the primary spanwise vortex that is rotating upstream with respect to the advecting frame of reference. This streamwise vortex placement persists when the wake is distorted as can be seen in Figure 4.2f. The jagged interface between positive and negative u brings a similar jaggedness to the spanwise sequence of secondary vortices, with the streamwise vortices continuing to exist either on the $u = 0$ line or in the region with $u < 0$. This behaviour of secondary vortex pairs is consistent with the simplified mode B model that has been proposed by Brede et al. (1996) for the cylinder wake. Their model features simply connected streamwise vortex tubes which weave between primary spanwise vortices, always passing around the side of the primary vortex that is rotating towards the upstream direction. The streamwise vortices alternate sign in the spanwise direction, therefore existing in counter-rotating pairs, and have a secondary instability wavelength of approximately $1d$ as determined by their experiments. A similar model has been given by Williamson (1996b); however, the author stated that it was not obvious that the streamwise vortices were simply connected.

The spanwise distance between adjacent streamwise vortex pairs in the present stereoscopic snapshots has been calculated using a spatial autocorrelation in the spanwise direction. The operation has been applied to the snapshots of Q'. The autocorrelation coefficient of the i^{th} snapshot shifted in the spanwise direction by Δz is given by

$$C(\Delta z) = \frac{\langle Q'(y_0, z_0, t_i) \cdot Q'(y_0, z_0 + \Delta z, t_i) \rangle}{Q'_{rms}(y_0, z_0, t_i) Q'_{rms}(y_0, z_0 + \Delta z, t_i)} \tag{4.1}$$

where the subscript *rms* denotes the root-mean-square operation. The distance between adjacent vortex pairs within each snapshot was then taken to be twice the distance between the initial maximum value ($C(0) = 1$) and the first minimum of the respective autocorrelation. This minimum occurs when the snapshot has been shifted such that vortices with opposite signs align, and therefore it represents a distance that is half that of the secondary instability wavelength.

The process described above has been applied to all stereo-PIV ensembles. Probability density functions (PDFs) that have been fit to the resulting values of λ_z using a Burr type XII distribution (Tadikamalla, 1980) are shown in Figure 4.3. By inspection, each PDF of λ_z is unimodal and slightly right-skewed. The peaks represent estimates for the most probable values of λ_z and correspond to $0.72h$, $0.75h$, and $0.79h$ for $Re(h) = 3500$, 5200, and 7000, respectively. These values for λ_z closely match the secondary instability wavelength of mode B found in the wakes of cylinders (Williamson, 1996a) and the predicted wavelength of mode S$'$ for the wake of an elongated blunt body (Ryan et al., 2005). The distributions do not change significantly as the flow upstream from the BTE transitions from laminar to turbulent; however, a reduction in magnitude and shift of the peak to the right is visible. Each distribution being unimodal suggests that there is only one dominant mode in the wake for the investigated *Re*. Additionally, any dominant presence of the BTE mode B$'$ in the wake can be ruled out, as it has a secondary instability wavelength closer to $2.2h$.

4.3 Temporal Behaviour of the Streamwise Wake Vortices

The organization of the streamwise vortices in the wake must be determined to further characterize the secondary instability. In particular, knowledge of how the vortices relate from one primary shedding cycle to the next is required to distinguish between the cylinder mode B and the BTE mode S$'$. The two modes have similar fine-scale spanwise wavelengths; however, the mode B secondary vortices maintain their direction of rotation over many shedding cycles while the mode S$'$ secondary vortices change their direction of rotation between each cycle of the primary instability (Ryan et al., 2005). In the previous subsection,

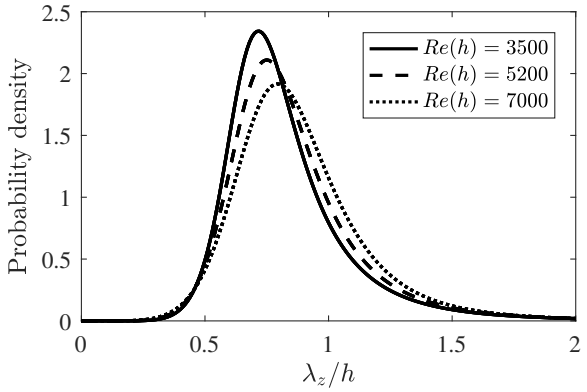

Figure 4.3: Probability density functions of secondary instability wavelength (λ_z) in the wake at $x = 2h$ for $Re(h) = 3500$, 5200, and 7000. The wavelengths were obtained by spatial correlation of vortex cores identified using a modified Q-criterion ($Q' = \omega_x Q/|\omega_x|$) as described by equation 4.1.

it was determined that the most probable secondary instability wavelength for the Re considered here is approximately $\lambda_z = 0.7$-$0.8h$. How the secondary vortices behave between primary shedding cycles is the last piece of information required to determine which mode is present in the wake.

High-speed stereo-PIV measurements have been performed within FOV4 at $x = 2h$ and the resulting time-resolved sequences of vector fields have been used to investigate the temporal characteristics of the streamwise wake vortices. The modified Q-criterion ($Q' = \omega_x Q/|\omega_x|$) has been determined as described in Section 4.2 to identify the streamwise vortex pairs within each stereoscopic velocity field. The resulting time-resolved evolution of Q' has been obtained by stacking the two-dimensional plots along the third dimension (i.e. time) to facilitate visualization of the vortical structures as they evolve temporally. Isosurface constructions of the vortical structures within the wake at $x = 2h$ are given in Figure 4.4 for $Re(h) = 3500$ and 7000. These plots are representative of the wake behaviour contained in all high-speed data collected in this study.

The alternating sign of vorticity in the spanwise direction is highly visible in the iso-surface constructions in Figure 4.4. Additionally, it is straightforward to see by visual inspection that many of the streamwise vortices in Figure 4.4*a* maintain their direction of

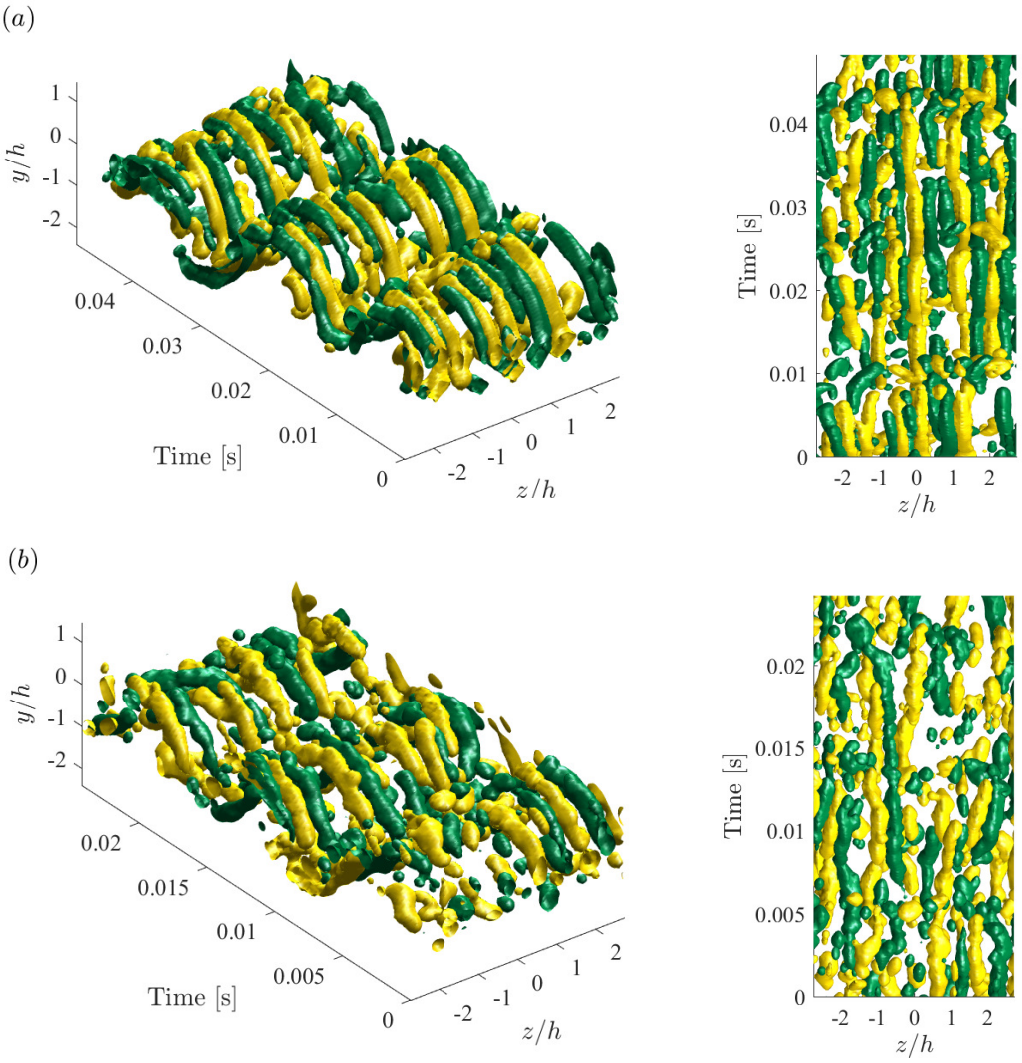

Figure 4.4: Isosurface constructions of modified Q-criterion ($Q' = \omega_x Q/|\omega_x|$) in the wake at $x = 2h$ for (a) $Re(h) = 3500$ (isosurface at $Q' = \pm 2000$ s^{-2}) and (b) $Re(h) = 7000$ (isosurface at $Q' = \pm 18000$ s^{-2}). Green and gold represent positive and negative rotational directions, respectively. Isosurface values have been chosen to obtain clear visualizations. Lowering the value makes the plots denser but does not alter the patterns displayed. Note that a second-order regression filter with a kernel size of 5 has been applied to the data to reduce noise and facilitate visualization.

rotation over the primary shedding cycles presented in the figure. This is not as easily visualized at higher Re when the wake region becomes more turbulent and three-dimensional. Thus, visual inspection of the vortex samples needs to be verified by statistical analysis. This has been done using a spatial cross-correlation in the spanwise direction, applied to the reconstructed temporal evolution of Q'. Subsequent vortex shedding cycles have been isolated as three-dimensional matrices and cross-correlated to determine whether the vortices change their direction of rotation between primary cycles. If the vortices maintain their rotational directions, the cross-correlation coefficient will begin at a positive value at $\Delta z = 0$ and trend towards a minimum with increasing Δz. This minimum will occur at a value of roughly $\Delta z = \lambda_z/2$ due to the alignment of vortices with opposite directions of rotation after the shift. However, the opposite will be true if the vortices are to change rotational direction between primary shedding cycles, i.e. the cross-correlation coefficient will begin at a minimum due to the alignment of vortices with opposite rotation and trend towards a maximum value at the location $\Delta z = \lambda_z/2$ where the vortices with the same rotational direction now align. This process has been applied to all N vortex shedding cycles for each Re considered and the resulting cross-correlation curves have been averaged. The mathematical description of the operation is given by

$$\rho(\Delta z) = \frac{1}{N-1} \sum_{i=1}^{N-1} \frac{\langle Q'(y_0, z_0, t_i) \cdot Q'(y_0, z_0 + \Delta z, t_i + T_{shed}) \rangle}{Q'_{rms}(y_0, z_0, t_i) Q'_{rms}(y_0, z_0 + \Delta z, t_i + T_{shed})} \tag{4.2}$$

where T_{shed} is the period of the primary vortex shedding cycle and Q' is a three-dimensional matrix containing a complete shedding cycle. The results for $Re(h) = 3500$, 5200, and 7000 are given in Figure 4.5. In agreement with the instantaneous visualizations in Figure 4.4, the averaged cross-correlation curves reveal that the streamwise vortices maintain their direction of rotation during primary shedding cycles since a maximum peak is observed at $\Delta z = 0$. Moreover, the first minimum in each plot occurs at about $\Delta z/h = 0.5$, confirming that the mean secondary instability wavelength is near $\lambda_z = 1h$ for the considered Re and therefore matches that of the cylinder mode B.

Upon further inspection of the isosurface constructions in Figure 4.4, it is evident that

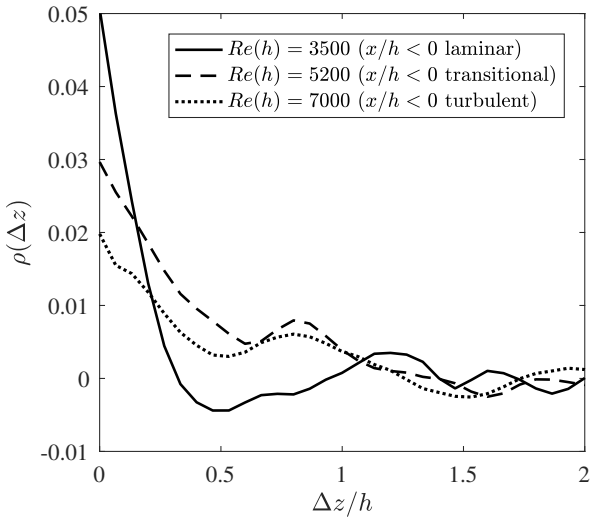

Figure 4.5: Average of spanwise cross-correlations applied to three-dimensional modified Q-criterion ($Q' = \omega_x Q/|\omega_x|$) between all subsequent primary vortex shedding cycles following Equation 4.2. All cross-correlation curves begin at a maximum positive value, indicating that the vortex pairs maintain their directions of rotation during primary shedding cycles. The first minimum of each curve is near $\Delta z/h = 0.5$, providing further evidence that the secondary instability wavelength is close to $\lambda_z = 1h$.

the streamwise vortices maintain their spanwise positions over time. This behaviour agrees with the models proposed by Brede et al. (1996) and Williamson (1996b) for the circular cylinder mode B; however, the behaviour contradicts the model proposed by Naghib-Lahouti et al. (2012) for the secondary instability in the wake of an elongated blunt body at a smaller aspect ratio (AR) of 12.5 based on LIF visualizations and reconstructed velocity fields. Their blunt body model contains streamwise vortices which stagger their spanwise positions every half shedding cycle, which is not observed here. Moreover, the streamwise vortices in Figure 4.4*a* appear to be simply connected as modelled by Brede et al. (1996), although it is difficult to confirm whether this behaviour is persistent in the wake.

Thus far, all results presented regarding the secondary wake vortices suggest that the cylinder mode B is the dominant secondary instability within the wake of the elongated blunt body studied here with $AR = 46.5$ for $Re(h) = 3500$, 5200, and 7000. No evidence of the BTE mode B$'$ nor S$'$ has been found within the collected data as was anticipated

from the stability analysis of Ryan et al. (2005) for $2.5 \leq AR \leq 17.5$ and a maximum $Re(h)$ of 700 and the experimental work of Naghib-Lahouti et al. (2012, 2014) for $AR = 12.5$ and $250 \leq Re(h) \leq 5 \times 10^4$, although the large differences in AR between these studies and the present investigation is emphasized. The visual inspection and spatial-correlation analysis of both the time-resolved and statistical stereo-PIV data have been used to reach this conclusion.

4.4 Low-Speed Zones of Streamwise Velocity

Both the upstream boundary layer and the wake region feature low-speed zones of streamwise velocity fluctuation. In the boundary layer they are often referred to as streaks due to their streamwise elongation, and they exist when the flow is turbulent or transitioning to turbulence. The boundary layer streaks are directly related to streamwise vortices near the wall (Blackwelder and Eckelmann, 1979; Schoppa and Hussain, 2002; Tomkins and Adrian, 2003), and the spanwise distance between adjacent low-speed streaks in a ZPG turbulent boundary layer ranges from 90 to 140 wall units depending on the distance from the wall (Smith and Metzler, 1983; Lin et al., 2008). As previously mentioned, low-speed zones of streamwise velocity also exist in the wake when secondary instabilities are present and the spanwise distance between adjacent low-speed zones matches the secondary instability wavelength (λ_z) in the wake (Mansy et al., 1994; Wu et al., 1996). The low-speed zones in the boundary layer and wake regions and their respective vorticity content will be investigated in this section. The spanwise distance between adjacent low-speed zones will be denoted as Λ_z.

Sample snapshots of the fluctuating component of streamwise velocity (u) are given in Figure 4.6 for $Re(h) = 3500$, 5200, and 7000 from the stitched 2C-PIV measurements within FOV2. The respective laminar, transitional, and turbulent nature of the upstream flow ($x < 0$) is evident within these snapshots. The fluctuation in streamwise velocity is almost non-existent in the upstream boundary layer in Figure 4.6a, as is expected for laminar flow. Conversely, the well-known turbulent boundary layer streaks are highly visible

in Figure 4.6*c*, where both low- and high-speed streaks can be seen to have a continuous presence. The transitional nature of the flow in Figure 4.6*b* is also evident, as boundary layer streaks are visible but do not populate the entire snapshot. Additionally, spanwise bands of low- and high-speed fluid are visible in the wake region ($x > 0$) of all snapshots. These bands represent slices through the primary spanwise vortices, resulting in low- and high-speed components which stem from the primary vortices that are rotating against and with the advecting frame of reference. The high-speed spanwise bands therefore represent primary vortices that have rolled off the near-side of the BTE ($y = 0$) and the low-speed spanwise bands represent primary vortices that have rolled off the far-side ($y = -h$). The undulation of streamwise velocity in the spanwise direction (within the bands) is visible in all three snapshots, although it is more pronounced in the spanwise bands that have $u < 0$. This is consistent with the snapshots presented in Figure 4.2, which revealed that the streamwise vortex pairs exist within the portion of each spanwise vortex that is rotating against advecting frame of reference (i.e. $u < 0$). This once again agrees with the cylinder mode B models that have been presented by Brede et al. (1996) and Williamson (1996b) and explains why the same undulating patterns are not visible in the spanwise bands with $u > 0$.

The spanwise distance between adjacent low-speed streaks in the upstream boundary layer was calculated using a spatial autocorrelation similar to the one described in Section 4.2 and presented in Equation 4.1. However, in the wake, the autocorrelation was only applied to the spanwise bands with $u < 0$ that hold the undulating patterns. These bands do not have a continuous presence in a single streamwise location, and so a window of streamwise width h (the height of the BTE) was used to search for the low-speed bands within each snapshot. The window was moved in the streamwise direction along the snapshots and the window with a minimum average velocity with respect to the rest of the snapshot was selected. The spanwise autocorrelation operation was applied to each window that was selected. The distance between adjacent low-speed zones was taken to be twice the distance between the initial maximum of the autocorrelation and the first minimum, and the centre

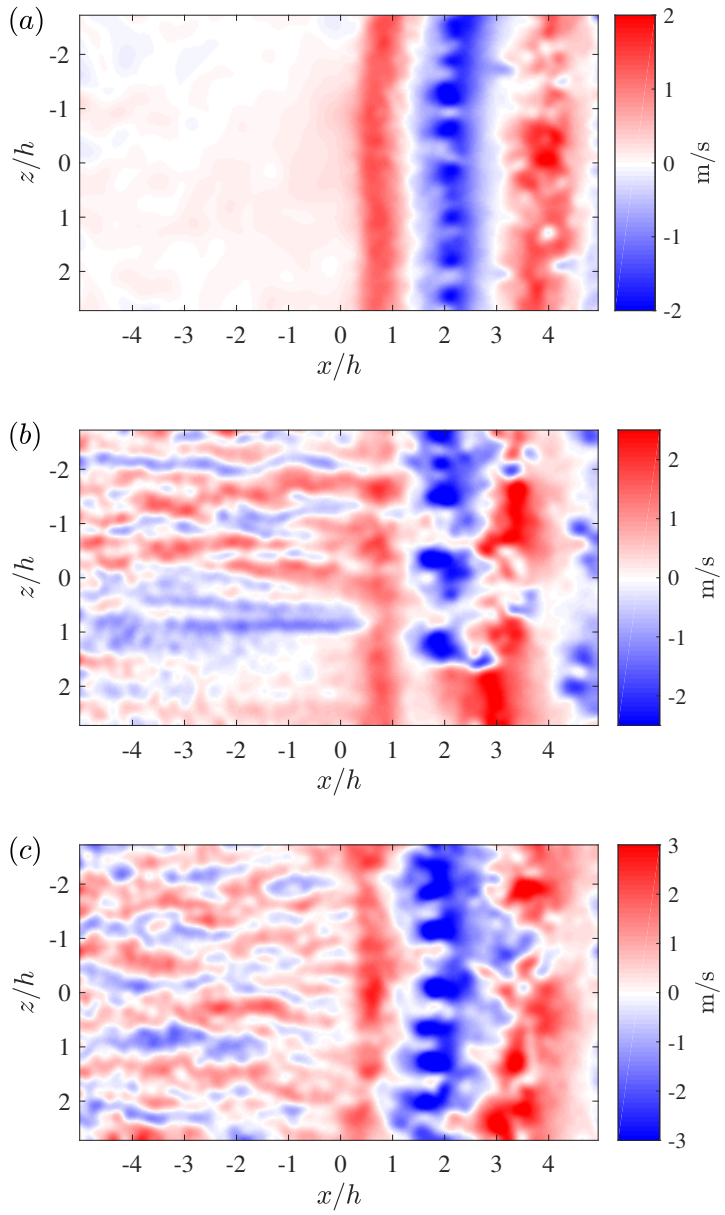

Figure 4.6: Instantaneous fluctuating component of streamwise velocity (u) in the x-z plane (y = 1.5 mm) for (a) $Re(h)$ = 3500, (b) $Re(h)$ = 5200, and (c) $Re(h)$ = 7000. The BTE is located at $x = 0$, and $x < 0$ represents the upstream boundary layer while $x > 0$ represents the wake. The respective laminar, transitional, and turbulent states of the upstream boundary layers are evident in the snapshots. The spanwise bands of positive and negative u in the wake represent the primary von Kármán vortices.

of the window was considered the streamwise location of each corresponding autocorrelation result. The results were then binned at varying streamwise locations. The estimated Λ_z in both the upstream boundary layer and wake have been fit with PDFs which are given in Figure 4.7 for $Re(h) = 3500$, 5200, and 7000 and at various streamwise locations before and after the BTE. The PDFs were estimated using a Burr type XII distribution (Tadikamalla, 1980).

Similarly to the PDFs of λ_z in Figure 4.3, all distributions of Λ_z in Figure 4.7 are unimodal and right-skewed. The peaks of the upstream boundary layer distributions (Figures 4.7*a-c*) are more distinct than those of the wake (Figures 4.7*d-f*), and it is generally observed that an increase in streamwise location brings a reduction in magnitude and shift of the peaks to the right. The most probable value for Λ_z in the upstream turbulent boundary layer at $Re(h) = 7000$ is approximately $0.41h$ based on the peaks of the PDFs at $x = -2h$ and $-h$ given in Figures 4.7*a* and 4.7*b*, respectively. Using the wall unit at $x = -7h$ presented in Table 4.1 for $Re(h) = 7000$ ($\lambda_0 = 44$ μm), this distance corresponds to $120\lambda_0$. This approximation falls within the expected range of 90-$140\lambda_0$ for a ZPG turbulent boundary layer (Smith and Metzler, 1983; Lin et al., 2008), despite the FPG in this boundary layer. Using Table 4.1 and the peaks in Figures 4.7*a* and 4.7*b*, the most probable value for Λ_z in the transitional boundary layer at $Re(h) = 5200$ is $81\lambda_0$.

The PDFs for Λ_z in the wake at $x = 2h$ (Figure 4.7*e*) are similar to the distributions for λ_z at the same location (Figure 4.3). The most probable values for these distributions are compared in Table 4.2, where it can be seen that the differences between λ_z and Λ_z at $Re(h) = 3500$, 5200, and 7000 are relatively small and correspond to -5.6%, 3.1%, and 8.0%, respectively, indicating that there is in fact a relationship between λ_z and Λ_z. The power spectral density (PSD) of u at $x = 2h$ has also been determined to further investigate Λ_z in the wake and to validate the results of the autocorrelations, as the latter may have filtered out wavelengths with lower energy content. The central spanwise rows of u have been extracted from the conditionally sampled spanwise bands of negative u (the same windows that were autocorrelated to create the PDFs in Figure 4.7*e*). The data

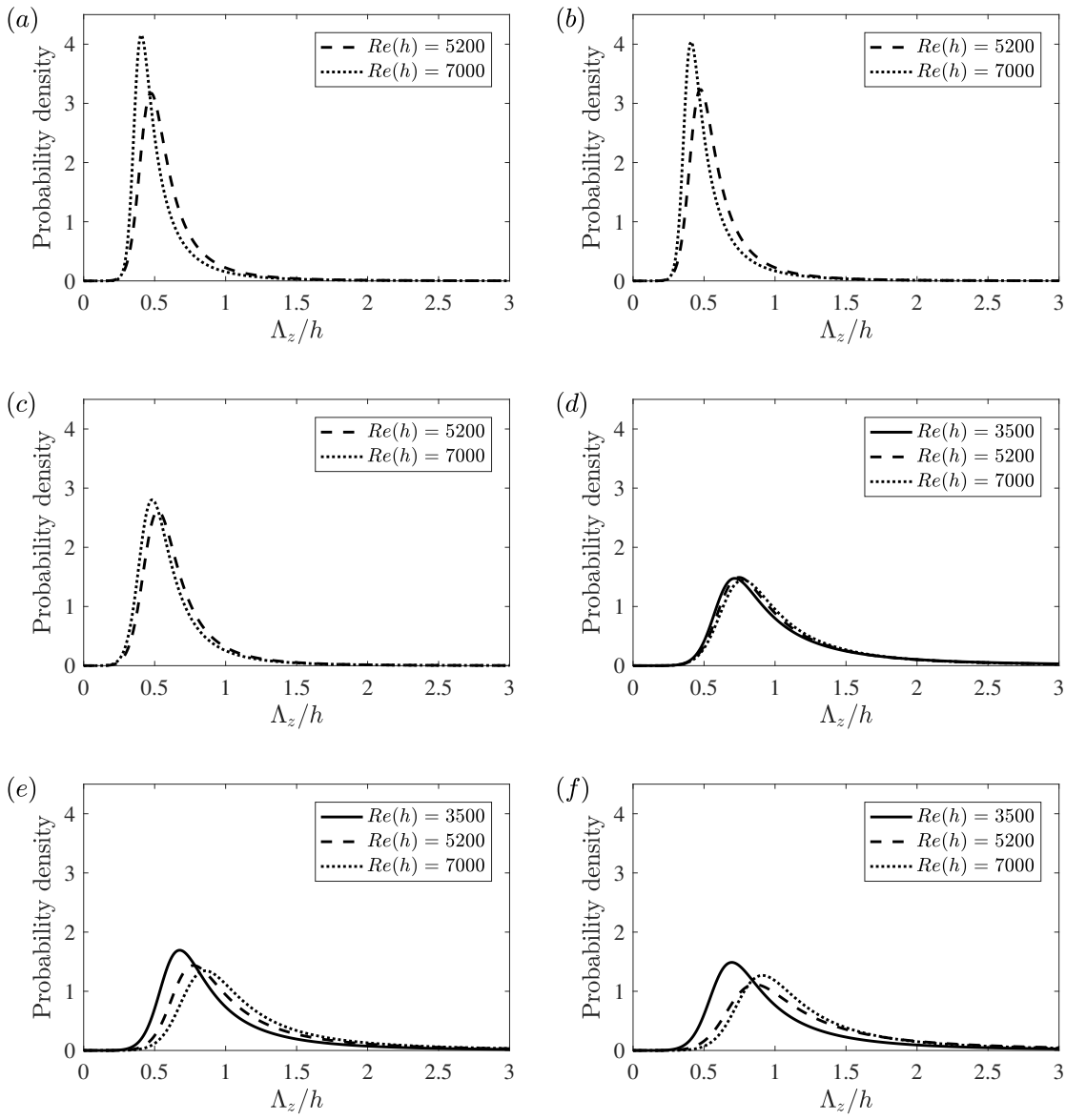

Figure 4.7: Probability density functions of the distance between adjacent low-speed zones (Λ_z) at $Re(h) = 3500$, 5200, and 7000 at streamwise locations (*a*) $x = -2h$, (*b*) $x = -h$, (*c*) $x = 0$, (*d*) $x = h$, (*e*) $x = 2h$, and (*f*) $x = 3h$. The peak of each distribution represents the most probable value for Λ_z at the corresponding streamwise location and Re.

$Re(h)$	λ_z	Λ_z
3500	$0.72h$	$0.68h$
5200	$0.75h$	$0.77h$
7000	$0.79h$	$0.86h$

Table 4.2: Most probable values for secondary instability wavelength (λ_z) and the spanwise distance between low-speed zones (Λ_z) in the wake at $x = 2h$ from the distributions given in Figures 4.3 and 4.7e, respectively.

were multiplied with a Hanning window before PSD was calculated using a fast Fourier transform. The resulting spectrums have been averaged and presented in Figure 4.8 as PSD versus normalized wavenumber (h/Λ_z). Each of the three spectrums features two peaks at the same locations for each Re. The first and second peaks correspond to $\Lambda_z = 5.4h$ and $1.1h$, respectively. The first value for Λ_z matches the total spanwise length of FOV2 and is therefore not physical. The second value of $\Lambda_z = 1.1h$ is close to the spanwise distances reported by the autocorrelations, thus validating the previous results. The absence of any other physical peak in the spectrums strengthens the observation that the cylinder mode B is the only secondary instability present in the wake of the elongated blunt body studied here.

The most probable values from all PDFs in Figure 4.7 are plotted as a function of distance from the BTE ($x = 0$) in Figure 4.9. This has been done to facilitate characterization of the evolution of the low-speed structures as they move from the upstream boundary layer and into the wake. Figure 4.9 reveals that the boundary layer streak spacing remains relatively constant before a rapid increase in Λ_z over the range $0 < x < h$ as the low-speed structures of the boundary layer are replaced by those of the unsteady wake. Beyond $x = h$, Λ_z stays relatively constant for $Re(h) = 3500$ and continues to gradually increase for $Re(h) = 5200$ and 7000.

As mentioned previously, the low-speed zones of streamwise velocity in both the upstream boundary layer and wake are related to the streamwise vorticity field. Whether the streamwise vortices present in the upstream boundary layer re-organize into the secondary wake vortices or are replaced altogether has been investigated using the stereo-PIV

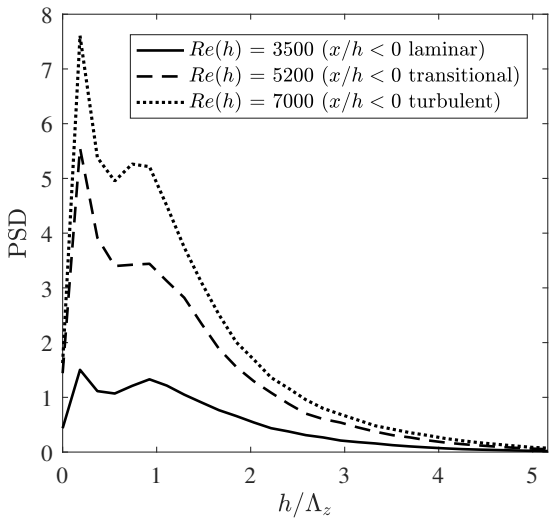

Figure 4.8: Power spectral densities of the spanwise signals of streamwise velocity fluctuation (u) in the wake at $x = 2h$ for $Re(h) = 3500$, 5200, and 7000. The first peak corresponds with the spanwise size of FOV2 and is therefore not physical. The second peak represents the secondary instability wavelength.

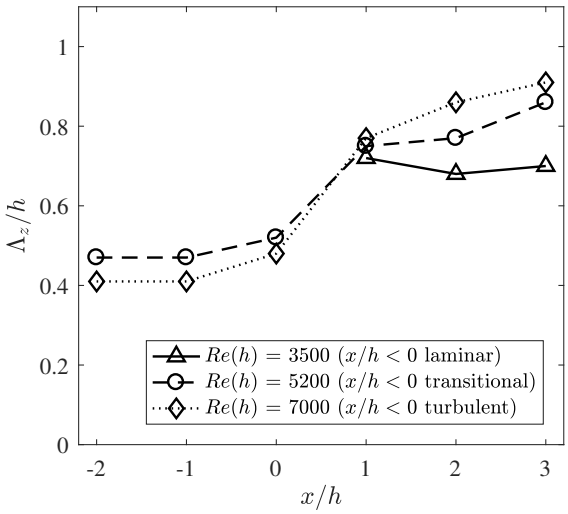

Figure 4.9: Most probable distance between adjacent low-speed zones (Λ_z) as a function of distance from the BTE ($x = 0$) for $Re(h) = 3500$, 5200, and 7000. Each point represents the peak of the corresponding probability density functions given in Figure 4.7. The rapid change in Λ_z over the region $0 < x/h < 1$ is due to the boundary layer structures being replaced by the secondary instability.

snapshots in the boundary layer at $x = -0.3h$ (FOV3) and the wake at $x = 2h$ (FOV4). Two-dimensional Q-criterion (Jeong and Hussain, 1995) has been used to identify vortices in the snapshots using a threshold to discard noise in the free-stream ($Q = 3000$ 1/s^2 was chosen by inspection of numerous snapshots of Q). The absolute values of streamwise vorticity ($|\omega_x|$) in the conditionally selected vortex cores with $Q > 3000$ 1/s^2 were summed and divided by the total area of the vortices to obtain a measure of average vorticity per unit vortex area within each snapshot. The results have been fit with PDFs using a Burr type XII distribution (Tadikamalla, 1980) and are displayed in Figure 4.10. The average vorticity content per unit area in the wake is nearly an order of magnitude higher than in the upstream boundary layer. This provides evidence to suggest that the mechanisms of streamwise vortex formation in the two flows are likely unrelated. This information, when coupled with the sharp increase in Λ_z over the range $0 < x < h$ observed in Figure 4.9 and the fact that the secondary instability does not change significantly as the upstream boundary layer transitions from laminar to turbulent, is evidence that the structures in the upstream transitional and turbulent boundary layers evolve into the near-wake flow without having much impact on the wake organization.

4.5 The Proper Orthogonal Decomposition of Streamwise Velocity in the Wake

Proper orthogonal decomposition (POD) is commonly used in turbulence studies to reduce flow fields to simplified representations (Berkooz et al., 1993). An ensemble is decomposed into time-varying amplitudes and a set of modes with decreasing energy content. The ensemble can be reconstructed using a select number of the modes to achieve a reduced-order representation of the data. The use of POD on snapshots of the fluctuating component of streamwise velocity (u) in the x-z plane of the wake is investigated in this section. This is done to study the energy content of the secondary instability in the wake and to carry out characterization of the secondary instability wavelength (λ_z) using the POD-based method applied by Naghib-Lahouti et al. (2012, 2014). This comparison is primarily motivated

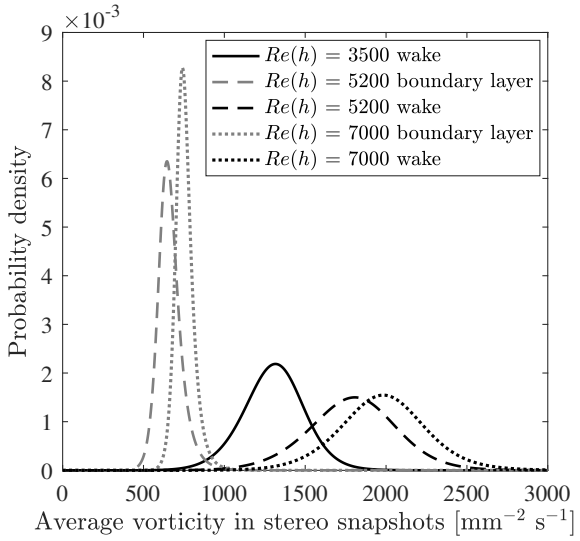

Figure 4.10: Probability density functions of average streamwise vorticity ($\langle\omega_x\rangle$) per unit area of the conditionally sampled vortex cores with $Q > 3000$ 1/s^2 in the boundary layer at $x = -0.3h$ and wake at $x = 2h$ for $Re(h) = 3500$, 5200, and 7000. A change in vortex strength of nearly an order of magnitude is visible between the boundary layer and wake.

by the differences in the wake structures reported between these studies and the present investigation, as it is not clear if the differences are physical or an artifact of the analysis techniques used. The present investigation has determined λ_z by direct measurement of the secondary vortices; however, Naghib-Lahouti et al. (2012, 2014) relied on measurements of u in the streamwise-spanwise plane and therefore the measurements of λ_z were indirect.

The POD of u by the method of snapshots (Section 2.5) has been performed on the 5000 snapshots within FOV2 ($x > 0$ only, i.e. just the wake) for $Re(h) = 3500$, 5200, and 7000. The first 8 POD modes and their energy content are given in Figures 4.11 and 4.12, respectively. The first two POD modes for each Re capture the dynamics of the primary instability, and modes 3 and 4 capture its large-scale distortion. These first 4 POD modes contain large fractions of the energy in the flow with respect to the remaining modes as shown in Figure 4.12. It is not clear if modes 5-8 are related to the distortion of the primary instability or the spanwise modulation of the secondary instability if λ_z is not known *a priori*. Figure 4.12 also reveals that the energy captured within the initial POD

modes shifts to the higher modes as Re increases. As it is expected, it becomes increasingly difficult to capture the complete dynamics of the flow using only a few modes when the levels of turbulence increase. Additionally, the first 8 POD modes presented here are in agreement with those given by Naghib-Lahouti et al. (2014), and 6 of the modes for each Re are practically identical between studies.

The snapshots of u have been reconstructed using varying numbers of modes and the same autocorrelation analysis used in Section 4.4 to determine the distance between adjacent low-speed zones (Λ_z) in the wake has been performed on the reduced-order ensembles. This was done to investigate the impact that the POD of u has on the PDFs of Λ_z. The effect of using 16, 24, 32, and 48 modes to reconstruct the snapshots of u was investigated. These four cases cover the analyses of Naghib-Lahouti et al. (2012, 2014), which used either 32 POD modes or enough modes to retain at least 70% of the energy in the flow. This energy criterion was met by using 16-32 modes depending on Re in the latter case. Figure 4.13 displays the impact of these reconstructions on the PDFs of Λ_z in the wake at $x = 2h$ for $Re(h) = 3500$, 5200, and 7000. Note that a kernel technique was necessary for estimating the PDFs once the distributions became multimodal (Sheather, 2004).

The PDFs in Figure 4.13 show that the distributions of Λ_z are highly sensitive to how many modes are used to reconstruct the snapshots. Using fewer modes causes the peak of each distribution to decrease in magnitude and shift to the right, thus erroneously increasing the estimated values for λ_z. When 24 modes are used for reconstruction, the PDFs become multimodal with the first peak bearing some resemblance to the expected peak for λ_z. The peaks following the first one likely represent the wavelengths present in some of the more energetic modes, for example modes 3 and 6 for any Re in Figure 4.11. When 16 modes are used for reconstruction, the presence of the first distinct peak that represents λ_z is no longer dominant, suggesting that the majority of information regarding the secondary instability is stored beyond mode 16.

It is evident that the application of POD to streamwise-spanwise snapshots of u when determining λ_z is highly dependent on the number of POD modes used to reconstruct

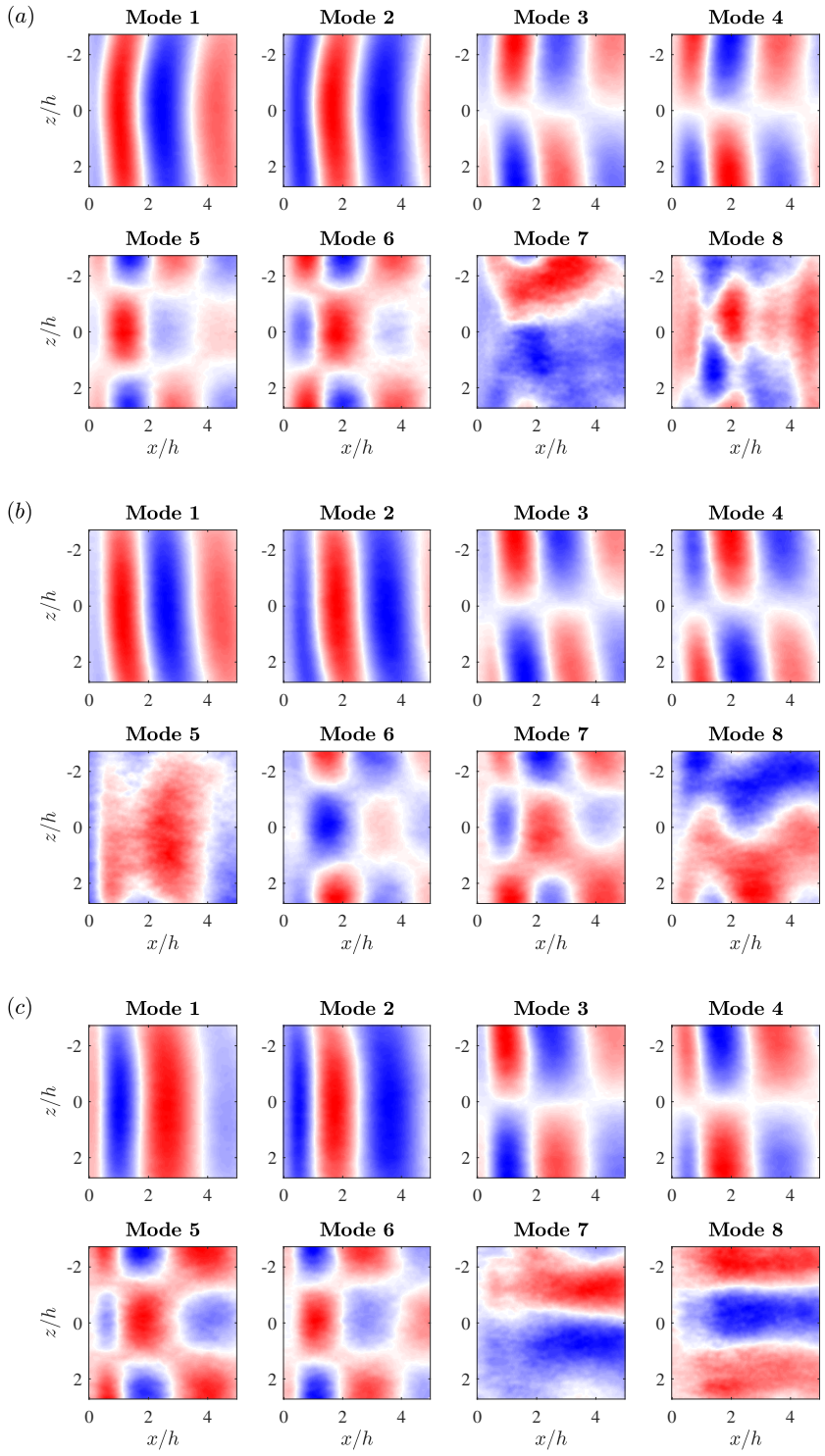

Figure 4.11: The first 8 POD modes of the fluctuating component of streamwise velocity (u) in the wake at $y = 1.5$ mm for (a) $Re(h) = 3500$, (b) $Re(h) = 5200$, and (c) $Re(h) = 7000$. The secondary instability wavelength is not visible in any of the modes.

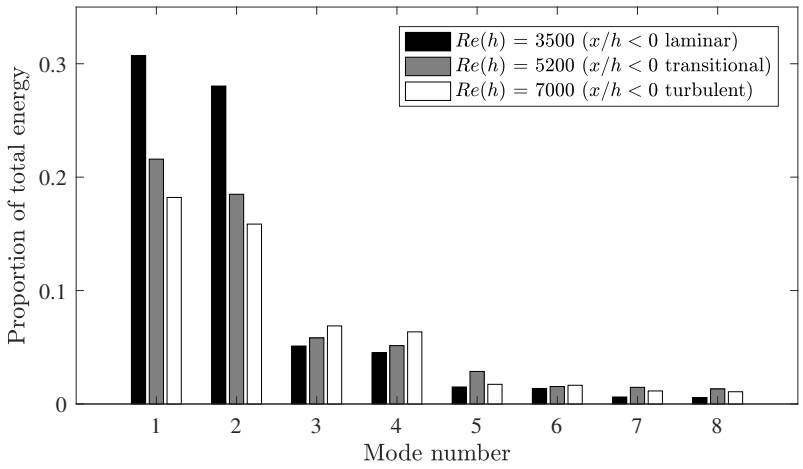

Figure 4.12: Energy associated with each of the POD modes given in Figure 4.11. A shift in energy to the higher modes occurs as Re is increased, indicating higher levels of turbulence.

the data ensembles and must be carefully applied. For example, when using 48 modes to reconstruct u and thus preserving at least 70% of the energy in the flow as was done by Naghib-Lahouti et al. (2014), the mean values for Λ_z in the wake are $2.24h$, $2.21h$, and $2.26h$ for $Re(h) = 3500$, 5200, and 7000, respectively. These values nearly exactly match λ_z for the mode B$'$ instability predicted by Ryan et al. (2005) and fall within the range of mean values reported by Naghib-Lahouti et al. (2012, 2014). When the original snapshots are used (100% energy), the mean values are $1.01h$, $1.21h$, and $1.29h$, respectively, and are consistent with the direct measurements of the secondary vortices in the present study. There are large differences in AR between these studies and the present investigation, and so this does not dismiss the presence of mode B$'$ for small AR; however, a re-evaluation of the wavelength of the secondary instability and the formation of mode B$'$ for elongated blunt bodies with AR smaller than what is considered here ($AR = 46.5$) is suggested.

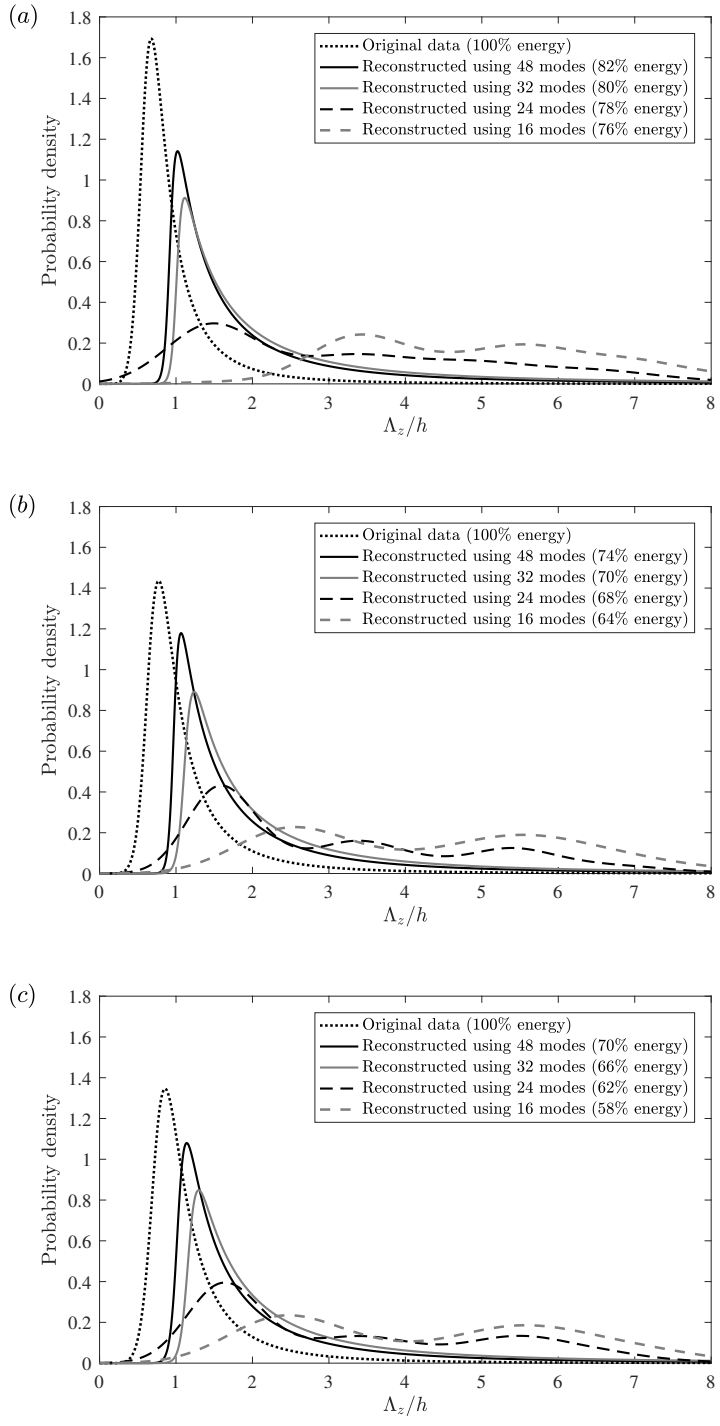

Figure 4.13: Effect of number of modes used in POD reconstruction on the probability density functions of the distances between low-speed zones (Λ_z) in the wake at $x = 2h$ for (a) $Re(h) = 3500$, (b) $Re(h) = 5200$, and (c) $Re(h) = 7000$. The distributions were calculated using the same spatial autocorrelation that is covered in Section 4.4. The distributions are highly sensitive to the number of POD modes used in reconstruction of the data.

Chapter 5

Active Wake Control Using Piezoelectric Actuators

This chapter focuses on the active control of vortex shedding from the modified blunt trailing edge (BTE) following Experiment 2 (Section 3.4). First, the surface-pressure signals are used to examine the full operating range of the actuators. Proper orthogonal decomposition (POD) is then applied to sets of particle image velocimetry (PIV) data for selected actuation cases to investigate how actuation affects the primary wake instability. Instances of vortex shedding amplification, suppression, and re-organization are studied. Finally, an adaptive slope-seeking control algorithm is applied to optimize actuation frequency in real time.

5.1 Actuation Envelopes

The suppression variable (σ) presented in Equation 3.1 is used here to evaluate the performance of the actuators over their entire operating range for symmetric, asymmetric, and single actuation. The actuator driving frequencies (f_a) have been varied from 10 to 180 Hz in increments of 10 Hz and the amplitudes have been varied from 2 to 30 V in increments of 2 V, resulting in 270 data points for each method. Each value of σ has been determined using 10 s of microphone data, corresponding to roughly 500 unforced wake cycles. The results have been formed into the contour plots in Figure 5.1, where the upper horizontal axis displays actuation frequencies normalized by the unforced wake frequency (f_u) and the orange band represents a region where σ cannot be evaluated (see Section 3.4.4). It is first

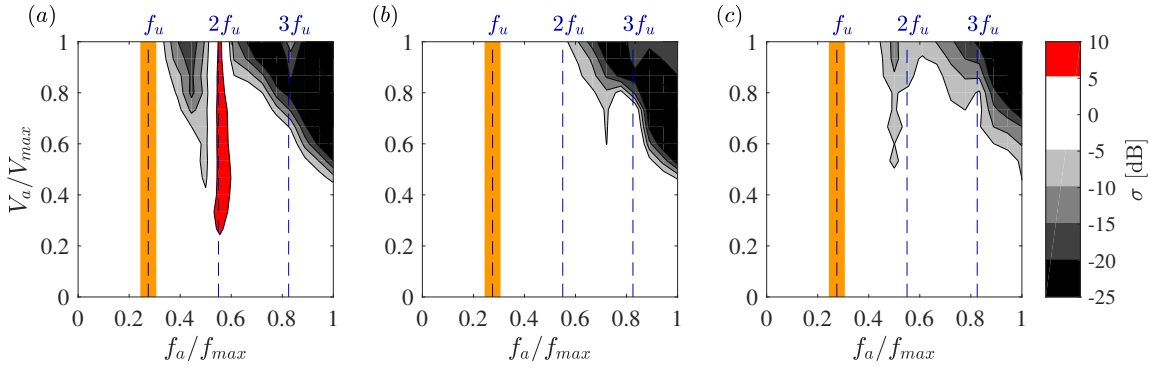

Figure 5.1: Contour plots of the suppression variable (σ, see Equation 3.1) over the entire operating envelope for (a) symmetric, (b) asymmetric, and (c) single actuation. The orange band centered at f_u represents an area of no data, as σ cannot be evaluated at the unforced wake frequency. All three contour plots indicate large amounts of vortex shedding suppression at high actuation amplitudes and frequencies. Note that $V_{max} = 30$ V and $f_{max} = 180$ Hz.

interesting to note that all three actuation methods appear to be able to suppress vortex shedding in the wake at high actuation amplitudes and frequencies as is evident in the upper right corners of the plots. This suggests that there is a form of threshold phenomenon at play, and this threshold appears to be above $f_a = 2f_u$ for all cases. As well, symmetric actuation (Figure 5.1a) results in behaviour that is not present for asymmetric and single actuation. This includes vortex shedding amplification at $f_a = 2f_u$ and a second region of vortex shedding suppression that occurs within $1 < f_a/f_u < 2$.

These contour plots have led to the selection of 6 cases of interest for each actuation method. These are actuation at 1.0, 1.5, 2.0, 2.5, 3.0, and 3.5 times the unforced wake frequency at the maximum actuation amplitude for all three actuation methods, thus covering all potential regions of vortex shedding suppression and amplification. High-speed PIV of the wake following Section 3.4.2 has been conducted within FOV5 for all cases of interest as well as for the unforced wake. These data ensembles will be the focus of the analysis for the next three sections.

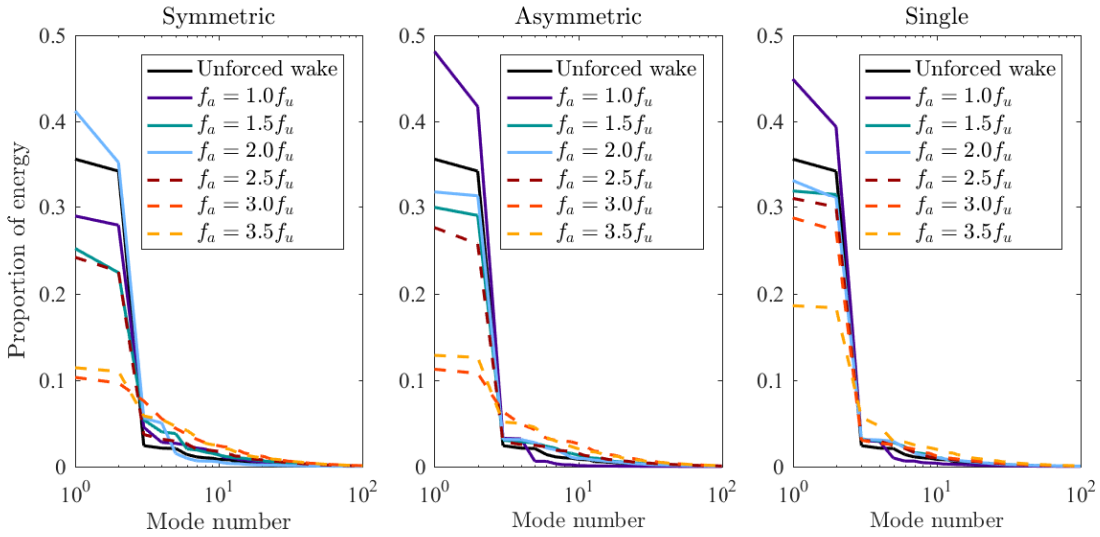

Figure 5.2: Total energy captured by each of the first 100 POD modes for all actuation cases as well as the unforced wake. Cases of vortex shedding suppression and amplification are evident for all three actuation methods.

5.2 Analysis of Wake Energy

The POD of streamwise velocity by the method of snapshots (Section 2.5) has been applied to all PIV data ensembles. This has been done to study the interaction between actuation and the primary instability. With respect to a periodic wake, it is known that the first two POD modes represent the dynamics of two-dimensional vortex shedding and contain a large fraction of the fluctuation energy in the wake flow (van Oudheusden et al., 2005). These two modes are used here to monitor the coherence of the vortex shedding pattern during actuation.

The energies associated with the first 100 POD modes for all cases are plotted in Figure 5.2. The energy contained within the first two modes of the unforced wake represents approximately 70% of the wake fluctuation energy, and the third mode contains only 2.4%. This demonstrates that the unforced wake is dominated by the primary vortex shedding instability. Considering the first two POD modes for the actuated cases, there are clear instances of both vortex shedding amplification and suppression for all three actuation methods. Moreover, the energy contained beyond mode 10 is negligible for all cases. To

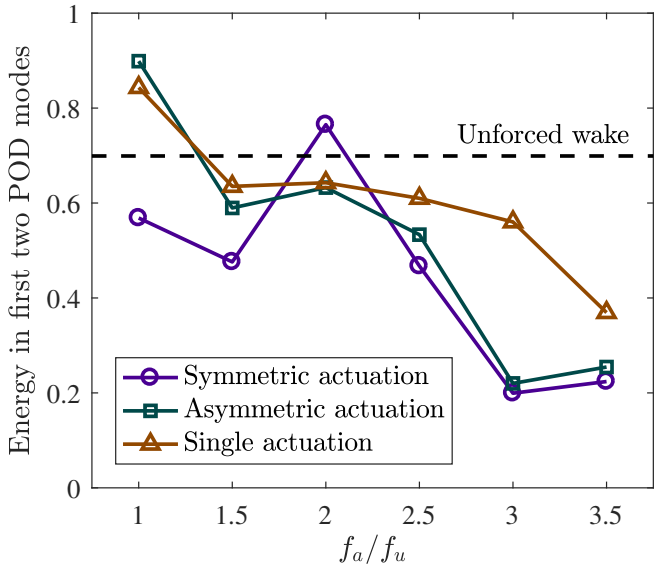

Figure 5.3: Energy content within the first two POD modes for all actuation cases considered here. Maximum vortex shedding suppression occurs at $f_a = 3f_u$ for symmetric and asymmetric actuation and at $f_a = 3.5f_u$ for single actuation. Cases of vortex shedding amplification are visible at $f_a = f_u$ and $2f_u$, likely through resonant forcing.

facilitate visualization of the trends, the total energy captured by the first two POD modes is plotted in Figure 5.3 as a function of actuation frequency. It should first be noted that the trends in Figure 5.3 agree with those determined using the microphone signals (Figure 5.1). Specifically, significant vortex shedding suppression occurs beyond $f_a = 2f_u$ for all cases, and symmetric actuation leads to amplification at $f_a = 2f_u$ and a second suppression region located in the range $1 < f_a/f_u < 2$. Two more cases of vortex shedding amplification are visible, corresponding to asymmetric and single actuation at $f_a = f_u$ (the region in Figure 5.1 where σ could not be evaluated), and this is likely due to synchronization between the actuation cycles and the primary instability. The most effective vortex shedding amplification occurs during asymmetric actuation at $f_a = f_u$, resulting in a vortex shedding pattern that contains 90% of the fluctuation energy in the flow. Conversely, symmetric actuation at $f_a = 3f_u$ leads to the maximum suppression of the vortex shedding pattern, resulting in the first two POD modes containing only 20% of the fluctuation energy. These cases and others will be evaluated further in the following sections.

5.3 Vortex Shedding Amplification

Two primary instances of vortex shedding amplification will be considered here: symmetric actuation at $f_a = 2f_u$ and asymmetric actuation at $f_a = f_u$. These two cases result in an increase in the energy associated with two-dimensional vortex shedding by 7% and 20%, respectively, according to the POD analysis presented in Figure 5.3. Amplification by single actuation at $f_a = f_u$ seems to be a weakened version of the amplification caused by asymmetric actuation and is therefore not considered.

As previously mentioned, vortex shedding amplification generally leads to an increase in turbulence intensities in the wake and a decrease in base pressure. The latter is related to formation length, i.e. the size of the mean recirculation region (Williamson, 1996a). These items are investigated within Figure 5.4, where contours of mean streamwise velocity ($\langle U \rangle$), turbulence intensities ($\langle u^2 \rangle$, $\langle v^2 \rangle$), and instantaneous snapshots of vorticity (ω_z) are given. Note that the recirculation region is defined by $\langle U \rangle = 0$ and is therefore represented by the black region in the plot.

The mean contours of streamwise velocity presented in Figure 5.4*a* show a widening of the wake and a shortening of the recirculation region for both actuation cases. Interestingly, symmetric amplification results in the shortest recirculation region, even though asymmetric amplification appears to be more effective at enhancing vortex shedding in the wake. The shortened recirculation regions suggest a decrease in base pressure because the low-pressure cores of the shed vortices are closer to the base of the BTE. This also suggests an increase in drag for both cases. The mean turbulent fluctuations in the streamwise and transverse directions are investigated in Figures 5.4*b*, *c*. Both cases of vortex shedding amplification result in higher levels of turbulent fluctuations on average, with asymmetric amplification producing the largest increases. Specifically, the maximum turbulent intensity in the transverse direction doubles under asymmetric amplification, and this can be seen in Figure 5.4*c*. This is indicative of large velocity fluctuations in the direction normal to the freestream flow and is likely followed by an increase in fluctuating forces acting on the body. Finally, the instantaneous snapshots of vorticity presented in Figure 5.4*d* reveal that the

amplified wakes lead to a more organized von Kármán pattern general. This is especially the case for asymmetric amplification, which results in shed vortices that are more round and coherent compared to those of the unforced wake. These results are consistent with those of Benard and Moreau (2013), who found that vortex shedding amplification resulted in more organized shedding and a shortened recirculation region. The authors also found that the vortices shed closer to the trailing edge of the body, and this seems to be the case in the present investigation as well as is evident from the reduced recirculation regions.

The improved coherence of the shed vortices has been further investigated statistically using the results of the POD analysis. This is done using phase plots of the normalized POD coefficients from the first two modes (van Oudheusden et al., 2005). The ideal case of two-dimensional vortex shedding will produce a phase plot corresponding to the unit circle. Any deviations from the circle can be considered to be due to turbulent fluctuations and differences between the various shedding cycles, i.e. larger deviations are caused by inconsistent vortex shedding. The POD mode amplitudes $a_i(t)$ for the first two modes have been normalized by the corresponding eigenvalues λ_i and are plotted against each other in Figure 5.5. The plots reveal that both instances of vortex shedding amplification result in more coherent vortex shedding; however, the effect is significantly more pronounced under asymmetric amplification. The lack of deviation from the tightly grouped phase circle in Figure 5.5*b* is evidence of vortex lock-on during asymmetric actuation, which acts to force the organization of the wake. The same evidence is not present for symmetric actuation, as the phase plot shows deviation even beyond that of the unforced wake for a short period of time. These results are in agreement with the instantaneous vorticity plots in Figure 5.4*d*, which show improved vortex shedding coherence, especially in the case of asymmetric amplification. Note that the contours of the suppression variable in Figure 5.1 and the energy trends of the first two POD modes in Figure 5.3 suggest that vortex shedding amplification is only possible within a narrow frequency range around $2f_u$ for symmetric actuation and f_u for asymmetric and single actuation.

Further inspection of the high-speed PIV data reveals that the mechanism behind vortex

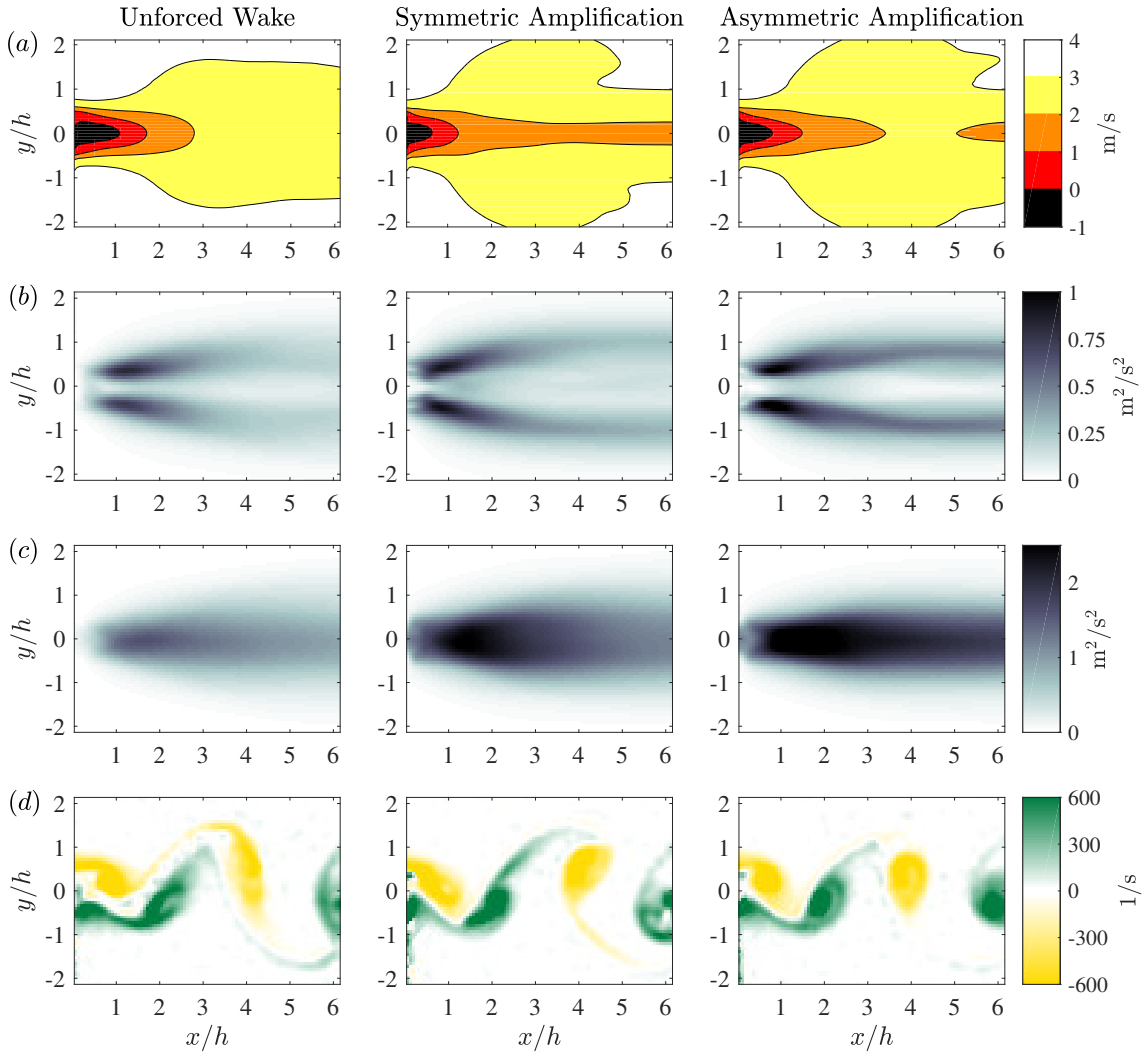

Figure 5.4: (a) Mean streamwise velocity contours $\langle U \rangle$, (b) streamwise turbulence intensities $\langle u^2 \rangle$, (c) transverse turbulence intensities $\langle v^2 \rangle$, and (d) instantaneous snapshots of vorticity ω_z for the unforced and amplified wakes. Vortex shedding amplification generally leads to a shorter recirculation region, larger turbulence intensities, and more organized vortex shedding.

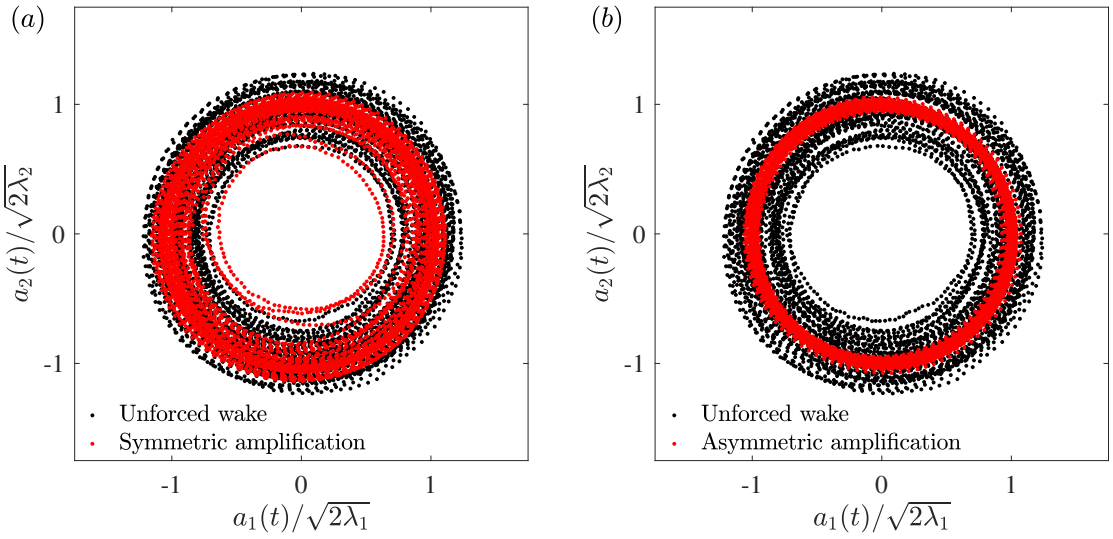

Figure 5.5: Phase plots of the first two POD mode amplitudes ($a_i(t)$) normalized by the corresponding eigenvalues (λ_i) and compared to those of the unforced flow for (a) symmetric and (b) asymmetric amplification. A normalized phase plot that more closely resembles the unit circle is indicative of more coherent vortex shedding.

shedding amplification through asymmetric actuation is in fact synchronization between the natural wake tendencies and the actuation cycles. A schematic representation of this mechanism is presented in Figure 5.6. As the shear layer on one side of the BTE rolls into the near-wake, the piezoelectric flaps move towards that shear layer. This initiates the roll-up of the forming vortex, effectively increasing its strength until it is shed from the body. As the shear layer from the opposite corner of the BTE begins to roll into the wake, the piezoelectric flap changes directions and the cycle of vortex enhancement continues. The asymmetric motion of the piezoelectric flaps simulates transverse oscillations of a flexible trailing edge in a localized manner. This actuation is similar to the transverse oscillation of a cylinder in that regard, which can also lead to vortex shedding enhancement through synchronization (Tao et al., 1996; Warui and Fujisawa, 1996). It should be noted that amplification through single actuation assists the forming vortex using only one piezoelectric flap, explaining why the amplification is not as strong. Vortex shedding amplification by symmetric actuation is also similar, but one piezoelectric flap is working against the vortex

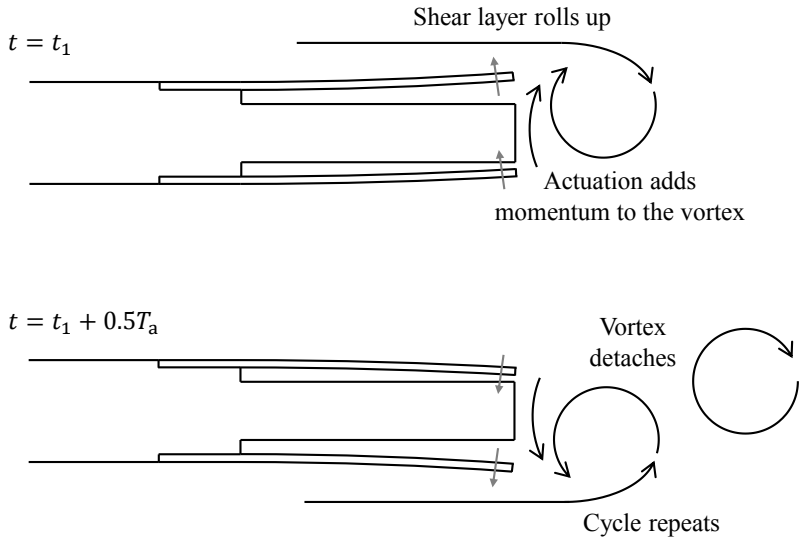

Figure 5.6: Schematic representation of the vortex shedding amplification mechanism under asymmetric actuation. T_a is the period of actuation.

strengthening process. This is likely the reason why symmetric actuation results in the weakest amplification of the wake unsteadiness.

5.4 Vortex Shedding Suppression

Suppression of the unsteady wake has been studied using the best performing actuation frequencies according to Figure 5.3 for all three actuation methods. This corresponds to symmetric and asymmetric actuation at $f_a = 3f_u$ and single actuation at $f_a = 3.5f_u$, resulting in the first two POD modes containing 20%, 22%, and 37% of the total fluctuation energy, respectively. Recall that this value is 70% for the unforced wake. Similarly to vortex shedding amplification, the performance of the suppression methods is first evaluated using the contours of mean streamwise velocity, turbulence intensities, and instantaneous snapshots of vorticity presented in Figure 5.7. Note that the unforced wake plots from Figure 5.4 will be used as the reference for evaluation of the suppression cases.

In contrast to vortex shedding amplification, the mean velocity contours in Figure 5.7*a* reveal a drastic narrowing of the wake and moderate lengthening of the recirculation region

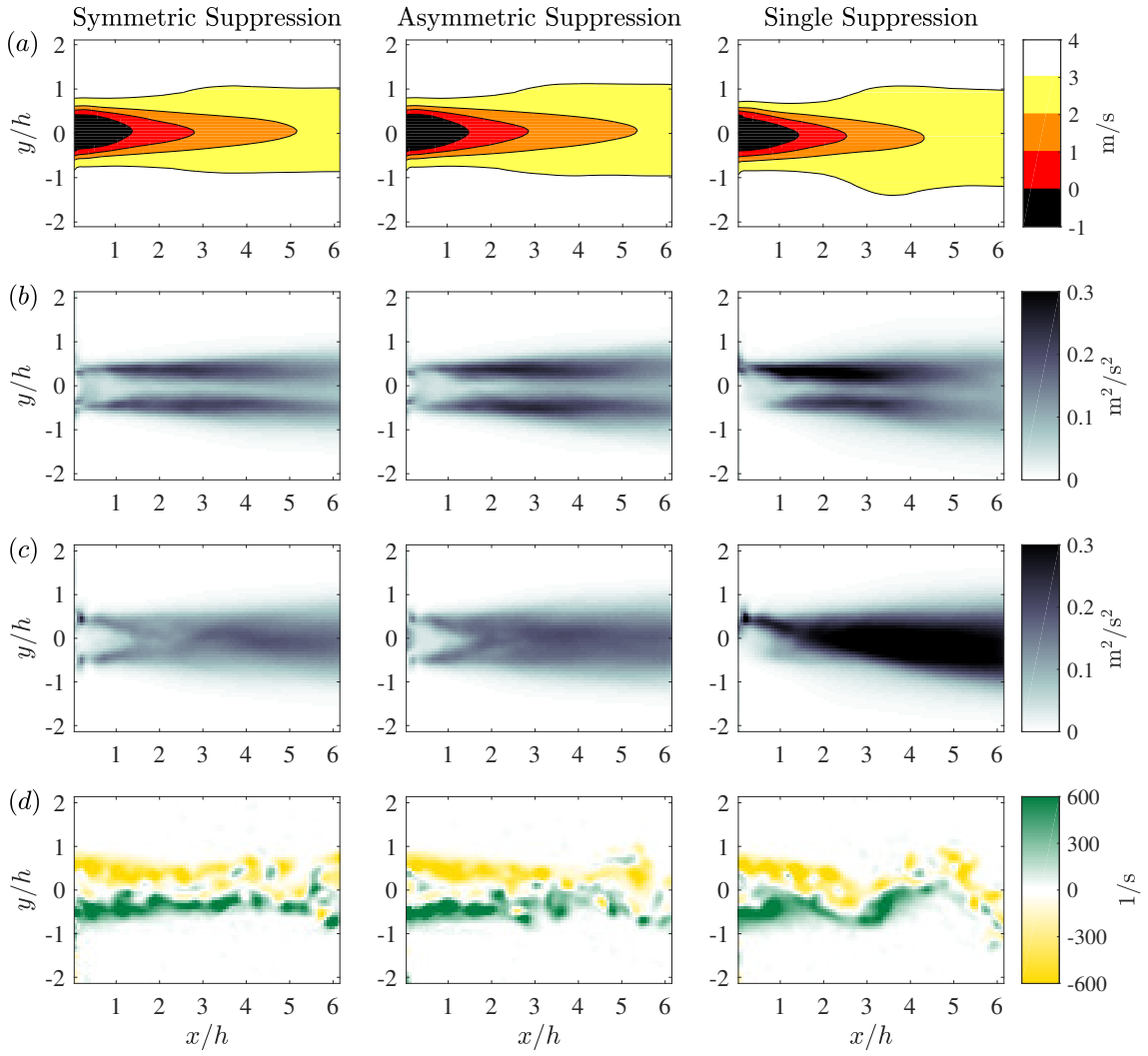

Figure 5.7: (a) Mean streamwise velocity contours $\langle U \rangle$, (b) streamwise turbulence intensities $\langle u^2 \rangle$, (c) transverse turbulence intensities $\langle v^2 \rangle$, and (d) instantaneous snapshots of vorticity ω_z for the symmetric, asymmetric, and single actuation suppression cases. Vortex shedding suppression is accompanied by an elongated recirculation region, greatly reduced turbulence intensities, and the removal of the vortex shedding pattern.

when vortex shedding suppression is successful. This suggests an increase in base pressure and therefore a decrease in bluff body drag. The patterns of turbulent fluctuations have been elongated, and the magnitudes have been greatly reduced (note that that axis scales in Figures 5.7b, c are significantly reduced when compared to the unforced wake reference in Figure 5.4b, c). Symmetric and asymmetric actuation show similar results; however, single actuation leads to less turbulence reduction and an asymmetric wake pattern. This is surely due to the fact that only one piezoelectric flap is influencing the wake. The turbulent fluctuations begin just past the tip of the piezoelectric flap before they increase and expand downstream, although they still do not reach the levels of turbulence that are present in the unforced wake.

The instantaneous vorticity plots in Figure 5.7d reveal a complete removal of the unsteady wake pattern for symmetric and asymmetric actuation, and a large reduction in the pattern for single actuation. Further inspection of these plots and the high-speed PIV data reveal that the separating shear layers become populated with small concentrations of vorticity. Spanwise vortices form at the tip of the piezoelectric flaps when the flap moves away from the wake centre line as shown schematically in Figure 5.8. The flap protruding into the high-shear flow forces this roll-up locally. The result is the formation of small spanwise vortices at the frequency of actuation. These vortices disrupt the natural interaction between the separating shear layers, thus resulting in suppression of the primary instability. Similar results have been obtained by Fujisawa et al. (2004), who found that suppression of the wake occurs when a slot synthetic jet caused the formation of small spanwise vortices directly into one of the shear layers separating from a circular cylinder. Nati et al. (2013) also reported vortex shedding suppression via shear layer disruption, but using plasma actuators near a BTE that acted to break up the shear layers in a less organized manner.

Snapshots of vorticity presented in Figure 5.7d reveal complete suppression of vortex shedding at an instant in time, but the question remains as to whether the suppression is continuous in time. This has been investigated using the frequency content in the wake. If the vortex shedding pattern is still present, the natural wake frequency should be present

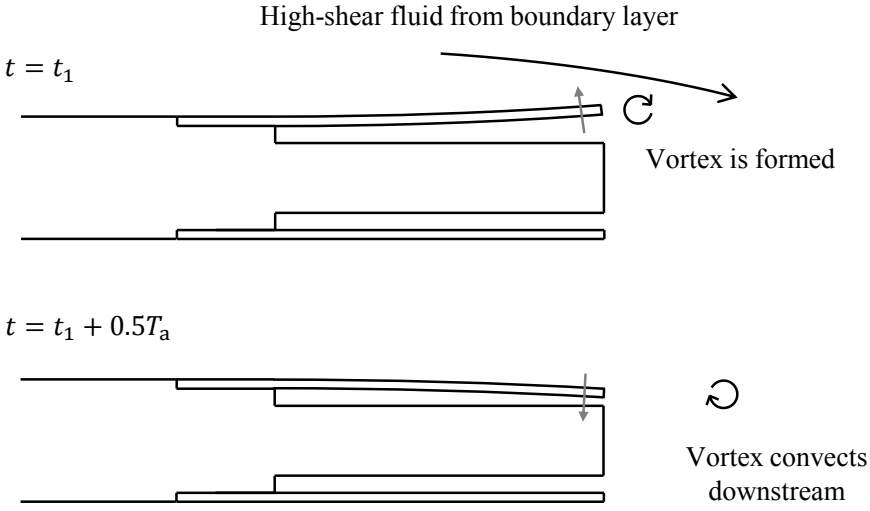

Figure 5.8: Schematic representation of the vortex shedding suppression mechanism. T_a is the period of actuation.

to some degree as well. The fluctuating component of streamwise velocity (u) from the time-resolved PIV data has been used to calculate the power spectral density (PSD) of velocity in the wake as a function of distance from the BTE, and the results are shown in Figure 5.9. Note that asymmetric actuation has been omitted from this analysis because the present results indicate that there is a negligible difference between symmetric and asymmetric suppression. As expected, the PSDs contain a significant peak corresponding to the natural vortex shedding frequency when the wake is unforced. This peak is maximized at the location $x = 3h$, and there is a small frequency component present at $f = 2f_u$ that likely represents a harmonic of the natural wake. Looking at symmetric actuation in Figure 5.9a, it is evident that the maximum suppression case ($f_a = 3f_u$) completely removes the peak corresponding to the unforced vortex shedding frequency up to at least $x = 6h$ downstream. Actuation at $f_a = 2.5f_u$ greatly reduces the magnitude of the peak, but some influence of the primary instability remains, and it increases with downstream distance. Single actuation, shown in Figure 5.9b, is not able to completely suppress the frequency component corresponding to vortex shedding, but suppression increases significantly when

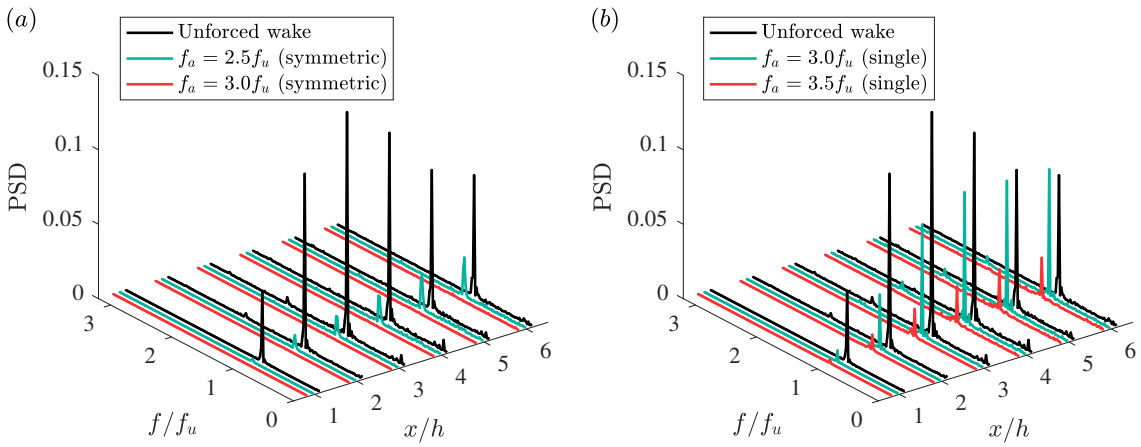

Figure 5.9: Power spectral density (PSD) of the fluctuating component of streamwise velocity (u) as a function of distance from the BTE (evaluated at $y = h$) for the unforced wake and for (a) symmetric and (b) single actuation cases. Complete removal of the vortex shedding frequency occurs as far as $x = 6h$ downstream during symmetric actuation at $f_a = 3f_u$.

the actuation frequency is increased from $f_a = 3f_u$ to $3.5f_u$. This is evidence that single actuation at a higher frequency than what is investigated here may result in complete suppression of the unsteady wake, suggesting that disruption of one shear layer may be sufficient for complete removal of vortex shedding. It should also be noted that, although vortex shedding is suppressed as far as $6h$ from the BTE, the primary instability and therefore wake unsteadiness has the potential to resume further downstream. This may be sufficient in the context of wake control, as delaying the vortex shedding process to further downstream has been shown to reduce the negative effects acting on a BTE (Pastoor et al., 2008).

5.5 Symmetric Wake Re-Organization

The second suppression region in the range $1 \leq f_a/f_u \leq 2$ visible in Figures 5.1 and 5.3 has not yet been addressed. This region is peculiar because it occurs only for symmetric actuation and for a narrow range of frequencies. It has been further studied using the high-speed PIV data corresponding to symmetric actuation at $f_a = 1.5f_u$. Contours of mean

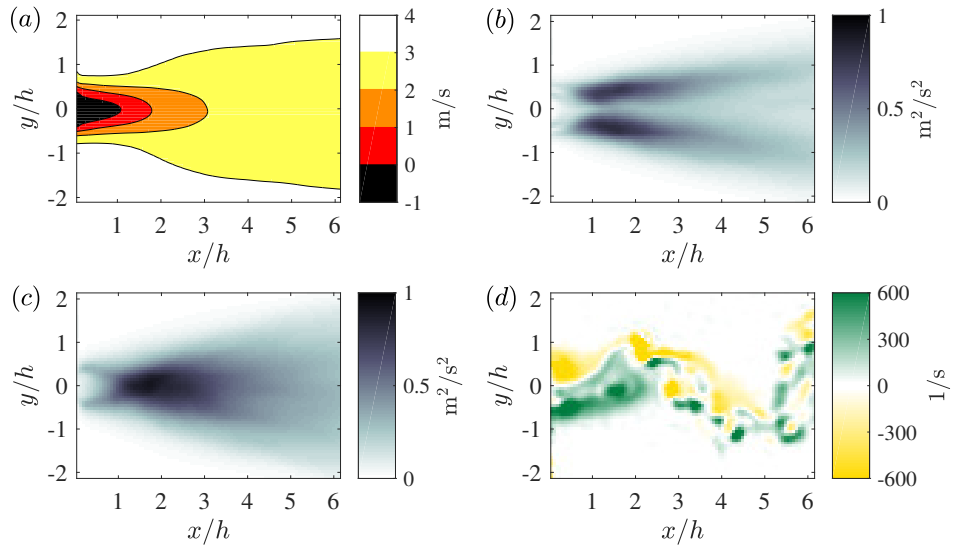

Figure 5.10: (a) Mean streamwise velocity contours $\langle U \rangle$, (b) streamwise turbulence intensities $\langle u^2 \rangle$, (c) transverse turbulence intensities $\langle v^2 \rangle$, and (d) instantaneous snapshots of vorticity ω_z for symmetric actuation at $f_a = 1.5 f_u$. The forced symmetric near-wake causes the overall shape of the wake to resemble a V, and the vortex shedding pattern can be seen to resume downstream.

streamwise velocity, turbulence intensities, and instantaneous snapshots of vorticity are presented in Figure 5.10, and the unforced wake plots from Figure 5.4 will once again be used as the reference for evaluation. The figure reveals that the mean recirculation region is not significantly affected, but the overall shape of the wake changes to resemble a V. This is also true for the turbulence intensities, which are slightly higher on average when compared to the unforced wake. Most notably, the vorticity plot reveals that the instantaneous structure of the wake is different when compared to the previously studied cases. First, the shear layers appear to be rolling up at the BTE simultaneously, suggesting that the symmetric wake mode is being forced in the near-wake by the symmetric actuation. Second, the overall structure of the alternating vortex shedding pattern appears to be present further downstream from the BTE, but without the presence of large, coherent spanwise vortices. It appears that the symmetric mode is forced, but the natural wake tendencies begin to dominate almost immediately.

The temporal evolution of the symmetric near-wake vortices has been plotted in Figure

5.11 to qualitatively investigate the behaviour of the wake during symmetric actuation at $f_a = 1.5f_u$. Three separate time sequences are shown, each of which follows the initially symmetric wake vortices using a red dashed box. The time instances are labelled by $t_i + \Delta t$, and all three sequences ($i = 1, 2, 3$) reveal similar behaviour. First, the symmetric vortices form from the separating shear layers (t_i) and grow in size as they move downstream ($t_i + 8$ ms). The symmetry of the two vortices then breaks ($t_i + 16$ ms) before they decompose into much smaller concentrations of vorticity ($t_i + 24$ ms). The small concentrations of vorticity continue to exist as they convect downstream with behaviour that resembles vortex shedding. The growth, symmetry breaking, and decomposition of the vortices occurs at distances of approximately h, $2h$, and $3h$ from the BTE, respectively. The formation of symmetric but unstable vortices during wake actuation has also been reported by Nishihara et al. (2005), Konstantinidis and Balabani (2007), and Pastoor et al. (2008).

Further inspection of the high-speed PIV data reveals that the symmetric wake is forced in the same way that the small spanwise vortices are generated during vortex shedding suppression (Figure 5.8), i.e. the vortices form from the shear layers when the piezoelectric flaps move away from the wake centre line. The primary difference is that the actuation frequency applied here is much closer to the natural frequency of the wake. The vortices grow and interact instead of simply remaining embedded in the shear layers, and this is likely because the primary wake instability has more influence at this frequency.

The complex interaction between the symmetric near-wake and the downstream vortex shedding is investigated using Figure 5.12, which shows PSD as a function of distance from the BTE for symmetric actuation at $f_a = 1.5f_u$. The plot reveals a clear shift in the dominant wake frequency to a value of approximately $0.75f_u$. This frequency is almost non existent in the very near-wake ($x = h$) and grows in strength with downstream distance. A small frequency component is also visible at $x = h$ corresponding to $1.5f_u$. This peak does not seem to be caused by a harmonic because it is the same magnitude as the only other peak at that streamwise location. Instead, it is likely due to the cyclic formation of the symmetric vortices caused by actuation, and its contribution to PSD is negligible at

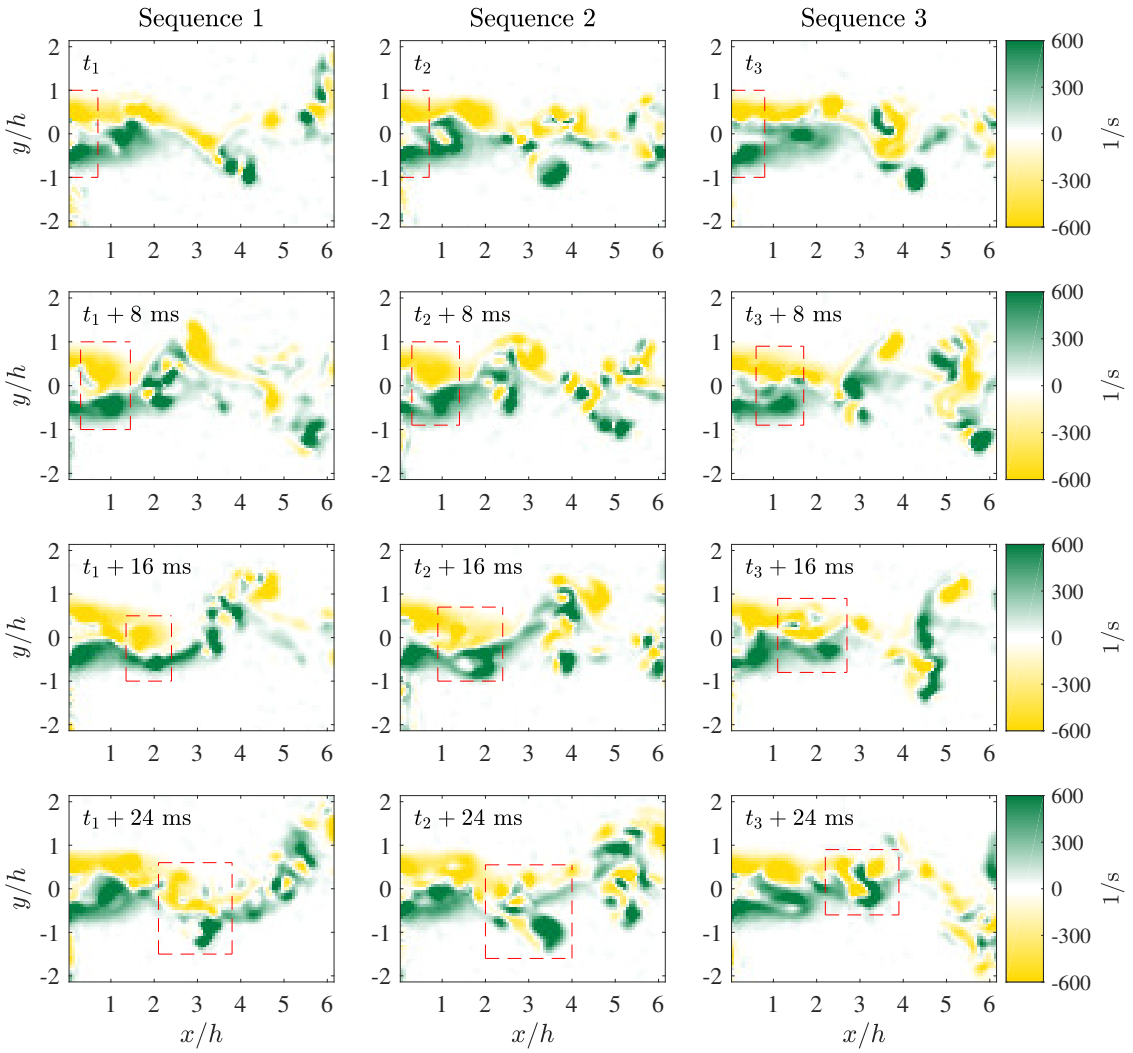

Figure 5.11: Temporal evolution of the symmetric vortical structures as they evolve into the wake region for symmetric actuation at $f_a = 1.5 f_u$. Three separate time sequences are shown. The four time frames for each sequence reveal that the symmetric vortices form in the near-wake, grow as they move downstream, destabilize, and then decompose into small concentration of vorticity.

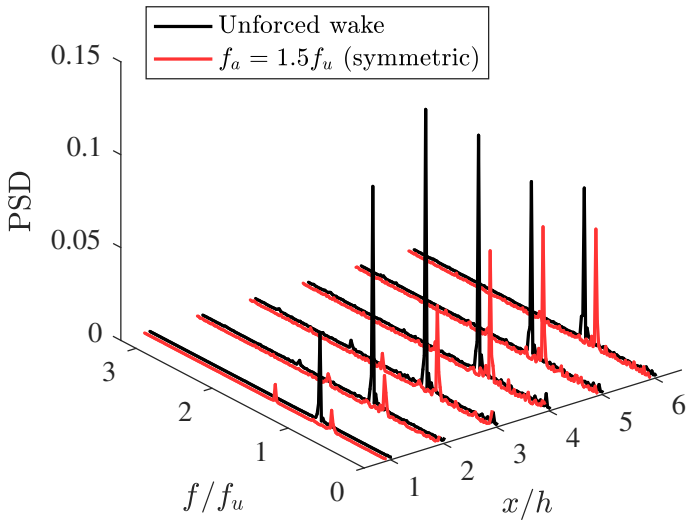

Figure 5.12: Power spectral density (PSD) of the fluctuating component of streamwise velocity (u) as a function of distance from the BTE (evaluated at $y = h$) for the unforced wake and for symmetric actuation at $f_a = 1.5f_u$. The dominant wake frequency shifts to a value of $0.75f_u$ during actuation.

all downstream points. This suggests that the wake is still dominated by the downstream vortex shedding, despite it being delayed by the forced symmetry in the near-wake.

5.6 Application of Adaptive Slope-Seeking Control

The present actuation strategies allow for effective manipulation of the wake structures to achieve both amplification and suppression of vortex shedding from a BTE. However, they were effective due to careful selection of the actuation parameters using analyses that are not easily applied outside of a laboratory environment. The utilization of adaptive slope-seeking allows for a system to automatically seek optimal control inputs in real time if a measurement of the plant to be controlled is available (Ariyur and Krstić, 2003). This method of closed-loop control is applied here to seek optimal actuation inputs for vortex shedding suppression using the microphone measurements at the BTE.

The microphone signals were investigated in Section 5.1 using the suppression variable, but this is not possible in real time due to the difficulties associated with calculating PSD

at high rates. Instead, a band-pass filter is applied to the measurements of P' to isolate the vortex shedding signal while attenuating the acoustic noise generated by the piezoelectric flaps, thus allowing for monitoring of the vortex shedding pattern in real time. An implication of this is that actuation cannot be applied at frequencies within the pass band of the filter. This is acceptable for vortex shedding suppression in the present context because it has been shown that the current actuation methods suppress the wake at actuation frequencies that are more than twice that of the unforced wake. The band-pass-filtered microphone signal will be denoted as P'', and the root-mean-square (rms) of P'' is used to obtain a measure of the magnitude of the wake fluctuations. The control goal is then to minimize P''_{rms} using the actuation frequency of the piezoelectric flaps.

A significant advantage of closed-loop control is the ability to adapt to changes and reject disturbances. In the context of the present investigation, this refers to changes or disturbances in freestream velocity, which would lead to a variation in the unforced wake frequency. A small range of Reynolds numbers (Re) is considered here to allow for testing of the ability of the controller to reject disturbances. This range corresponds to $2600 \leq Re(h) \leq 3500$ and 49.5 Hz $\leq f_u \leq$ 68.7 Hz. The lower and upper cutoff frequencies of the band-pass filter have therefore been chosen to be 45 and 75 Hz to allow for the monitoring of vortex shedding using P'' within this range.

Symmetric actuation at the maximum amplitude has been selected for closed-loop control because it results in the most effective suppression while having the smallest chance of imposing unnecessary fluctuating forces on the BTE. The actuation parameter that will be optimized using slope-seeking is the frequency of actuation f_a. The steady-state maps of P''_{rms} are given as a function of f_a/f_u for $Re(h) = 2600$ and 3500 in Figure 5.13, where each data point has been determined by calculating P''_{rms} over a 20 s period. Note that this is not practical for real-time application, and so P''_{rms} is calculated using the last 0.1 s of microphone data during real-time control. The range of frequencies shown in the plot were selected because they represent a steep slope that the controller can navigate to find the optimal input. Upon inspection, the steady-state map is of the plateau type and will

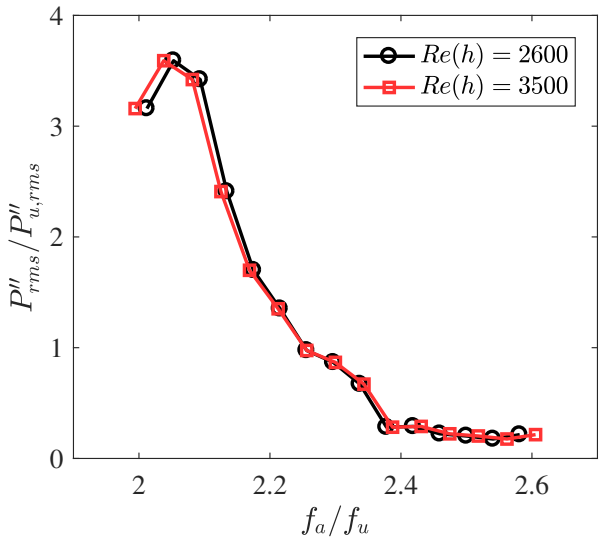

Figure 5.13: The plateau-style steady state maps for the current application of adaptive slope-seeking. The optimal actuation frequency according to these maps is $f_a/f_u = 2.4$, and the map appears static within $2600 \leq Re(h) \leq 3500$.

therefore require seeking a small non-zero slope. The curves for both Re have the same shape, and the optimal actuation input according to the maps is approximately $f_a/f_u = 2.4$ (the initiation of the plateau). It is interesting to note that this disagrees with the previous POD analysis, which suggested that $f_a/f_u = 3$ provides maximum suppression (Figure 5.3). This discrepancy has been caused by the fact that the microphones are only capable of measuring the near-wake, while POD was applied to PIV data extending as far as 6 BTE thicknesses downstream and therefore could account for delayed wake unsteadiness. This is evident in Figure 5.9 where it can be seen that symmetric actuation at $f_a/f_u = 2.5$ was able to suppress vortex shedding in the near-wake, but it ultimately resumed downstream. This reduced observability of the wake is simply a result of using flush-mounted sensors embedded into the BTE as opposed to sensors that can measure the downstream state of the wake to a greater extent. Despite this, actuation at $f_a/f_u = 2.4$ will be considered optimal for the current application of adaptive slope-seeking.

The control loop structure used here is presented in Figure 5.14 and is based off the work of Brackston et al. (2016). The major modification that the authors implement to the

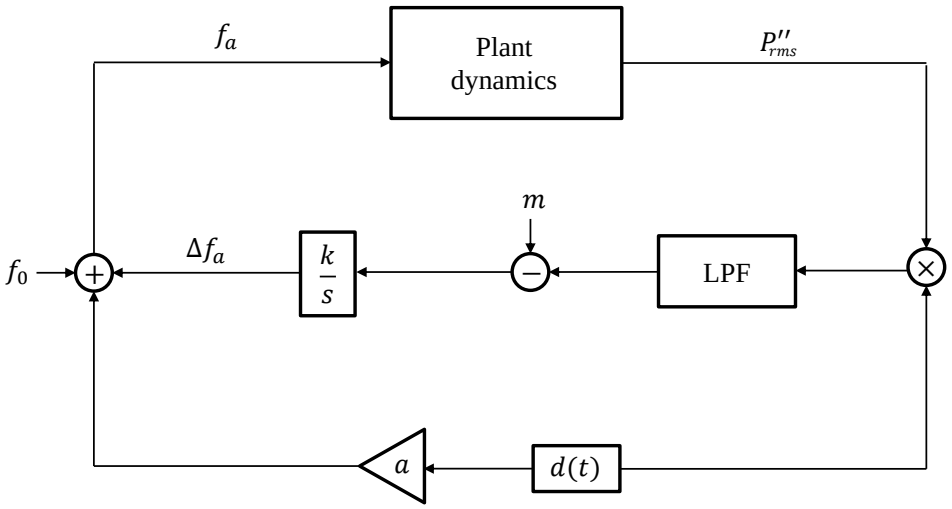

Figure 5.14: The control loop structure implemented for adaptive slope-seeking. Following Brackston et al. (2016), the low-pass filter (LPF) is a moving average filter with a period of $2\pi/\omega_d$ and the dither signal $d(t)$ is a unit square wave with a frequency of ω_d.

standard slope-seeking loop is the removal of the high-pass filter, which, as they explain, becomes redundant with a properly designed low-pass filter. Specifically, a moving-average filter with a period of $2\pi/\omega_d$ is selected, where $\omega_d = 2\pi f_d$ is the frequency of the dither signal in radians. This filter results in complete attenuation of the harmonics of ω_d, which are what are what remain unaccounted for in the signal if the high-pass filter is removed. A second modification to the standard control loop is the use of a square wave dither signal as opposed to a sinusoid. This change is made because the input to the system is the frequency of actuation. The result would be an actuator driving frequency that is itself changing in a sinusoidal manner, resulting in unwanted broadband frequency content (Brackston et al., 2016). Thus, the square wave dither is used here, and the control input is only updated when the square wave changes from 1 to -1 or vice versa. The signal driving the actuators is therefore a sinusoid of constant amplitude whose frequency changes in a stepwise manner.

The adaptive slope-seeking controller requires selection of the dither frequency (f_d), dither amplitude (a), slope reference (m), and integrator gain (k) for use in the control loop structure presented in Figure 5.14. These values were tuned experimentally, resulting

in $f_d = 0.2$ Hz, $a = 2$, $m = -0.008$, and $k = -22$, and were selected to obtain quick and stable system performance without overshoot. The system response at $Re(h) = 2600$ under these parameters can be viewed in Figure 5.15. The plot reveals large fluctuations in P''_{rms} prior to the controller being turned on. These fluctuations occur at the frequency of the dither signal and their magnitude is indicative of the steep slope on the steady-state map. The controller acts to force these fluctuations to a small value once it is turned on. After approximately 30 s, the controller settles at the optimal frequency $f_a/f_u = 2.4$ and maintains this value over time. This system response time ($\sim$30 s) is large compared to the time scale of the unsteady wake dynamics ($\sim$0.02 s). This is a consequence of using an adaptive slope-seeking controller, which requires such differences in time scales to operate properly (Brackston et al., 2016). Figure 5.15 reveals that there are still small oscillations in P''_{rms} at the dither frequency after reaching $f_a/f_u = 2.4$. This occurs because a small slope is used as the reference. If a slope of zero were to be sought then the controller would act to remove all oscillations in the signal because it is the oscillations that provide a measure of the slope.

The ability of the controller to respond to disturbances has been investigated by changing the freestream velocity in the wind tunnel once the controller has settled at the optimal value. The disturbance was simulated by increasing, holding, then decreasing the wind tunnel velocity while staying within the Re range that the controller was designed for ($2600 \leq Re(h) \leq 3500$). The Strouhal number of the unsteady wake flow remains constant at $St(h) = 0.20$ within this range, and so it has been used to determine f_u as the freestream velocity changes. This allows for monitoring f_a/f_u as long as the freestream velocity is known. The freestream velocity in the wind tunnel was recorded using a simple planar PIV measurement at an acquisition frequency of 25 Hz during the disturbance rejection experiment. The results of the experiment are presented in Figure 5.16. It can be seen that, after an adaptation period, the controller is able to reject the disturbance and reach the optimal actuation frequency of $f_a/f_u = 2.4$ at the new freestream velocity. The same is true when the Re is reduced back to its original value. However, the controller responds

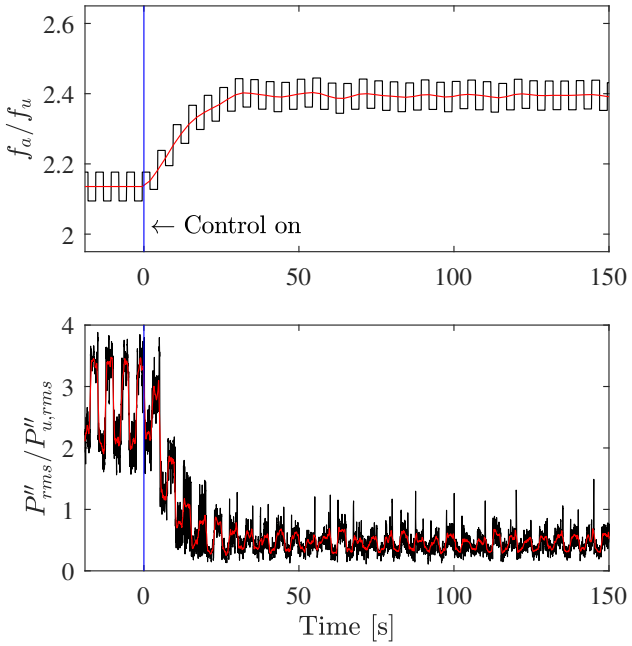

Figure 5.15: System response of the adaptive slope-seeking controller at $Re(h) = 2600$. The controller seeks the optimal input of $f_a/f_u = 2.4$ in approximately 30 s, and maintains this value over time.

more quickly when the freestream velocity is increased as opposed to decreased. This is due to the fact that a slope measurement is driving the control action using an integrator. The error in the slope is larger when the velocity is increased because the current position on the steady-state map (Figure 5.13) is moved up the steep slope. When the velocity is decreased, the current position is moved further down the plateau. The difference between the reference m and the zero slope of the plateau does not offer as much of a driving force for the controller and therefore the adaptation is slower. This also means that if the reference was set to zero for this particular plateau-style map, the controller would not be able to reject a reduction in the freestream velocity because the difference between the reference and the current slope would remain zero when the current position on the steady-state map was shifted up the plateau.

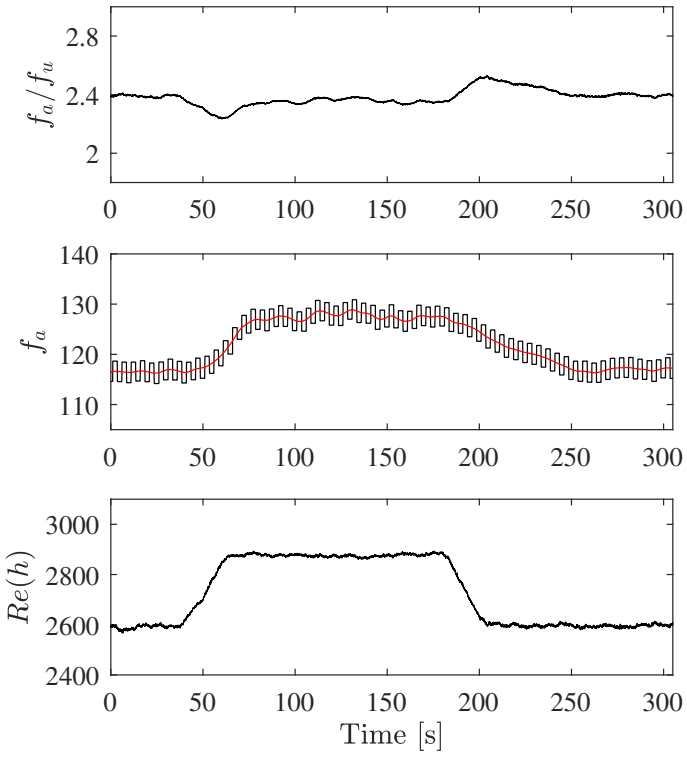

Figure 5.16: System response to a simulated disturbance in the form of a varying freestream velocity. The slope-seeking controller is able to reject the change in freestream velocity and eventually return to the optimal input of $f_a/f_u = 2.4$. The controller is quicker to adapt to increases in freestream velocity because of the nature of the plateau-style steady state map.

Chapter 6

Conclusions

Vortex shedding affects many geometries found within industrial systems, and the blunt trailing edge (BTE) investigated here is one of these systems. Flow past the blunted feature causes an unsteady vortex pattern to dominate the wake, resulting in unwanted pressure forces on the body. This thesis has advanced the understanding of the phenomenon and developed a means for controlling it. The complex vortex structures in the natural unsteady wake have been experimentally studied, and an active control strategy has been designed and successfully implemented. This chapter presents a summary of the primary results and outlines recommendations for future work.

6.1 Secondary Instabilities

The present experimental investigation utilized various particle image velocimetry (PIV) measurements to characterize the secondary instability in the wake of an elongated blunt body with an aspect ratio (AR) of 46.5 at Reynolds numbers (Re) of 3500, 5200, and 7000, and investigated its relationship with low-speed streamwise velocity patterns in both the upstream boundary layer and wake region. The wake was found to be populated with streamwise counter-rotating vortex pairs that are typical of bluff body wake flows. The most probable spanwise distance between adjacent vortex pairs in the wake at $x = 2h$ was found to range from 0.7-0.8h depending on Re. The streamwise vortices maintained both their rotational directions and spanwise positions during primary vortex shedding

cycles. Furthermore, the secondary vortices appeared to be simply connected between cycles and were shown to wrap around the primary spanwise vortex cores while passing through the portion of each primary vortex that is rotating against the advecting frame of reference. The characteristics of the secondary instability did not change greatly as the upstream boundary layer transitioned from laminar to turbulent. Only a slight increase in the secondary instability wavelength was observed, along with an expected increase in wake turbulence.

The characteristics of the secondary instability described above match those of the cylinder mode B and all features agree with the mode B models that have been proposed by Brede et al. (1996) and Williamson (1996b) for the wakes of circular cylinders. The present results do not suggest extrapolation of the stability analysis of Ryan et al. (2005) to higher Re and AR as is evident in the summary given by Table 6.1. Their analysis predicted that elongated blunt body wakes with $AR > 7.5$ would be afflicted by modes that differ from those of circular cylinders at Re smaller than 700. No evidence of their predicted modes B$'$ nor S$'$ has been found in the present study, although it should be emphasized that the present investigation was performed on an elongated blunt body with larger Re and AR than what Ryan et al. (2005) considered in their stability analysis.

The present investigation also shows different results compared with the works of Naghib-Lahouti et al. (2012, 2014). They concluded the presence of mode B$'$ with secondary instability wavelengths ranging from 2.0 to 2.5h in the wake of an elongated blunt body with a much smaller AR of 12.5 for $250 \leq Re(h) \leq 5 \times 10^4$ as shown by Table 6.1. The same indirect characterization of the secondary instability applied in these studies using proper orthogonal decomposition (POD) was repeated here. It was shown that the use of POD for characterizing the secondary instability in the wake is highly sensitive to the amount of energy captured (number of modes used) by the data reconstruction. This may also explain the large differences between the model proposed by Naghib-Lahouti et al. (2012) and the models of Brede et al. (1996) and Williamson (1996b), as the former was influenced by the indirect POD-based analysis. Further investigation of the secondary instability by direct

	$Re(h)$ range	Aspect ratio(s)	Dominant mode(s)	Wavelength(s)
Present investigation	3500-7000	46.5	B	0.7-0.8h
Naghib-Lahouti et al. (2014)	2000-50000	12.5	B′	2.3-2.5h
Naghib-Lahouti et al. (2012)	250-2150	12.5	B′	2.0-2.5h
Ryan et al. (2005)	Up to 700	2.5-17.5	B′, S′	2.2h, 0.7-1.0h

Table 6.1: Summary of the present and past investigations regarding secondary instabilities in the wake of a BTE.

characterization of the vortical structures in the wake of elongated bodies with small AR is suggested.

Finally, the present investigation showed that the average strength of the streamwise vortices in the upstream boundary layer was nearly an order of magnitude less than the average strength of the streamwise vortices in the wake. It was also shown that the boundary layer streaks are quickly replaced by the wake structures over the region $0 < x < h$. These observations, when coupled with the fact that the state of the upstream boundary layer does not significantly affect the secondary instability in the wake, suggest that the upstream boundary layer structures are simply absorbed into the near-wake region without having much of an impact on the wake organization. This also implies that the state of the upstream boundary layer does not play much of a role in the development of the secondary instability. This result is congruent with the findings of Naghib-Lahouti et al. (2014), who concluded that the secondary instability has little dependence on the state of the upstream boundary layer.

6.2 Active Control

The manipulation of vortex shedding from a BTE using oscillating piezoelectric flaps with sub-millimeter displacement has been studied experimentally in a wind tunnel at $Re(h) = 2600$. The actuators were operated to a maximum frequency of 180 Hz, and microphones installed at the surface of the trailing edge allowed for measuring the pressure fluctuations in the near-wake. The surface-pressure measurements were used to investigate the impact of actuation over the entire operating range of the actuators for three different actuation methods: symmetric, asymmetric, and single actuation. The results indicated that all three

methods were capable suppressing the dominant vortex shedding frequency in the wake at high actuation frequencies and amplitudes.

The surface-pressure results were used to select actuation cases of interest and high-speed PIV was conducted to further investigate the wake flow. The cases of interest were selected to cover all possible instances of vortex shedding amplification and suppression. POD was applied to the resulting vector fields to study the energy content in the wake that is attributable to the primary vortex shedding instability. This value was 70% in the unforced wake, and it was obtained by summing the energy captured by the first two POD modes which represent the dynamics of the two-dimensional vortex shedding pattern.

Asymmetric actuation at $f_a = f_u$ lead to the maximum amplification of the wake. The energy captured by the first two POD modes increased to 90%, and the vortex shedding became more coherent and organized. The mean recirculation region in the wake shortened, suggesting a reduction in base pressure, and the turbulence intensities increased significantly. The high-speed data revealed that amplification was caused by synchronization between the natural wake tendencies and the actuation cycles, which enhanced the forming vortices prior to their detachment from the BTE. The asymmetric flapping of the trailing edge was similar to a transversely oscillating cylinder, which can also lead to vortex shedding amplification (Tao et al., 1996; Warui and Fujisawa, 1996). Symmetric and single actuation were able to amplify vortex shedding to some degree, but their impact was less pronounced because one of the piezoelectric flaps was either turned off or working against the enhancement for these cases.

Maximum vortex shedding suppression occurred during symmetric and asymmetric actuation at $f_a = 3f_u$, which lead to the first two POD modes containing only 20% and 22% of the total fluctuation energy, respectively. Although symmetric actuation seems to slightly out-perform asymmetric actuation, there did not seem to be a significant difference between their performances. Suppression resulted in a highly narrowed wake region and an increase in formation length, suggesting an increase in base pressure. The turbulence intensities in the wake were greatly reduced, and the dominant vortex shedding frequency was com-

pletely removed from the frequency spectrum of streamwise velocity fluctuation for at least 6 BTE thicknesses downstream. The high-speed PIV data revealed that the mechanism of suppression was the generation of small spanwise vortices at the tips of the piezoelectric flaps. The vortices acted to disrupt the communication between the separating shear layers, which lead to the complete suppression of vortex shedding. Fujisawa et al. (2004) and Nati et al. (2013) also reported vortex shedding suppression via shear-layer disruption, and Wiltse and Glezer (1993) reported similar vortex formation when using piezoelectric flaps to manipulate an air jet. Single actuation at $f_a = 3.5f_u$ resulted in a large attenuation of the vortex shedding pattern but not its complete removal. Despite this, the results provide evidence that single actuation may result in complete suppression if actuation amplitudes or frequencies higher than what were investigated here were applied. This suggests that the disruption of a single shear layer may be sufficient for suppressing wake unsteadiness, provided that the disruption is large enough.

Symmetric actuation at $f_a = 1.5f_u$ acted to force both separating shear layers to roll into the wake simultaneously. The resulting symmetric vortices grew as they convected downstream before becoming unstable and decomposing into smaller concentrations of vorticity. The wake unsteadiness continued downstream, and the dominant wake frequency shifted to a value of $0.75f_u$. Similar cases of forced wake symmetry have been reported by Nishihara et al. (2005), Konstantinidis and Balabani (2007), and Pastoor et al. (2008) using different forms of actuation. The latter reported an increase in base pressure by 40%; however, the formation length was not significantly affected when near-wake symmetry was forced here. If a base pressure increase follows the present case of forced symmetry, it is likely not related to an increase in formation length.

Finally, an adaptive slope-seeking controller was designed to optimize the actuation parameter in real time. The controller acted to manipulate the frequency of symmetric actuation using the pressure fluctuation measurements at the surface of the BTE. Extensions to the standard extremum-seeking feedback loop that were proposed by Brackston et al. (2016) were implemented here, resulting in a controller that was able to reach and maintain

an optimal control input within the designed operating range. The controller was also capable of adapting to changes in freestream velocity.

The difficulties associated with active flow control are evident in the present work. Although the actuation methods designed here were highly effective at amplifying and suppressing vortex shedding, they are limited to a narrow range of Re. This is primarily due to the resonant frequency of the piezoelectric flaps, which limited the vortex shedding frequencies that could be effectively manipulated. Techniques such as amplitude-modulated excitation (Wiltse and Glezer, 1993) allow for working around these limitations, but piezoelectric actuators with higher resonant frequencies and larger displacements are what will ultimately lead to extending these methods to higher Re. Measurement devices can also pose issues as is demonstrated here. The observability of the wake during closed-loop control was hindered by the inability of the sensors to measure the downstream wake state. This meant that true optimal vortex shedding suppression was not possible during adaptive slope-seeking. Practical applications demand simple and minimally-invasive flow measurements such as the surface-pressure measurements conducted here, but these are far from ideal for monitoring the entire flow domain that is being controlled.

6.3 Future Work

There are various directions to take when considering extensions to the present work. Some recommendations are given below.

Secondary instabilities as a function of aspect ratio

The present work contradicts simulations (Ryan et al., 2005) and experiments (Naghib-Lahouti et al., 2012, 2014) regarding which secondary modes exist in the wakes of elongated bodies with BTEs and varying AR. Only a single AR was investigated here, and so an experimental parametric study of the secondary instabilities in the wake is needed. Direct, time-resolved measurements of the secondary vortices for a wide range of AR and Re is suggested.

Universality of mode B

Chapter 4 showed that mode B was the dominant secondary instability in the wake of the BTE studied here. This is also true for circular and square cylinders (Williamson, 1996b; Robichaux et al., 1999). This suggests that mode B may be a universal mode that exists in the wake of many symmetric geometries. An experimental examination of the presence of mode B in the wakes of various two-dimensional trailing edge geometries would assist in confirming or denying this assertion.

Secondary instabilities for vortex shedding suppression

The active control strategy studied in this thesis relied on acting upon the primary instability in the wake, and the results demonstrated that shear layer disruption is one possible route to vortex shedding suppression. Amplification of the secondary instability in the near-wake may be an efficient means of achieving this. Some work on this topic has already begun using synthetic jets and plasma actuators (Naghib-Lahouti et al., 2012, 2015; Bhattacharya and Gregory, 2018), but this has not yet been explored using piezoelectric materials.

Instantaneous force measurements during control

The measurements conducted within this thesis limited the analyses to velocity fields and pressure fluctuation data. This allowed for confirming active amplification and suppression of vortex shedding, but the overall effect of actuation was not determined. It is recommended that the active control strategies designed here are investigated using instantaneous base-pressure and load cell measurements so that the drag and lift forces acting on the body can be determined.

Three-dimensional actuation using piezoelectric flaps

The piezoelectric flaps utilized for control in Chapter 5 actuated the wake in a two-dimensional manner. An extension of this to three-dimensional actuation may allow for a more efficient means of suppressing the wake. It is recommended that the flaps be segmented so that actu-

ation can be varied along the span of the body. The actuators can then be used implement various patterns, for example a travelling wave (Bai et al., 2014).

Extension of closed-loop control algorithms

It is recommended that active control strategies beyond adaptive slope-seeking be implemented using the current piezoelectric actuator configuration. Other possible choices includes opposition control (Pastoor et al., 2008), genetic programming (Li et al., 2017), and the use of system identification (Pfeiffer and King, 2018).

6.4 Closing Remarks

Although vortex shedding has been the subject of study for more than a century, its complete understanding still eludes researchers. This thesis has investigated how it affects the wake of a BTE, and how it can be actively controlled using piezoelectric materials. It is hoped that these contributions lead to further advancements in the area of bluff body aerodynamics in the future.

Bibliography

M. Amir and K. Kontis. Application of piezoelectric actuators at subsonic speeds. *J. Aircraft*, 45(4):1419–1430, 2008.

K. B. Ariyur and M. Krstić. *Real-Time Optimization by Extremum-Seeking Control*. Wiley, New York, 2003.

G. Artana, R. Sosa, E. Moreau, and G. Touchard. Control of the near-wake flow around a circular cylinder with electrohydrodynamic actuators. *Exp. Fluids*, 35:580–588, 2003.

M. A. Badri Narayanan and V. Ramjee. On the criteria for reverse transition in a two-dimensional boundary layer flow. *J. Fluid Mech.*, 35(2):225–241, 1969.

H. L. Bai, Y. Zhou, W. G. Zhang, S. J. Xu, Y. Wang, and R. A. Antonia. Active control of a turbulent boundary layer based on local surface perturbation. *J. Fluid Mech.*, 750: 316–354, 2014.

C. Barbi, D. P. Favier, C. A. Maresca, and D. P. Telionis. Vortex shedding lock-on of a circular cylinder in oscillatory flow. *J. Fluid Mech.*, 170:527–544, 1986.

B. Bays-Muchmore and A. Ahmed. On streamwise vortices in turbulent wakes of cylinders. *Phys. Fluids A*, 5(2):387–392, 1993.

J. F. Beaudoin, O. Cadot, J. L. Aider, and J. E. Wesfreid. Bluff-body drag reduction by extremum-seeking control. *J. Fluids Struct.*, 22:973–978, 2006a.

J. F. Beaudoin, O. Cadot, J. L. Aider, and J. E. Wesfreid. Drag reduction of a bluff body using adaptive control methods. *Phys. Fluids*, 18:085107, 2006b.

R. Becker, R. King, R. Petz, and W. Nitsche. Adaptive closed-loop separation control on a high-lift configuration using extremum seeking. *AIAA J.*, 45(6):1382–1392, 2007.

H. Bénard. Formation de centres de giration l'arrire d'un obstacle en mouvement. In *Comptes Rendus de l'Acadmie des Sciences*, volume 147, pages 839–842, 970–972, 1908.

N. Benard and E. Moreau. Response of a circular cylinder wake to a symmetric actuation by non-thermal plasma discharges. *Exp. Fluids*, 54:1467, 2013.

N. Benard, E. Moreau, J. Griffin, and L. N. Cattafesta III. Slope seeking for autonomous lift improvement by plasma surface discharge. *Exp. Fluids*, 48:791–808, 2010.

E. Berger. Suppression of vortex shedding and turbulence behind oscillating cylinders. *Phys. Fluids*, 10:S191–S193, 1967.

G. Berkooz, P. Holmes, and L. Lumley. The proper orthogonal decomposition in the analysis of turbulent flows. *Annu. Rev. Fluid Mech.*, 25:539–575, 1993.

S. Bhattacharya and J. W. Gregory. Effect of three-dimensional plasma actuation on the wake of a circular cylinder. *AIAA J.*, 53(4):958–967, 2015.

S. Bhattacharya and J. W. Gregory. Optimum-wavelength forcing of a bluff body wake. *Phys. Fluids*, 30:015101, 2018.

O. Bilgen, C. de Marqui Junior, K. B. Kochersberger, and D. J. Inman. Piezoceramic composite actuators for flow control in low Reynolds number airflow. *J. Intell. Material Syst. Struct.*, 21:1201–1212, 2010.

M. bin Mansoor, N. Reuther, S. Köble, M. Gérard, H. Steger, P. Woias, and F. Goldschmidtböing. Parametric modeling and experimental characterization of a nonlinear resonant piezoelectric actuator designed for turbulence manipulation. *Sens. Actuators A: Phys.*, 258:14–21, 2017.

H. M. Blackburn and J. M. Lopez. On three-dimensional quasiperiodic Floquet instabilities of two-dimensional bluff body wakes. *Phys. Fluids*, 15(8):L57, 2003.

H. M. Blackburn, F. Marques, and J. M. Lopez. Symmetry breaking of two-dimensional time-periodic wakes. *J. Fluid Mech.*, 522:395–411, 2005.

R. F. Blackwelder and H. Eckelmann. Streamwise vortices associated with the bursting phenomenon. *J. Fluid Mech.*, 94(3):577–594, 1979.

R. F. Blackwelder and L. S. G. Kovasznay. Large-scale motion of a turbulent boundary layer during relaminarization. *J. Fluid Mech.*, 53(1):61–83, 1972.

M. S. Bloor. The transition to turbulence in the wake of a circular cylinder. *J. Fluid Mech.*, 19(2):290–304, 1964.

R. D. Brackston, A. Wynn, and J. F. Morrison. Extremum seeking to control the amplitude and frequency of a pulsed jet for bluff body drag reduction. *Exp. Fluids*, 57:159, 2016.

M. Brede, H. Eckelmann, and D. Rockwell. On secondary vortices in the cylinder wake. *Phys. Fluids*, 8(8):2117–2124, 1996.

T. F. Brooks, D. S. Pope, and M. A. Marcolini. Airfoil self-noise and prediction. *NASA Ref. Publ. 1218*, 1989.

S. L. Brunton and B. R. Noack. Closed-loop turbulence control: progress and challenges. *Appl. Mech. Rev.*, 67:050801, 2015.

L. N. Cattafesta III and M. Sheplak. Actuators for active flow control. *Annu. Rev. Fluid Mech.*, 43:247–272, 2011.

L. N. Cattafesta III, S. Garg, and D. Shukla. Development of piezoelectric actuators for active flow control. *AIAA J.*, 39(8):1562–1568, 2001.

L. N. Cattafesta III, Q. Song, D. R. Williams, C. W. Rowley, and F. S. Alvi. Active control of flow-induced cavity oscillations. *Prog. Aerosp. Sci.*, 44:479–502, 2008.

T. Chabert, J. Dandois, and E. Garnier. Experimental closed-loop control of flow separation over a plain flap using slope seeking. *Exp. Fluids*, 55:1797, 2014.

T. Chabert, J. Dandois, and E. Garnier. Experimental closed-loop control of separated-flow over a plain flap using extremum seeking. *Exp. Fluids*, 57:37, 2016.

C. T. Chen. *Linear System Theory and Design.* Oxford University Press, Oxford, New York, 1999.

H. Choi, W. P. Jeon, and J. Kim. Control of flow over a bluff body. *Annu. Rev. Fluid Mech.*, 40:113–139, 2008.

E. Detemple-Laake and H. Eckelmann. Phenomenology of Kármán vortex streets in oscillatory flow. *Exp. Fluids*, 7:217–227, 1989.

L. H. Feng and J. J. Wang. Circular cylinder vortex-synchronization control with a synthetic jet positioned at the rear stagnation point. *J. Fluid Mech.*, 662:232–259, 2010.

J. E. Ffowcs Williams and B. C. Zhao. The active control of vortex shedding. *J. Fluids Struct.*, 3(2):115–122, 1989.

N. Fujisawa and T. Nakabayashi. Neural network control of vortex shedding from a circular cylinder using rotational feedback oscillations. *J. Fluids Struct.*, 16(1):113–119, 2002.

N. Fujisawa, G. Takeda, and N. Ike. Phase-averaged characteristics of flow around a circular cylinder under acoustic excitation control. *J. Fluid Struct.*, 19:159–170, 2004.

J. H. Gerrard. The mechanics of the formation region of vortices behind bluff bodies. *J. Fluid Mech.*, 25(2):401–413, 1966.

J. H. Gerrard. The wakes of cylindrical bluff bodies at low Reynolds number. *Phil. Trans. R. Soc. A*, 288(1354):351–382, 1978.

S. Ghaemi, D. Ragni, and F. Scarano. PIV-based pressure fluctuations in the turbulent boundary layer. *Exp. Fluids*, 53(6):1823–1840, 2012.

L. Graftieaux, M. Michard, and N. Grosjean. Combining PIV, POD and vortex identification algorithms for the study of unsteady turbulent swirling flows. *Meas. Sci. Technol.*, 12: 1422–1429, 2001.

X. Y. Huang. Feedback control of vortex shedding from a circular cylinder. *Exp. Fluids*, 20 (3):218–224, 1996.

C. P. Jackson. A finite-element study of the onset of vortex shedding in flow past variously shaped bodies. *J. Fluid Mech.*, 182:23–45, 1987.

S. A. Jacobson and W. C. Reynolds. Active control of streamwise vortices and streaks in boundary layers. *J. Fluid Mech.*, 360:179–211, 1998.

W. P. Jeon and R. F. Blackwelder. Perturbations in the wall region using flush mounted piezoceramic actuators. *Exp. Fluids*, 28:485–496, 2000.

J. Jeong and F. Hussain. On the identification of a vortex. *J. Fluid Mech.*, 285:69–94, 1995.

M. R. Johnson and L. W. Kostiuk. Efficiencies of low-momentum jet diffusion flames in crosswinds. *Combust. Flame*, 123(1):189–200, 2000.

T. A. Johnson and V. C. Patel. Flow past a sphere up to a Reynolds number of 300. *J. Fluid Mech.*, 378:19–70, 1999.

T. N. Jukes and K. S. Choi. Control of unsteady flow separation over a circular cylinder using dielectric-barrier-discharge surface plasma. *Phys. Fluids*, 21:094106, 2009.

R. D. Keane and R. J. Adrian. Theory of cross-correlation analysis of PIV images. *Appl. Sci. Res.*, 49:191–215, 1992.

M. F. Kerho and M. B. Bragg. Neutrally buoyant bubbles used as flow tracers in air. *Exp. Fluids*, 16:393–400, 1994.

D. H. Kim, J. W. Chang, and J. S. Cho. Flow disturbances depending on excitation frequency on a flat plate by a piezoceramic actuator. *J. Vis.*, 16:111–121, 2013.

K. Kim, C. Kasnakogğlu, A. Serrani, and M. Samimy. Extremum-seeking control of subsonic cavity flow. *AIAA J.*, 47(1):195–205, 2009.

E. Konstantinidis and S. Balabani. Symmetric vortex shedding in the near wake of a circular cylinder due to streamwise perturbations. *J. Fluids Struct.*, 23:1047–1063, 2007.

I. Korkischko and J. R. Meneghini. Suppression of vortex-induced vibration using moving surface boundary-layer control. *J. Fluids Struct.*, 34:259–270, 2012.

A. V. Kozlov and F. O. Thomas. Bluff-body flow control via two types of dielectric barrier discharge plasma actuation. *AIAA J.*, 49(9):1919–1931, 2011.

R. Li, B. R. Noack, L. Cordier, J. Bore, and F. Harambat. Drag reduction of a car model by linear genetic programming control. *Exp. Fluids*, 58:103, 2017.

J. Lin, J. P. Laval, J. M. Foucaut, and M. Stanislas. Quantitative characterization of coherent structures in the buffer layer of near-wall turbulence. Part 1: streaks. *Exp. Fluids*, 45(6):999–1013, 2008.

J. C. Lin, J. Towfighi, and D. Rockwell. Instantaneous structure of the near-wake of a circular cylinder: On the effect of Reynolds number. *J. Fluids Struct.*, 9(4):409–418, 1995a.

J. C. Lin, J. Towfighi, and D. Rockwell. Near-wake of a circular cylinder: control by steady and unsteady surface injection. *J. Fluid Struct.*, 9:659–669, 1995b.

S. C. Luo, X. H. Tong, and B. C. Khoo. Transition phenomena in the wake of a square cylinder. *J. Fluids Struct.*, 23(2):227–248, 2007.

A. Mallock. On the resistance of air. In *Proceedings of the Royal Society of London*, volume 79 of *Series A*, pages 262–273, 1907.

H. Mansy, P. M. Yang, and D. R. Williams. Quantitative measurements of three-dimensional structures in the wake of a circular cylinder. *J. Fluid Mech.*, 270:277–296, 1994.

J. Mathew, Q. Song, B. V. Sankar, M. Sheplak, and L. N. Cattafesta III. Optimized design of piezoelectric flap actuators for active flow control. *AIAA J.*, 44(12):2919–2928, 2006.

C. D. Meinhart, S. T. Wereley, and J. G. Santiago. A PIV algorithm for estimating time-averaged velocity fields. *J. Fluids Eng.*, 122(2):285–289, 2000.

A. Melling. Tracer particles and seeding for particle image velocimetry. *Meas. Sci. Technol.*, 8:1406–1416, 1997.

A. Naghib-Lahouti, L. S. Doddipatla, and H. Hangan. Secondary wake instabilities of a blunt trailing edge profiled body as a basis for flow control. *Exp. Fluids*, 52(6):1547–1566, 2012.

A. Naghib-Lahouti, P. Lavoie, and H. Hangan. Wake instabilities of a blunt trailing edge profiled body at intermediate Reynolds numbers. *Exp. Fluids*, 55(7):1779, 2014.

A. Naghib-Lahouti, H. Hangan, and P. Lavoie. Distributed forcing flow control in the wake of a blunt trailing edge profiled body using plasma actuators. *Phys. Fluids*, 27:035110, 2015.

G. Nati, M. Kotsonis, S. Ghaemi, and F. Scarano. Control of vortex shedding from a blunt trailing edge using plasma actuators. *Exp. Therm. Fluid Sci.*, 46:199–210, 2013.

T. Nishihara, S. Kaneko, and T. Watanabe. Characteristics of fluid dynamic forces acting on a circular cylinder oscillated in the streamwise direction and its wake patterns. *J. Fluids Struct.*, 20:505–518, 2005.

A. Ongoren and D. Rockwell. Flow structure from an oscillating cylinder Part 2. Mode competition in the near wake. *J. Fluid Mech.*, 191:225–245, 1988.

M. Pastoor, L. Henning, B. R. Noack, R. King, and G. Tadmor. Feedback shear layer control for bluff body drag reduction. *J. Fluid Mech.*, 608:161–196, 2008.

V. C. Patel and M. R. Head. Reversion of turbulent to laminar flow. *J. Fluid Mech.*, 34(2): 371–392, 1968.

M. S. Petrusma and S. L. Gai. Bluff body wakes with free, fixed, and discontinuous separation at low Reynolds numbers and low aspect ratio. *Exp. Fluids*, 20(3):189–198, 1996.

J. Pfeiffer and R. King. Robust control of drag and lateral dynamic response for road vehicles exposed to cross-wind gusts. *Exp. Fluids*, 59:45, 2018.

A. K. Prasad and K. Jensen. Scheimpflug stereocamera for particle image velocimetry in liquid flows. *Appl. Optics*, 34:7092–7099, 1995.

Y. Qu, J. Wang, M. Sun, L. Feng, C. Pan, Q. Gao, and G. He. Wake vortex evolution of a square cylinder with a slot synthetic jet positioned at the rear surface. *J. Fluid Mech.*, 812:940–965, 2017.

M. Raffel, C. E. Willert, S. T. Wereley, and J. Kompenhans. *Particle Image Velocimetry: A Practical Guide*. Springer, Berlin, Germany, 2007.

D. Ragni, F. Schrijer, B. W. van Oudheusden, and F. Scarano. Particle tracer response across shocks measured by PIV. *Exp. Fluids*, 50:53–64, 2011.

J. Robichaux, S. Balachandar, and S. P. Vanka. Three-dimensional Floquet instability of the wake of square cylinder. *Phys. Fluids*, 11(3):560–578, 1999.

A. Roshko. On the development of turbulent wakes from vortex streets. *NACA rep. 1191*, 1954.

A. Roshko. Perspectives on bluff body aerodynamics. *J. Wind Eng. Ind. Aerodyn.*, 49(1): 79–100, 1993.

K. Roussopoulos. Feedback control of vortex shedding at low Reynolds numbers. *J. Fluid Mech.*, 248:267–296, 1993.

K. Ryan, M. C. Thompson, and K. Hourigan. Three-dimensional transition in the wake of bluff elongated cylinders. *J. Fluid Mech.*, 538:1–29, 2005.

F. Scarano and M. L. Riethmuller. Advances in iterative multigrid PIV image processing. *Exp. Fluids*, 29(1):S051–S060, 2000.

F. Scarano, S. Ghaemi, G. C. A. Caridi, J. Bosbach, U. Dierksheide, and A. Sciacchitano. On the use of helium-filled soap bubbles for large-scale tomographic piv in wind tunnel experiments. *Exp. Fluids*, 56:42, 2015.

W. Schoppa and F. Hussain. Coherent structure generation in near-wall turbulence. *J. Fluid Mech.*, 453:57–108, 2002.

J. C. Schulmeister, J. M. Dahl, G. D. Weymouth, and M. S. Triantafyllou. Flow control with rotating cylinders. *J. Fluid Mech.*, 825:743–763, 2017.

G. J. Sheard, M. J. Fitzgerald, and K. Ryan. Cylinders with square cross-section: wake instabilities with incidence angle variation. *J. Fluid Mech.*, 630:43–69, 2009.

S. J. Sheather. Density estimation. *Stat. Sci.*, 19(4):588–597, 2004.

X. D. Shi and L. H. Feng. Control of flow around a circular cylinder by bleed near the separation points. *Exp. Fluids*, 56:214, 2015.

L. Sirovich. Turbulence and the dynamics of coherent structures, parts I-III. *Q. Appl. Math.*, 45:561–590, 1987.

C. R. Smith and S. P. Metzler. The characteristics of low-speed streaks in the near-wall region of a turbulent boundary layer. *J. Fluid Mech.*, 129:27–54, 1983.

V. Strouhal. Über eine besondere Art der Tonerregung. *Annalen der Physik*, 5:216–251, 1878.

P. R. Tadikamalla. A look at the Burr and related distributions. *Int. Stat. Rev.*, 48(3): 337–344, 1980.

J. S. Tao, X. Y. Huang, and W. K. Chan. A flow visualization study on feedback control of vortex shedding from a circular cylinder. *J. Fluids Struct.*, 10(8):965–970, 1996.

M. C. Thompson, T. Leweke, and C. H. K. Williamson. The physical mechanism of transition in bluff body wakes. *J. Fluids Struct.*, 15(3):607–616, 2001.

C. D. Tomkins and R. J. Adrian. Spanwise structure and scale growth in turbulent boundary layers. *J. Fluid Mech.*, 490:37–74, 2003.

C. Tropea, A. L. Yarin, and J. Foss. *Handbook of Experimental Fluid Mechanics*. Springer, Berlin, Germany, 2007.

B. W. van Oudheusden, F. Scarano, N. P. van Hinsberg, and D. W. Watt. Phase-resolved characterization of vortex shedding in the near wake of a square-section cylinder at incidence. *Exp. Fluids*, 39:86–98, 2005.

T. von Kármán. Über den Mechanismus des Widerstandes, den ein bewegter Körper in einer Flüssigkeit erfährt. *Nachrichten von der Gesellschaft der Wissenschaften zu Göttingen, Mathematisch-Physikalische Klasse*, pages 509–517, 1911.

T. von Kármán. *Aerodynamics: Selected Topics in the Light of Their Historical Development*. McGraw-Hill, 1954.

H. M. Warui and N. Fujisawa. Feedback control of vortex shedding from a circular cylinder by cross-flow cylinder oscillations. *Exp. Fluids*, 21(1):49–56, 1996.

T. Wei and C. R. Smith. Secondary vortices in the wake of circular cylinders. *J. Fluid Mech.*, 169:513–533, 1986.

J. Westerweel and F. Scarano. Universal outlier detection for PIV data. *Exp. Fluids*, 39(6): 1096–110, 2005.

B. Wieneke. Stereo-PIV using self-calibration on particle images. *Exp. Fluids*, 39(2):267–280, 2005.

D. R. Williams, H. Mansy, and C. Amato. The response and symmetry properties of a cylinder wake subjected to localized surface excitation. *J. Fluid Mech.*, 234:71–96, 1992.

C. H. K. Williamson. The existence of two stages in the transition to three-dimensionality of a cylinder wake. *Phys. Fluids*, 31(11):3165–3168, 1988a.

C. H. K. Williamson. Defining a universal and continuous Strouhal-Reynolds number relationship for the laminar vortex shedding of a circular cylinder. *Phys. Fluids*, 31:2742, 1988b.

C. H. K. Williamson. Vortex dynamics in the cylinder wake. *Annu. Rev. Fluid Mech.*, 28: 477–539, 1996a.

C. H. K. Williamson. Three-dimensional wake transition. *J. Fluid Mech.*, 328:345–407, 1996b.

C. H. K. Williamson and R. Govardhan. Vortex-induced vibrations. *Annu. Rev. Fluid Mech.*, 36:413–455, 2004.

J. M. Wiltse and A. Glezer. Manipulation of free shear flows using piezoelectric actuators. *J. Fluid Mech.*, 249:261–285, 1993.

J. M. Wiltse and A. Glezer. Direct excitation of small-scale motions in free shear flows. *Phys. Fluids*, 10:2026, 1998.

A. Wu, Y. Zhou, H. L. Cao, and W. J. Li. Closed-loop enhancement of jet mixing with extremum-seeking and physics-based strategies. *Exp. Fluids*, 57:107, 2016.

J. Wu, J. Sheridan, J. Soria, and M. C. Welsh. An experimental investigation of streamwise vortices in the wake of a bluff body. *J. Fluids Struct.*, 8(6):621–624, 1994.

J. Wu, J. Sheridan, M. C. Welsh, and K. Hourigan. Three-dimensional vortex structures in a cylinder wake. *J. Fluid Mech.*, 312:201–222, 1996.

S. J. Xu, Y. Zhou, and M. H. Wang. A symmetric binary-vortex street behind a longitudinally oscillating cylinder. *J. Fluid Mech.*, 556:27–43, 2006.

I. Yildirim, C. C. M. Rindt, and A. A. van Steenhoven. Mode C flow transition behind a circular cylinder with a near-wake wire disturbance. *J. Fluid Mech.*, 727:30–55, 2013.

M. M. Zdravkovich. Different modes of vortex shedding: an overview. *J. Fluids Struct.*, 10: 427–437, 1996.

H. Q. Zhang, U. Fey, B. R. Noack, M. König, and H. Eckelmann. On the transition of the cylinder wake. *Phys. Fluids*, 7(4):779–794, 1995.

M. M. Zhang, L. Cheng, and Y. Zhou. Closed-loop-controlled vortex shedding and vibration of a flexibly supported square cylinder under different schemes. *Phys. Fluids*, 16(5):1439, 2004.

M. M. Zhang, Y. Zhou, and L. Cheng. Closed-loop-manipulated wake of a stationary square cylinder. *Exp. Fluids*, 39(1):75–85, 2005.

Appendices

A Flow Acceleration Upstream from the Blunt Trailing Edge

The mean boundary layer profiles shown in Figure 4.1 display evidence of a favourable pressure gradient (FPG) as is discussed in Section 4.1, which causes the flow to accelerate. This flow acceleration just upstream from the blunt trailing edge (BTE) has been confirmed using a separate planar particle image velocimetry (PIV) experiment.

The PIV experiment utilized a single Imager ProX-4M camera featuring a 2048×2048-pixel CCD sensor with a 7.4×7.4 μm^2 pixel size and 14-bit resolution. The camera was used to image the wake region and a portion of the upstream boundary layer, resulting in a resolution of 36.4 μm/pix. Illumination for the experiment was provided by a Spectra-Physics PIV-400-10 Nd:YAG laser capable of producing 532 nm light at 400 mJ per pulse with a pulse width of 5-8 ns. Sets of 2000 images were collected for each of the 5 Reynolds numbers (Re) considered and an ensemble-of-correlation (Meinhart et al., 2000) was applied to the boundary layer region $0.5h$ upstream from the BTE.

The results of the planar PIV experiment are presented in Figure A.1, where the axes have been normalized using the value and location of the maximum velocity in each profile. Each of the profiles in the plot features a bulge where the velocity exceeds that of the freestream value. This bulge is not present in zero-pressure-gradient (ZPG) boundary layer profiles, and has been caused by the flow accelerating into the near-wake region. This acceleration is indicative of the FPG within these boundary layers, and explains the behaviour of the semi-logarithmic profiles within Figure 4.1*b*.

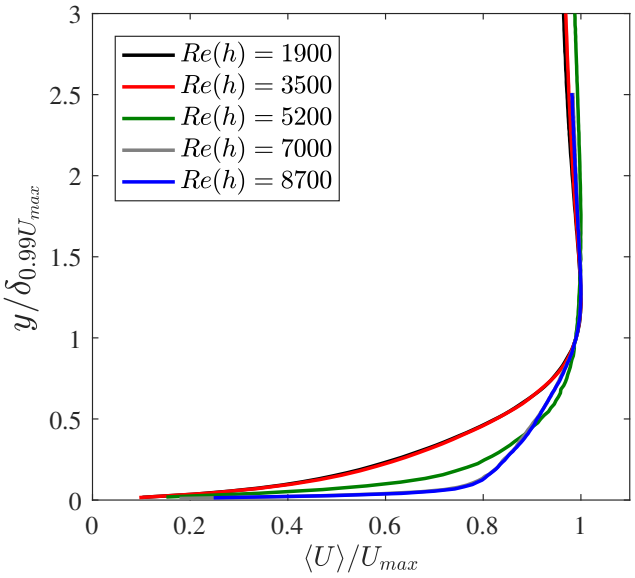

Figure A.1: Mean boundary layer profiles $0.5h$ upstream from the BTE. Note that only one of the laminar and one of the turbulent profiles are fully visible due to complete overlap of the curves. The bulge in the profiles caused by the favourable pressure gradient is located at the intersection of unity on both axes.